GEOCHEMICAL INVESTIGATION OF FLUID PETROLEUM COKE DEPOSITS AT AN OIL SANDS MINE IN NORTHERN ALBERTA, CANADA

A Thesis Submitted to the College of

Graduate Studies and Research

In Partial Fulfillment of the Requirements

For the Degree of Master of Science

In the Department of Geological Sciences

University of Saskatchewan

Saskatoon

By

JAKE ADAM NESBITT

PERMISSION TO USE

In presenting this thesis in partial fulfillment of the requirements for a Postgraduate degree from the University of Saskatchewan, I agree that the Libraries of this University may make it freely available for inspection. I further agree that permission for copying of this thesis in any manner, in whole or in part, for scholarly purposes may be granted by the professor or professors who supervised my thesis work or, in their absence, by the Head of the Department or the Dean of the College in which my thesis work was done. It is understood that any copying or publication or use of this thesis or parts thereof for financial gain shall not be allowed without my written permission. It is also understood that due recognition shall be given to me and to the University of Saskatchewan in any scholarly use which may be made of any material in my thesis.

Requests for permission to copy or to make other uses of materials in this thesis/dissertation in whole or part should be addressed to:

Head of the Department of Geological Sciences
114 Science Place
University of Saskatchewan
Saskatoon, Saskatchewan S7N 5E2 Canada

ABSTRACT

The geochemical characteristics of three petroleum coke deposits at an oil sands mine near Fort McMurray, Alberta were investigated. This coke was generated in large volumes via fluidized-bed coking during the upgrading of oil sands bitumen and slurried with process-affected water to deposits onsite. This research examined variations in trace element speciation and release under varied field conditions. Continuous core sampling and multi-level well groundwater sampling were performed to 8 m depth throughout the deposits to acquire samples from differing storage and redox conditions. Bulk elemental analyses confirmed that this coke was composed mainly of C and S, with a secondary fraction of clays and oxides (Si, Al, Fe, Ti, Ca, K, Mg) and a suite of trace metals dominated by V (1280 ± 120 mg kg^{-1}) and Ni (230 ± 80 mg kg^{-1}). Synchrotron powder X-ray diffraction revealed the presence of Si and Ti oxides, organically-complexed V, hydrated Ni sulfate, and provided information about the aromatic carbon matrix. Electron microprobe analyses, scanning electron microscopy, and X-ray fluorescence mapping revealed concentric rings within coke grains, with elevated concentration of inorganics, V, and Ni in the ring margins. Vanadium and Ni K-edge X-ray absorption spectroscopy (XAS) showed that these elements were hosted in porphyrins and similar organic complexes throughout coke grains. Micro-focused XAS showed that V and Ni speciation is different in the concentric ring margins. Vanadium coordination is consistent with substitution into the distorted octahedral site of phyllosilicates, and Ni is either hosted in distorted asphaltenic metal sites or in Ni oxide. Sulfur and Fe XANES confirmed that thiophenic coordination and pyritic-ilmenitic coordination are predominant, respectively. Groundwater depth profiles of pH, Eh, electrical conductivity, major ions, and stable isotopes of water showed evidence of a mixing zone between infiltrating, oxic, sub-neutral pH precipitation and underlying, anoxic, alkaline pH process water. Vanadium and Ni are mobilized only at the top of the saturated zone due to ingress of oxygen and precipitation. Vanadium was found to undergo oxidative mobilization in the form of oxyanionic species whereas Ni mobilization occurred as pH decreased.

ACKNOWLEDGEMENTS

I would first like to acknowledge the unwavering support and mentorship of my supervisor Dr. Matt Lindsay throughout the entire degree and for the welcoming environment he fostered for our research group. Thank you also to my advisory committee member, Dr. Jim Hendry, for advice and guidance and to Dr. Derek Peak, for reviewing my thesis. A number of colleagues and staff from the University of Saskatchewan also provided invaluable assistance with many aspects of my project. Kathryn Dompierre helped with field work over the course of several rainy September days. Jonathan Vyskocil performed all microbiological lab work in collaboration with this project. Kaitlyn Heaton assisted with the fabrication of water sampling wells. Dr. Joyce McBeth and Samira Sumaila helped me with X-ray diffraction data collection and processing. From Syncrude Canada Ltd., Dallas Heisler, Lori Cyprien, and Chris Beierling all provided administrative assistance and help on site. I would also like to thank Dallas McGowan and the ConeTec staff for going above and beyond to help ensure sample collection went smoothly.

Funding for this research was provided by Syncrude Canada Ltd. and the National Sciences and Engineering Research Council of Canada (NSERC) through the NSERC/Syncrude Industrial Research Chair in Mine Closure Geochemistry (Grant No. IRCPJ-463568-13) held by Dr. Matt Lindsay. Additional support from the SRK Consulting (Canada) Graduate Scholarship Program is also acknowledged. A portion of the research described in this thesis was performed at the Canadian Light Source, which is funded by the Canada Foundation for Innovation, the NSERC, the National Research Council Canada, the Canadian Institutes of Health Research, the Government of Saskatchewan, Western Economic Diversification Canada, and the University of Saskatchewan. This research also used resources of the Advanced Photon Source, a U.S. Department of Energy (DOE) Office of Science User Facility operated for the DOE Office of Science by Argonne National Laboratory under Contract No. DE-AC02-06CH11357. The extensive synchrotron work I performed would have been virtually impossible without the support and guidance provided by beamline staff. My first and biggest mention goes to Ning Chen (CLS HXMA) for all his kind assistance, for teaching me how to play the game of synchrotron science,

and for performing extensive XAS modelling in collaboration with this project. Weifeng Chen and Jinru Lin (CLS HXMA), and Yongfeng Hu and Aimee MacLennan (CLS SXRMB) provided many hours of training and assistance. Matt Newville and Tony Lanzirotti (APS 13-ID-E) provided training, advice, and helped with data management.

Finally, and most importantly, thank you to my family and to Ashley for your undying love and for supporting my decision to move so far away to pursue my dreams. Thank you for the endless emotional and academic support, feedback and editing, and for constantly inspiring me to believe in myself.

TABLE OF CONTENTS

LIST OF TABLES

LIST OF FIGURES

LIST OF ABBREVIATIONS

APS	Advanced Photon Source
CLS	Canadian Light Source
CMCF	Canadian Light Source Canadian Macromolecular Crystallography Facility
EDX	energy-dispersive x-ray
EMP	electron microprobe
EPA	Environmental Protection Agency
(μ)EXAFS	(micro) extended x-ray absorption fine structure
FDMNES	finite difference modelling of the near-edge structure
HDPE	high-density polyethylene
HXMA	Canadian Light Source Hard X-ray Micro-analysis
ICP-MS	inductively coupled plasma-mass spectrometry
ICP-OES	inductively coupled plasma-optical emission spectrometry
LCF	linear combination fitting
LDPE	low-density polyethylene
NA	naphthenic acid
NiOEP	nickel octaethyl porphyrin
NiTPP	nickel tetraphenyl porphyrin
OSPW	oil sands process-affected water
pH_{PZC}	pH point of zero charge
REE	rare earth element
SCL	Syncrude Canada Limited
SEM	scanning electron microscope
SXRMB	Canadian Light Source Soft X-ray Microcharacterization Beamline
VOOEP	vanadyl octaethyl porphyrin
VOPBD	vanadyl bis-(1-phenyl-1,3-butanedionato)
VOTPP	vanadyl tetraphenyl porphyrin

VOTTDPz	vanadyl tetrakis(thiadiazole)porphyrazine
(P)XRD	(powder) X-ray diffraction
(μ)XRF	(micro) X-ray fluorescence
(μ)XAS	(micro) X-ray absorption spectroscopy
(μ)XANES	(micro) X-ray absorption near edge spectroscopy
13-ID-E	Advanced Photon Source, Sector 13, Insertion Device E, GeoSoilEnviro Center for Advanced Radiation Sources microprobe beamline

CHAPTER 1 INTRODUCTION & LITERATURE REVIEW

1.1 Introduction

Oil sands mining has both physical and chemical impacts on the environment. Bitumen is recovered from oil sands either by *in situ* steam-assisted gravity drainage or by surface mining. The latter is only feasible to a depth of approximately 80 m (Kasperski and Mikula, 2011). These operations generate mining wastes and upgrading byproducts during the production of synthetic crude oil. Petroleum coke is generated in large quantities during the coking step of the bitumen upgrading process. The Athabasca oil sands region coke inventory was 50 million tonnes (Mt) in 2007, had reached 100 Mt by 2016 (AER, 2015), and is projected to increase to roughly 1000 Mt by the time oil sands mining in the region is complete (Fedorak and Coy, 2006).

Coke is composed primarily of carbon, which occurs as asphaltenic molecular aggregates. Sulfur, Si, metal(loid)s (Fe, Al, Ti, etc.), and a suite of trace elements comprise the balance of the chemical composition (Zubot et al., 2012). Vanadium and Ni are the most abundant potentially-hazardous trace metals in coke. They are derived from metalloporphyrin complexes and poorly-understood non-porphyrinic organo-metallic compounds in the bitumen feedstock. Vanadium and Ni porphyrinic complexes exhibit exceptional thermal stability and are expected to persist during diagenesis (Lewan and Maynard, 1982). These metals become preferentially concentrated into the coke during the coking process (Dechaine and Gray, 2010).

The speciation of trace metals hosted in coke is thought to be strongly influenced by the initial bitumen feed. However, the coking process as well as chemical and physical weathering could change this porphyrin-dominated speciation to less stable forms. Oxidation or degradation of V-bearing phases in the near-surface oxic zone of coke deposits could lead to oxidative V release into the aqueous phase as highly mobile V(V) hydroxyanionic species. Nickel could be released from the solid phase into the aqueous phase as the Ni^{2+} ion. Understanding the geochemical factors leading to these potential chemical transitions is fundamental to understanding metal mobility.

1.2 Research Motivation

Coke exhibits elevated V and Ni concentrations, and leachates containing these elements have been shown to be toxic to aquatic organisms (Puttaswamy et al., 2010; Puttaswamy and Liber,

2011; Puttaswamy and Liber, 2012; Baker et al., 2012). The current research aims to refine the understanding of solid-phase V and Ni speciation in petroleum coke deposits, and to determine whether the aqueous-phase comportment varies under different field redox conditions. Coke is currently stockpiled in large quantities for potential use in oil sands mine post-closure reclamation landforms. Accessible storage of coke is currently mandated by Alberta provincial regulations because it is considered a potential fuel source. In some cases, it is stored subaerially and thus wind-blown coke is also a potential environmental risk (Zhang et al., 2016). A fraction of coke is also used at oil sands mines as fuel for boilers (AER, 2015). The high sulfur and trace metal content of coke has raised environmental concerns regarding both its combustion and long-term storage.

1.3 Project Scope

The current research project is part of an NSERC-Syncrude Industrial Research Chair program aimed at improving the understanding of biogeochemical processes in oil sands mine wastes and their potential impact on water quality in mine closure landscapes. This Master's thesis project is specifically focused on understanding the geochemical controls on metal mobility in petroleum coke deposits. Spatial and temporal variations in geochemical redox processes are hypothesized to be controlling factors in the release and attenuation of metals in the coke pore water system.

Core sampling and pore water sampling campaigns were completed at the Mildred Lake mine, which is operated by Syncrude Canada Limited (Syncrude). A suite of both bulk and micro-focused synchrotron-based spectroscopy, bulk elemental analyses, powder X-ray diffraction, and physical characterization were employed. Coke deposit pore water geochemistry was studied in detail. Measurements included pH, Eh, alkalinity, H_2S, NH_4^+, major cations, inorganic anions, trace elements, acid-extractable organics, and stable isotopes of water.

1.4 Description of Field Site

Petroleum coke generated at Syncrude's Mildred lake upgrading facility was sequentially stockpiled in a series of four coke storage cells from 1979-1985, with a total area of <0.6 km^2. Approximately 31 M m^3 of coke was stockpiled in Coke Cell 5 (CC5) (Figure 1-1b) from 1985-1999, to a depth of roughly 60 m, and thereafter capped with a <1 m thick reclamation soil layer (peat-mineral mix) and vegetated. The lower 45 m of coke in CC5 is saturated and the upper 15 m is projected to remain unsaturated in the final closure landscape. The Mildred Lake Settling Basin (MLSB) received coarse tailings slurries until the maximum allowable elevation of 349.5 m above

sea level was reached in 2000, at which point this large impoundment began to be used for coke storage (Figure 1-1a). Coke has been hydraulically transported with oil sands process-affected water (OSPW) since 2000 via pipeline from the upgrading facilities to the western margin of MLSB and hydraulically deposited forming a beach (Zubot, 2010). The depth of the Coke Beach (CB) deposit is variable but was between 10 and 30 m thick at sampling locations. Only the upper 1 to 3 m of CB are unsaturated. A section in the southwest corner of CB was capped with a reclamation soil layer and vegetated beginning in 2003. A small portion of this Coke Watershed was instrumented with lysimeters to examine coke pore water chemistry and properties of coke (Kessler and Hendry, 2006).

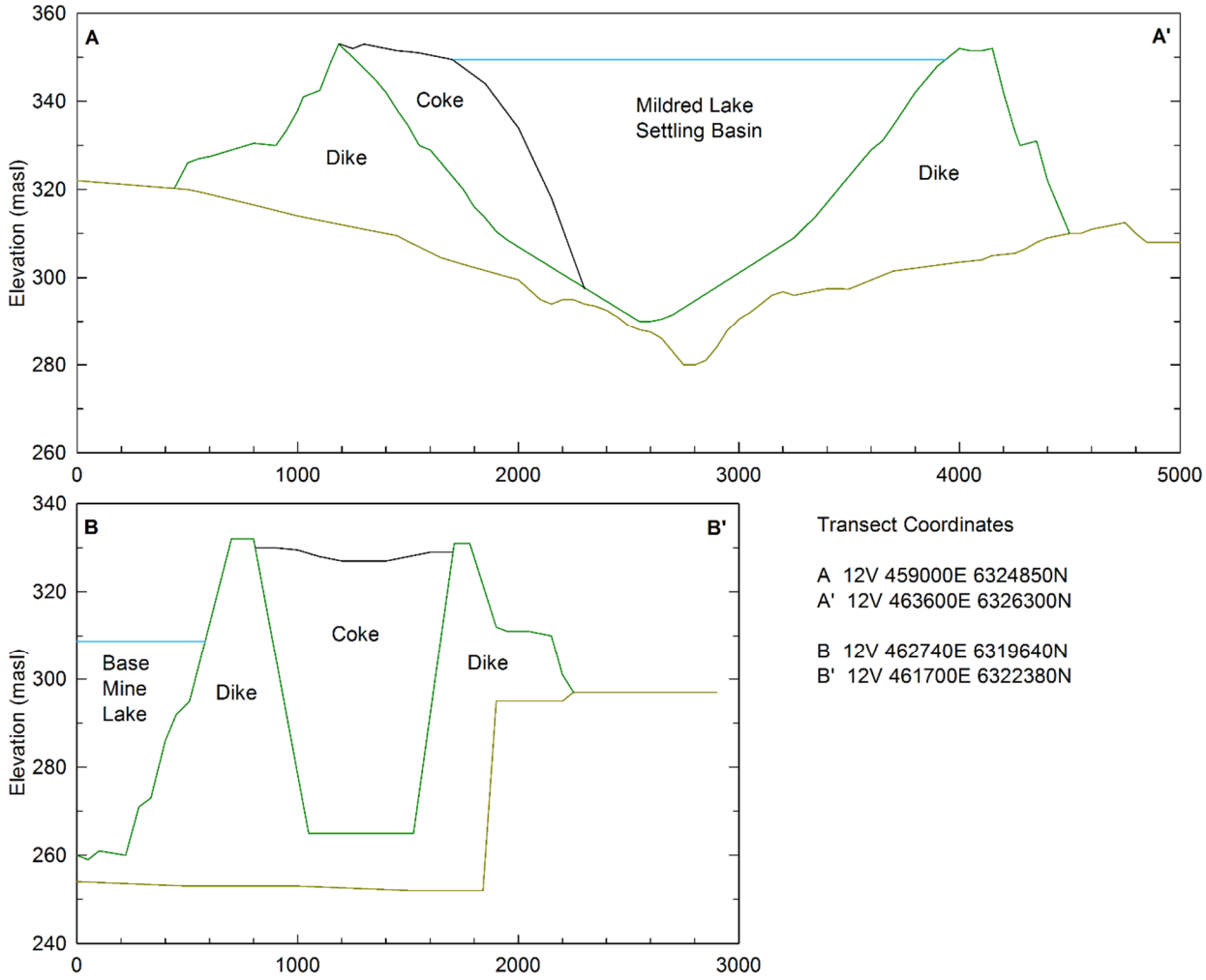

Figure 1-1. Cross-sections of a) Mildred Lake Settling Basin, including Coke Beach, and b) Coke Cell 5. The vertical scale is exaggerated 20 times. The sub-aqueous portion of Coke Beach is drawn schematically.

1.5 Literature Review

The following review outlines past studies of relevance to the current study, and attempts to situate the current research in the context of previous studies. A review of the properties of coke and sources of associated trace elements is followed by a discussion of their geochemical behaviour and methods for examining their comportment in coke deposits.

1.5.1 Petroleum Coke Production and Composition

Oil sands petroleum coke is generated either by fluid coking, flexicoking, or delayed coking. Fluid coke is generated at a rate of approximately 20 kg for every barrel of synthetic crude oil produced (Fedorak and Coy, 2006). Pre-existing coke is heated in a burner unit and then transferred to the coker unit. Steam is injected from below and the bitumen feed is heated to approximately 550 °C and sprayed into the coker where it coats the particles of hot coke (Blaser, 1992). The complex hydrocarbon molecules in bitumen are cracked into shorter molecules on the surface of existing coke particles and lighter hydrocarbon fractions escape from the coker in the vapour phase (Figure 1-2). Once captured, this hot vapour can be further fractionated into petroleum products ranging from gases and naphtha to heavy gas oil. The hot coke coated with high molecular weight organic material gradually cools, exits the coker, and is directed back to the burner unit (Matsen, 1996). Since layers of additional mass accumulate on coke particles during successive coking cycles, surplus coke is extracted from the burner unit and slurried with OSPW for transport and deposition. Flexicoking involves an additional gasification step that reduces the C, S, and volatiles content. Conversely, delayed coking employs a brief thermal cracking step in a fired heater followed by a longer cracking cycle in an insulated coke vessel. Delayed coking is performed at 415-450 °C, versus 480-565 °C for fluid coke, resulting in a higher volatile content in delayed coke (7-13 %) than in fluid coke (4-6 %) (Anthony, 1995). Delayed coke accumulates in the coker and then must be mechanically removed (Anthony, 1995).

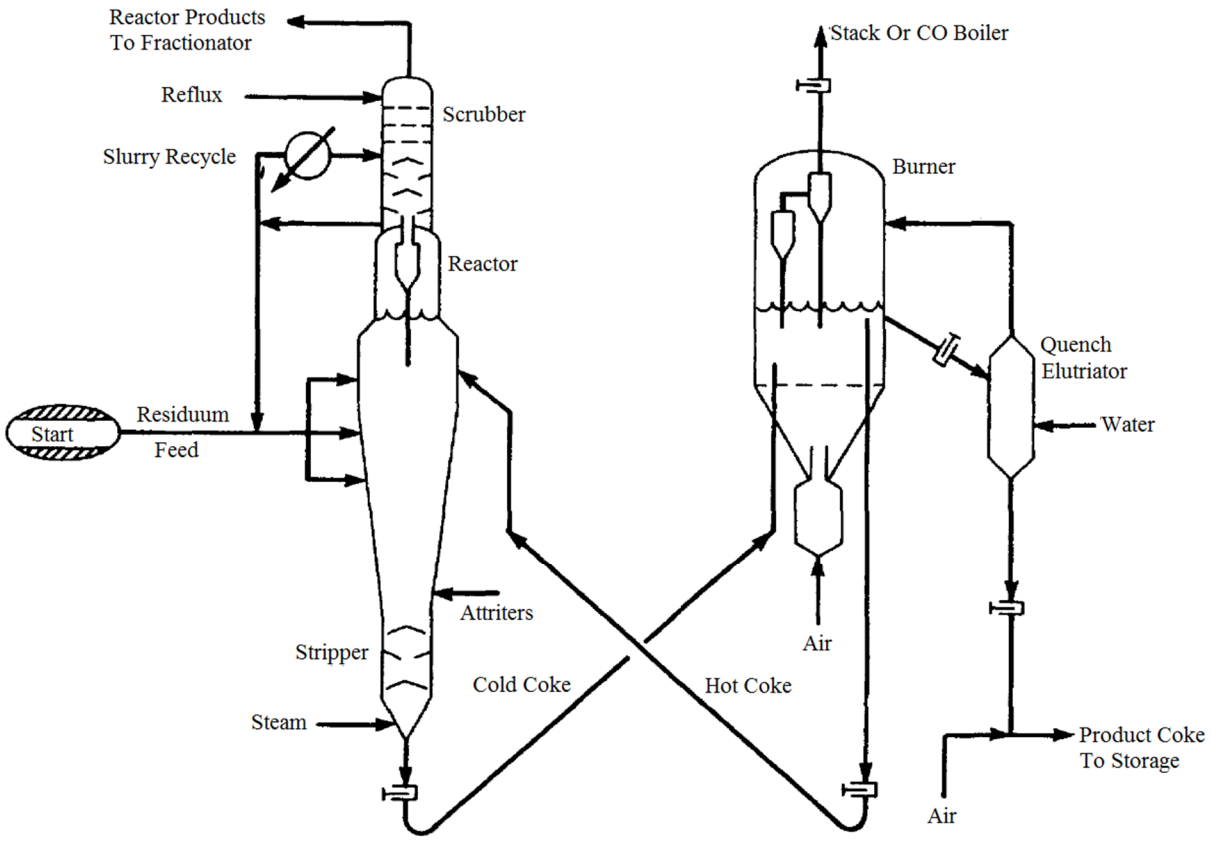

Figure 1-2. Schematic of fluid coking process, modified from Matsen (1996).

The composition of coke is directly influenced by the bitumen feedstock composition. Athabasca bitumen can contain more than 7% w/w solids. The solids consist primarily of aluminosilicate clay particles partially coated with polar and aromatic toluene-insoluble organic matter. These properties allow bitumen to complex with both oil and water. Bitumen end-cuts also have a significant sulfur content (7.2% w/w) that includes thiophenic, sulfide, and mercaptide compounds (Zhao et al., 2002).

Fluid petroleum coke produced at the Mildred Lake upgrading facility exhibits a fine sandy texture with smooth, uniformly spherical, well-sorted, framboidal grains (Har, 1981; Kessler and Hendry, 2006). This coke is composed largely of organically-bound C (84 ± 2.4 %) and S (7.0 ± 0.3 %), and contains lesser amounts of inorganically-hosted Si (9210 ± 3050 mg kg^{-1}), Al (5980 ± 1190 mg kg^{-1}), Fe (4760 ± 1180 mg kg^{-1}), and Ti (1380 ± 430 mg kg^{-1}). Coke also contains a suite of trace elements, of which V (1300 ± 120 mg kg^{-1}) and Ni (230 ± 80 mg kg^{-1}) are the most abundant.

1.5.2 Geological Source of Trace Metals

Trace metals such as V and Ni occur as organic complexes in the initial bitumen feedstock. Athabasca oil sands bitumen hosts a variety of V- and Ni-porphyrin complexes and chelated asphaltene-associated compounds (Zhao et al., 2002). These transition metals can be incorporated into tetrapyrrole porphyrin molecules because of the small ionic radii of VO^{2+} (0.63 Å) and Ni^{2+} (0.69 Å), the abundance of V and Ni in anaerobic marine depositional settings, and their favourable electronic configurations (Lewan and Maynard, 1982). Furthermore, as the redox potential of the depositional setting decreases, transition metals ions such as Fe^{3+}, Cu^{2+}, and Mg^{2+}, which can form complexes with ligands such as porphyrins, undergo reduction or exchange and are mobilized. This process leaves vanadyl (VO^{2+}) and nickelous (Ni^{2+}) ions as primary competitors for the ligand binding sites (Wehrli and Stumm, 1989). These ions form very strong covalent bonds with porphyrin binding sites (Lewan and Maynard, 1982).

While the trace metals found in coke are the same as those found in bitumen, the concern with petroleum coke is that these trace metals are preferentially concentrated into the coke during upgrading (Booz-Allen & Hamilton Inc., 1982; Dechaine and Gray, 2010). Vanadium is found in the V(IV) oxidation state as the VO^{2+} ion in porphyrin complexes. Depending on the redox setting of the original depositional environment, either VO^{2+} or Ni^{2+} porphyrins are preferentially formed. In strongly-reducing, S-rich depositional settings, VO^{2+} porphyrins would be generated. In weakly-reducing environments, V could be oxidized to V(V) which forms more labile aqueous complexes, implying that Ni^{2+} would be preferentially incorporated into porphyrin molecules (Filby, 1994). Only bitumen derived from Type I and II kerogen – lacustrine algal and marine planktonic respectively – has been found to contain appreciable levels of V and Ni since terrestrially generated kerogens are more readily degraded, resulting in metal release (Lewan and Maynard, 1982).

Unlike other metallated organic complexes, tetrapyrroles such as VO^{2+} and Ni^{2+} porphyrin complexes have high thermal stability, acid resistance, and are inert with regards to cation exchange behaviour (Lewan and Maynard, 1982). Despite this stability, it has also been proposed that during bitumen maturation in the source formation, metalloporphyrin decomposition could potentially release VO^{2+} and Ni^{2+}. These ions could form metal-asphaltene complexes or complexes with other polar molecules such as naphthenic acids (Filby, 1994). While present in all fractions of Athabasca bitumen, 76% of V is found in the asphaltene fractions and 23% of the V

is found in the pentane-soluble maltene fraction, implying an important non-porphyrinic component (Filby and Strong, 1991).

1.5.3 Redox Geochemistry of Vanadium and Nickel

Vanadium exhibits complex redox-sensitive geochemical behaviour owing primarily to the range of possible oxidation states and ability to form a variety of aqueous oxyanions and oxycations. Vanadium can exhibit oxidation states ranging from V(-I) to V(V), but the most common in naturally-occurring redox environments are V(V) and V(IV) (Li et al. 2007). This couple is used as a redox indicator because the equilibrium between the two oxidation states often occurs at Eh-values observed at the sediment water interface in natural soil-groundwater systems (Wehrli and Stumm, 1989). Hydrolysis products of V(V) are primarily oxyanionic and include $VO(OH)_3^0$, $VO_2(OH)_2^{1-}$, $VO_3(OH)^{2-}$, and VO_4^{3-} (Wehrli and Stumm, 1989; Aide, 2005). Vanadium in the V(V) oxidation state is protonated below pH 5, but at very low pH V(V) exists primarily as VO_2^{1+} (Li et al., 2007). Above pH 3.5, the dominant V(V) species are VO_3^{1-} and VO_4^{3-} (Blackmore et al., 1996). Polynuclear V species such as metavanadates and decavanadates can form at V concentrations greater than ~10^{-3} M, which is much higher than values typical for natural waters (10^{-8} to 10^{-6} M) (Baes and Mesmer, 1976; Wehrli and Stumm, 1989). Hydrolysis products of V(IV) are primarily oxycationic and include VO^{2+}, $VO(OH)^{1+}$ and $VO_2(OH)_2^{2+}$ (Wehrli and Stumm, 1989; Aide, 2005). At low pH, V(IV) exists primarily as VO^{2+} (Li et al., 2007). The VO^{2+} cation is a very hard Lewis acid and thus tends to coordinate with oxygen donor atoms. It also forms strong complexes with both soluble organic chelates and hydrous oxide particles (Wehrli and Stumm, 1989). The VO^{2+} ion is the most stable diatomic ion known to exist in nature, and generally exists in the form of a tetragonal bipyramidal species such as $VO(H_2O)_5^{2+}$ (Baes and Mesmer 1976; Aide 2005). Inorganic V(IV) is easily and completely oxidized by O_2 in air and aqueous solutions above pH 7 (Li et al., 2007). The V^{3+} ion is only stable at very low pH under very reducing conditions, or as a substituting lattice component of selected primary minerals (Aide, 2005).

Unlike V, Ni does not exhibit particularly complex redox geochemistry. Nickel(II) is the dominant oxidation state found in the environment. It is soluble and present as Ni^{2+} in most natural waters, except at pH>10 where it can be found as Ni(II) hydroxide. Nickel speciation is controlled more by the presence of ligands than by redox conditions. Given the inherent importance of carbonate in groundwater systems, it should be noted that Ni-CO_3 compounds are

thermodynamically stable in alkaline water, though there is some debate over the quantification of this stability (Hummel and Curti, 2003).

1.5.4 Release and Attenuation of Metals

One of the first laboratory-based leaching studies involving Syncrude petroleum coke suggested that metals and inorganic ions found in the coke matrix were essentially unleachable (Chung et al., 1996). While more recent studies have indicated that this is not the case, sequential extraction experiments (Kessler and Hendry, 2006) did partially corroborate the findings of Chung et al. (1996). The majority of elements were found to be strongly bound to the coke matrix; more than 50 % of the total content was still present in the residual fraction after extraction. However, Mn, Fe, and Ca were more weakly bound to the matrix; 20 % to 50 % of these elements were found in the water-soluble, acid-extractable, or reducible fractions. This study also examined the physical characteristics of Syncrude fluid coke and hypothesized that the smaller size fraction of coke particles may account for more adsorption of trace metals due to increased relative surface area (Kessler and Hendry, 2006).

Comparison of coke from different field conditions showed that aging and weathering were not major factors in the evolution of geochemical conditions (Chung et al., 1996). Also, simulated accelerated weathering was not found to increase metal leaching (Squires, 2005). Despite low leaching potential (3.6-10.8 mg kg^{-1}) relative to total elemental content (~1300 mg kg^{-1}), elevated dissolved V concentrations can occur. A comparison of field lysimeter studies with laboratory leaching experiments confirmed that the V concentration in Syncrude coke pore water could generally be attributed to the water soluble fraction of metals in solid fluid coke (Kessler and Hendry, 2006).

The complex chemical relationship between coke and OSPW must be better understood to be able to predict the partitioning of contaminant species between these two phases. In general, OSPW can be defined as water which has been in contact with oil sands or formation water, has been in a tailings deposit or settling basin, or has come into contact with groundwater or precipitation in the landscape. There are multiple sorption mechanisms by which dissolved metals may be attenuated by coke particles (Zubot et al., 2012). The first is the adsorption of aqueous metal species directly onto the carbon of the coke matrix. Many studies have been performed to understand the sorptive characteristics of coke, activated coke, and other similar carbonaceous materials.

Experiments have been performed to assess the sorptive behaviour of both coke and activated coke. A review of various fluid coke activation techniques showed that physical activation by steam or chemical activation by a KOH solution were most effective in directly increasing surface area. Other activation methods which employed strong oxidizing reagents like H_2O_2 and HNO_3 were less favourable with regards to the direct creation of porosity. Rather, these methods altered the coke matrix surface chemistry resulting in increased sorption of cationic species like NH_4^+ (Rambabu et al., 2013). Activated fluid coke can be generated for use as an effective adsorptive treatment option for organic materials such as less-biodegradable NAs in OSPW (Gamal El-Din et al., 2011). However, these activated coke products were found to release low levels of metals such as V (~20 ppb) and Ni (~200 ppb) (Small et al., 2012). The effect of combining coke and zero-valent iron (ZVI) for the purposes of OSPW treatment has been studied by Pourrezaei et al. (2014). Coke mediates the transfer of electrons between ZVI and NAs in OSPW, meaning that it could serve as both an adsorption and oxidation site for these organic compounds. Although trace metals were initially released from the coke, subsequent attenuation by ZVI was observed (Pourrezaei et al., 2014).

The second proposed mechanism of V attenuation is the preferential adsorption of aqueous V species to metal (oxyhydr)oxides hosted within the coke matrix. Vanadium adsorption onto various metal (oxyhydr)oxides has been studied independently of petroleum coke (Wehrli and Stumm, 1989; Blackmore et al., 1996). Solution pH has a strong influence on the adsorption behaviour of V onto metal oxides. Experiments assessing pH-dependence of V adsorption onto Ti- and Fe-oxide materials indicated that vanadate adsorption was most favourable at pH 3.0-3.5. This is consistent with electrostatic attraction between protonated metal sites and aqueous vanadate oxyanions (Naeem et al., 2007). By comparison, the pH of process water in the coke deposits being studied in the current research varies from circumneutral to slightly alkaline.

The adsorption of V(V) species onto amorphous Fe oxyhydroxides and hydrated amorphous Mn oxides was found to decline in more alkaline solutions despite these same species being adsorbed strongly at pH values above their respective pH_{PZC} values. This finding suggests that V(V) adsorption to these minerals is via inner-sphere mechanisms (Blackmore et al., 1996). This decrease at high pH is likely due to adsorptive competition between aqueous V oxyanions and hydroxide ions (Naeem et al., 2007). The VO_2^+ ion has been proposed to adsorb to oxide sites via a monodentate mechanism at low pH:

$$> MOH + VO_2^+ \leftrightarrow > MO - VO_2 + H^+$$ (Wehrli and Stumm, 1989)

At high pH, V(V) can behave much like phosphate, once again via a monodentate mechanism:

$$> MOH + VO_3(OH)^- \leftrightarrow > MO - HVO_3^- + OH^-$$ (Wehrli and Stumm, 1989)

Conversely, V(IV) as VO^{2+} has been proposed to adsorb to oxide sites via a bidentate mechanism:

$$\begin{matrix} > MOH \\ > MOH \end{matrix} + VO^{2+} \leftrightarrow \begin{matrix} > MO \\ > MO \end{matrix} VO + 2H^+$$ (Wehrli and Stumm, 1989)

It is important to note that findings from these laboratory-based studies of contaminant adsorption onto carbonaceous materials and metal (oxyhydr)oxide materials may not be directly applicable to adsorption processes in field-scale petroleum coke deposits. However, many of the redox-controlled mechanisms of release and attenuation described herein may play a role in determining the spatial distribution and speciation of contaminants in the field setting.

1.5.5 Environmental Toxicology

Coke is currently stored at the Mildred Lake mine in large deposits either in proximity to or directly in contact with large bodies of OSPW, such as the Mildred Lake Settling Basin. Both coke and OSPW will be incorporated into the post-mining landscape where they may release potentially toxic contaminants into the surrounding environment. Leachates with elevated V and Ni concentrations collected from lysimeters and wells at various coke deposits at the Mildred Lake mine were acutely toxic to *Ceriodaphnia dubia* (Puttaswamy et al., 2010). Higher bicarbonate concentrations correlated to greater V leaching (Puttaswamy and Liber, 2012). The presence of sulfate inhibited V uptake by the *C. dubia*; however, Ni toxicity increased at higher bicarbonate concentrations. The relative proportions of the dominant V oxyanions, $(VO_2(OH)_2^{1-}$ and $VO_3(OH)^{2-})$, also varied with increasing bicarbonate concentration (Puttaswamy and Liber, 2012).

Aquatic and terrestrial revegetation is an important aspect of mine closure; therefore, it is important to understand the effects of mine wastes on plants and animals. Plants grown in coke exhibited multiple stress symptoms attributable to its physical and chemical properties. *Triticum aestivum* (wheat species) and *Deschampsia caespitosa* (grass species) displayed water stress likely as a result of poor water retention due to low organic matter and well-sorted grains. These plants also suffered from nutrient deficiencies, loss of biomass, and uptake of potentially phytotoxic concentrations of V (9.3-18 mg kg^{-1}) and Ni (47-69 mg kg^{-1}). Emplacement of a reclamation soil cover over coke greatly reduced these stress symptoms and is therefore recommended for longterm

coke landform revegetation programs (Nakata et al., 2011). Constructed wetlands will play an important role in oil sands mine reclamation landscapes, so the fate of potentially-toxic metals in these settings must be better understood. Sediments and oil sands fine tailings capped with coke in constructed wetlands were associated with uptake of V and Ni in a macrophytic green alga and benthic invertebrates (Baker et al., 2012).

1.5.6 Characterization of Coke Deposit Water Provenance

Stable isotopes of water, $\delta^{18}O$ and $\delta^{2}H$ (δD), were used to characterize the hydrological regime at the study site. Fractionation of the stable isotopes of water occurs primarily during physical phase changes, (i.e. evaporation, condensation, freezing, melting, and sublimation). The heavier isotopes (^{18}O and ^{2}H) become enriched in lower energy phases and become depleted in higher energy water phases. Enrichment and depletion are measured and reported as follows (Faure, 1998):

$$\delta^{18}O = \left(\frac{\left(\left(^{18}O/^{16}O\right)_{sample} - \left(^{18}O/^{16}O\right)_{std}\right)}{\left(^{18}O/^{16}O\right)_{std}}\right) \times 1000\ ‰ \qquad \text{Equation 1-1.}$$

$$\delta^{2}H = \left(\frac{\left(\left(\,^{2}H/\,^{1}H\right)_{sample} - \left(\,^{2}H/\,^{1}H\right)_{std}\right)}{\left(\,^{2}H/\,^{1}H\right)_{std}}\right) \times 1000\ ‰ \qquad \text{Equation 1-2.}$$

A linear relationship is typically observed between $\delta^{2}H$ and $\delta^{18}O$ values since H and O experience fractionation events together. This relationship can generally be referred to as the local meteoric water line (LMWL) for a finite geographic region. Meteoric water samples from a particular, distinct geographic region tend to plot along this line. The LMWL is geographically variable due to differences in latitude, climate, and the source water bodies for atmospheric water vapour. While all meteoric water samples lie along this line, the actual values can vary substantially and can be clustered at signature values. The isotopic signatures of water samples from the Syncrude Mildred Lake area have been catalogued and characterized (Baer, 2014). The signature of OSPW is distinguishable from precipitation because of the repeated evaporation and condensation steps encountered during its use throughout processing (Baer, 2014). Coke deposit pore water depth profiles of $\delta^{2}H$ and $\delta^{18}O$ were used in the current research to determine the depth of precipitation infiltration and the vertical extent of the mixing zone between infiltrating precipitation and OSPW.

1.5.7 Solid-Phase Analyses of Petroleum Coke

A variety of analytical and spectroscopic techniques have been employed to study and characterize petroleum coke and related carbonaceous materials derived from bitumen and crude oil fractions. Many techniques have been used to analyze the carbonaceous fraction of petroleum coke but only those employed in the present study are discussed herein. X-ray diffraction (XRD) has been used extensively to study the asphaltenic fraction of petroleum materials such as crude oil, coke, and fly ash (Tanaka et al., 2004; Andersen et al., 2005). Asphaltenic materials often exhibit a broad peak at ~20° 2θ (Cu Kα source) corresponding to a variety of paraffin compounds with a second broad peak at ~26° 2θ corresponding to aromatics (Wiehe and Liang, 1996).

Raman spectroscopy is another technique which can be used to elucidate the components and proportions of specific asphaltenic compounds within heterogeneous carbonaceous materials (CM). This method assesses the relative magnitude of bands (peaks) corresponding to resonant modes of carbon atoms within aromatic molecules. Disordered CM, such as coke being studied in the current research, display two main broad bands corresponding to stretching vibration in the aromatic layers (G band, 1590 cm^{-1}) and in-plane structural defects (D1 band, 1350 cm^{-1}) (Beyssac et al., 2003; Bouhadda et al., 2007). The relative width and intensities of the G and D Raman bands in disordered CM vary systematically as a function of carbon type and processing temperature and can therefore be employed in characterizing such materials (Vidano and Fischbach, 1978). Raman spectroscopy has also been used in the investigation of V oxides (Sanchez et al., 1982) and VO^{2+} porphyrins (Macor et al., 1990; Rankin and Czernuszewicz, 1993). It has similarly been used to characterize bonding mechanisms in V compounds found in natural systems such as oxovanadyl complexes between VO^{2+} and organic ligands (Baran, 2001).

1.5.8 Comportment of V and Ni Phases in Petroleum Coke

Vanadium and Ni are the highest-concentration potentially-hazardous trace metals in petroleum coke, so their release from coke deposits could pose a serious environmental risk. However, since V exhibits among the most complex redox chemistries of the elements found in coke, understanding its mobility is not trivial. A range of synchrotron-based spectroscopic techniques have been used to characterize V and Ni compounds such as porphyrin complexes and oxides. However, to the best of my knowledge, synchrotron analyses of petroleum coke have not yet been published.

Vanadium and Ni are present as both metalloporphyrins and non-porphyrinic species in the asphaltenic fraction of bitumen (Tooulakou and Filby, 1988). Given their resilience to degradation, porphyrinic compounds or other organo-metallic compounds may survive the fluid coking process and become an important longterm reservoir of V and Ni in coke. X-ray spectroscopic methods provide evidence that much of the V is present in petroleum and asphaltene samples as a vanadyl ion (VO^{2+}) coordinated to four N ligands in a square planar arrangement (Dechaine and Gray, 2010). The Ni coordination is more variable; UV-visible spectroscopy has shown that this element may be more prevalent as a non-porphyrinic species in asphaltenic aggregates. Non-porphyrin species of Ni and V within the asphaltenic matrix may consist of metallated N, O, and S functional groups or metallated naphthenic salts. Metalloporphyrin molecules may become either structurally incorporated into, or hydrogen-bonded to the surface of, complex asphaltenic aggregates, resulting in either square-planar or even octahedral metal coordination (Tooulakou and Filby, 1988).

In general, the most common porphyrin classes (Figure 1-3) found in petroleum systems, and therefore anticipated to be found in coke, are (deoxophylloerythro)etioporphyrins (Pearson and Green, 1993). An X-ray absorption spectroscopy near-edge structure (XANES) study of both fresh and aged bituminous material showed that the predominant VO^{2+} porphyrin was a vanadyl octaethyl porphyrin (VOOEP), a common etioporphyrin. While aging did not lead to V oxidation state changes, it has been found to cause the partial aromatization of VOOEP to vanadyl (meso)-tetraphenyl porphyrin (VOTTP) (El Béze et al., 2012).

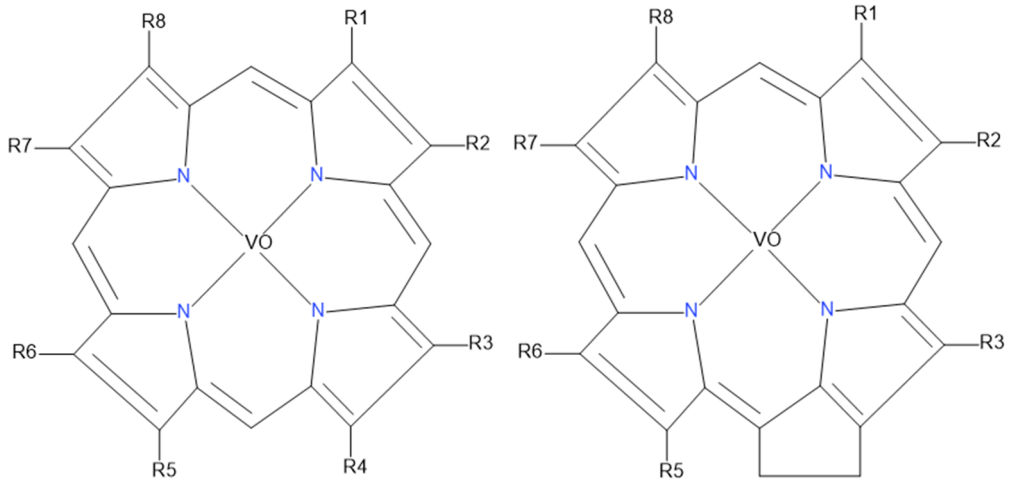

Figure 1-3. The most common porphyrin classes in petroleum systems are common etioporphyrins (left) and deoxophylloerytrho-etioporphyrins (right). R indicates location of functional group. Vanadyl (VO^{2+}) variety shown here (modified from Pearson and Green, 1993).

The high temperatures reached during the coking process, as well as physical and chemical weathering in the environment, may liberate V and Ni from porphyrin molecules or other functional groups within the asphaltenic fraction. Vanadium oxides have been thoroughly studied using X-ray absorption spectroscopy (XAS) (Wong et al., 1984). Due to the electronic structure and atomic coordination of V, there is a prominent pre-K-edge feature in the associated XAS spectra, the magnitude and position of which is strongly correlated with oxidation state (Sutton et al., 2005). The V oxidation state can be systematically determined by peak-fitting of this pre-edge feature and comparing its magnitude to the K-edge white line magnitude (Chaurand et al., 2007). Extended X-ray absorption fine structure (EXAFS) has also been utilized to investigate bonding distances and V coordination in V oxide compounds (Tanaka et al., 1988).

1.5.9 Assessing Micro-scale Heterogeneities in Element Speciation

The current research examines the possibility that the concentration and speciation of V and other redox-sensitive elements (i.e. S, Fe) may exhibit spatial variation at the micron scale. While micron-scale heterogeneities in elemental speciation have not previously been investigated for coke, various techniques have been developed for assessing such variability in geological materials. Micro X-ray fluorescence (μXRF) maps are commonly used to examine micro-scale spatial distribution of elements in a wide range of materials.

The process of oxidation state, or speciation, mapping is performed similarly by collecting multiple μXRF maps of the same region on a sample, but at different incident X-ray photon energies (Sutton et al., 1995). These target energies are selected to correspond to features in the XANES spectra of the element of interest which are known to fluctuate in relative magnitude depending upon oxidation state or local coordination. By comparing these maps, it is possible to gain insight into the distribution of different species at the scale of individual grains (Mayhew et al., 2011). Sulfur has been shown to be highly amenable to μXRF oxidation state mapping because of its range of possible species and its redox-sensitive XANES spectra with large energy difference between oxidation states (Zeng et al., 2013).

An innovative method has been used to compare multiple micro-XRF maps, thus extending the capabilities of this process even further. X-ray fluorescence counts taken on a pixel-by-pixel basis from a set of *N* spatially-coincident maps can be plotted as coordinates in an *N*-dimensional space. *N*-dimensional cluster or regression analyses can then be performed to determine the quantity and relative proportions of distinct phases. This can be performed using micro-XRF maps

of different elements or using a set of oxidation state maps for different species of one element. (Manceau et al., 2002; Isaure et al., 2002). The current research will attempt to employ these techniques to assess micro-scale spatial variability in V speciation in coke to determine whether potentially-mobile V phases are likely to be released. Nickel is likely to occur exclusively as Ni(II); therefore, oxidation state mapping is not relevant.

1.6 Research Statement

This research examines how solid-phase trace metal speciation and aqueous-phase redox geochemical conditions control metal mobility in petroleum coke deposits.

Hypothesis 1: Variation in geochemical characteristics of fluid petroleum coke is linked to bulk trace element speciation in this coke.

- Objective 1a: Provide a detailed baseline assessment of bulk geochemical and mineralogical properties of coke from deposits.
- Objective 1b: Assess deposit-scale variability of these properties.

Hypothesis 2: Trace element mobility is directly influenced by redox geochemical conditions and micro-scale variations in the chemical hosting mechanism.

- Objective 2a: Establish a relationship between coke deposit pore water redox geochemical conditions and trace element mobility.
- Objective 2b: Develop an understanding of micro-spatial variations in trace element concentration, speciation, and coordination within coke particles.

1.7 Organization of Thesis

This manuscript-style thesis is presented in four chapters. The first introduces the thesis topic and reviews previous studies of relevance to the current research. The second chapter describes the geochemistry of coke and the bulk speciation and hosting mechanisms of trace metals. The third chapter examines micro-scale variations in trace metal geochemistry and describes the relationship between redox geochemical conditions and metal release. Both the second and third chapters begin by providing a background of relevant previous work performed in the respective fields of research followed by a description of pertinent fieldwork, lab methods, sample processing, and data analysis tools used to test the hypothesis in each chapter. Both chapters then present the results and discuss the geochemical implications. The fourth and concluding chapter integrates the key findings of the current research in order to understand the significance of this research within the field, and proposes potential future work.

CHAPTER 2 GEOCHEMICAL CHARCTERISTICS OF OIL SANDS FLUID PETROLEUM COKE

2.1 Introduction

Oil sands petroleum coke is generated during the upgrading of bitumen to synthetic crude oil. Greater than 20 kg of coke are generated per barrel of oil produced. Approximately 21 % of this coke is used as fuel at on site upgrading facilities, and 2.2 M tonnes of coke are deposited on site annually (AER, 2015). Coke stockpiles in the Athabasca oil sands regions are currently 100 M tonnes (AER, 2015) and are projected to amount to ~1 km^3 over the lifespan of oil sands mining and upgrading in the Athabasca oil sands region (Fedorak and Coy, 2006). Coke is primarily composed of aromatic, asphaltenic, and amorphous C (80 – 85 %). However, S (4 – 8 %) and N (1 – 4 %) are also abundant (Jack et al., 1979a; Anthony, 1995). Coke also contains Si, Al, Fe, Ti, Ca, and a suite of trace metals (Zubot et al., 2012) because of the bitumen feed composition and the concentrating effect of the coking process.

Vanadium and Ni are generally the most abundant trace metals in coke, as in many petroleum deposits derived from organic-rich marine sediments (Lewan and Maynard, 1982). These metals are hosted in compounds ranging from porphyrins to metallated asphaltenic molecular aggregates in bitumen. The coking process sequesters these large and complex asphaltenic phases diverting most trace metals into the coke phase while removing lighter C compounds (Anthony, 1995; Dechaine and Gray, 2010). The types of V- and Ni-complexes and the diversity of metal binding sites in many petroleum systems, including oil sands bitumen, have previously been studied (Saraceno et al., 1961; Millson et al., 1966; Jacobs and Bachelor, 1984; Fish et al., 1986; Reynolds et al., 1987; Pearson and Green, 1993; Miller and Fisher, 1999; Caumette et al., 2009). However, the fate of these complexes is poorly understood following coking, deposition in reclamation landscapes, and weathering under environmental conditions.

The potential toxicity of trace metals in coke to aquatic, benthic, and terrestrial organisms living in contact with coke deposits or coke-amended reclamation landforms is a key motivator to better understand the bulk form of these metals. Coke pore water can contain elevated concentrations of V and Ni (Puttaswamy et al., 2010; Nakata et al., 2011; Puttaswamy and Liber,

2011; Baker et al., 2012; Puttaswamy and Liber, 2012; Jensen-Fontaine et al., 2014). Constructed wetlands containing native sediments, oil sands mature fine tailings, and fluid fine tailings, capped or amended with coke are expected to play an important role in mine-closure landscapes (Fedorak and Coy, 2006). In situ microcosm experiments showed that organisms such as algae and burrowing benthic invertebrates can uptake metals from coke and coke-amended wetland sediments (Baker et al., 2012). Since coke is currently stockpiled sub-aerially, wind-blown coke also contributes to the spread of contaminants, such as polycyclic aromatic hydrocarbons, throughout the Athabasca oil sands region (Zhang et al., 2016). Understanding the fate of metals during coking and thermal cracking of asphaltenic molecules in Athabasca bitumen can help inform longterm coke storage conditions in reclamation landforms. The product asphaltenes in coke, which dominate the carbonaceous component of coke, retain metallo-porphyrins from the bitumen source (Asaoka et al., 1983; Bausell et al., 1992). However, the removal of vanadyl (VO^{2+}) porphyrin metal centres and the breakage of weak organic S bonds were found to be the main reactions leading to the breakdown of the irregular and structurally-weaker portions of asphaltenic micelles. The vanadyl ions released from these portions may remain loosely bound or could be free to form complexes with non-asphaltenic, or even inorganic, phases during coking. Nitrogen sites and organo-metallic Ni sites are less important in mediating these cracking reactions, remaining more intact within asphaltenic micelles (Asaoka et al., 1983).

Coke is primarily produced via delayed coking, fluid coking, or flexicoking. This study focused on fluid coke, which differs from delayed coke both in production method and particle size and morphology (Jack et al., 1979a; Blaser, 1992). Fluid coking is performed by circulating coke particles between a burner vessel and a coker vessel, continuously removing any particles which grow too large (Blaser, 1992). Conversely, delayed coking involves a brief thermal cracking step in a fired heater followed by a longer cracking cycle in an insulated coke drum. It is performed at a slightly lower temperature (415-450 °C, versus 480-565 °C for fluid coke) resulting in a higher volatile content in delayed coke (7-13 %) than in fluid coke (4-6 %) (Anthony, 1995). Bulk elemental analyses of delayed coke showed around 30 % less V and Ni than in fluid coke (Jack et al., 1979a). Flexicoking is different than fluid coking only in that the coke undergoes an additional gasification step to decrease C, S, and volatiles content.

The current research aimed to link variations in geochemical characteristics of fluid petroleum coke to bulk trace element speciation in coke. The objectives of this research were to

provide an up-to-date assessment of geochemical and mineralogical properties of Syncrude fluid coke from both active and inactive coke deposits and to assess the deposit-scale spatial variability of these properties.

2.2 Study Site

Coke from three deposits at the Syncrude Canada Limited Mildred Lake oil sands mine, located approximately 40 km north of Fort McMurray, Alberta, Canada was investigated (Figure 2-1). Coke Beach (CB) (1.5 km^2 in 2015) is an uncovered active deposit. Coke Watershed (CW) (0.28 km^2) and Coke Cell 5 (CC5) (0.90 km^2) are inactive deposits with established vegetated covers. These deposits were selected because differences in topography and cover result in a range of hydrological and redox geochemical conditions. The geochemical and hydrological characteristics of coke deposits are influenced by aspects of the fluid coking process itself. As fluid coke particles grow in size through the addition of successive layers, they are removed from the cycle and slurried with process water to deposition areas. This coke is therefore a uniform, fine sandy texture, characterized by sub-spherical particles typically ranging from 0.08 – 0.3 mm, though occasionally as large as 1 mm (Furimsky, 1998; Kessler and Hendry, 2006). Particle size distribution in coke deposits can be influenced by mechanical sorting during sub-aerial hydraulic deposition and subsequent aeolian sorting (Kessler and Hendry, 2006).

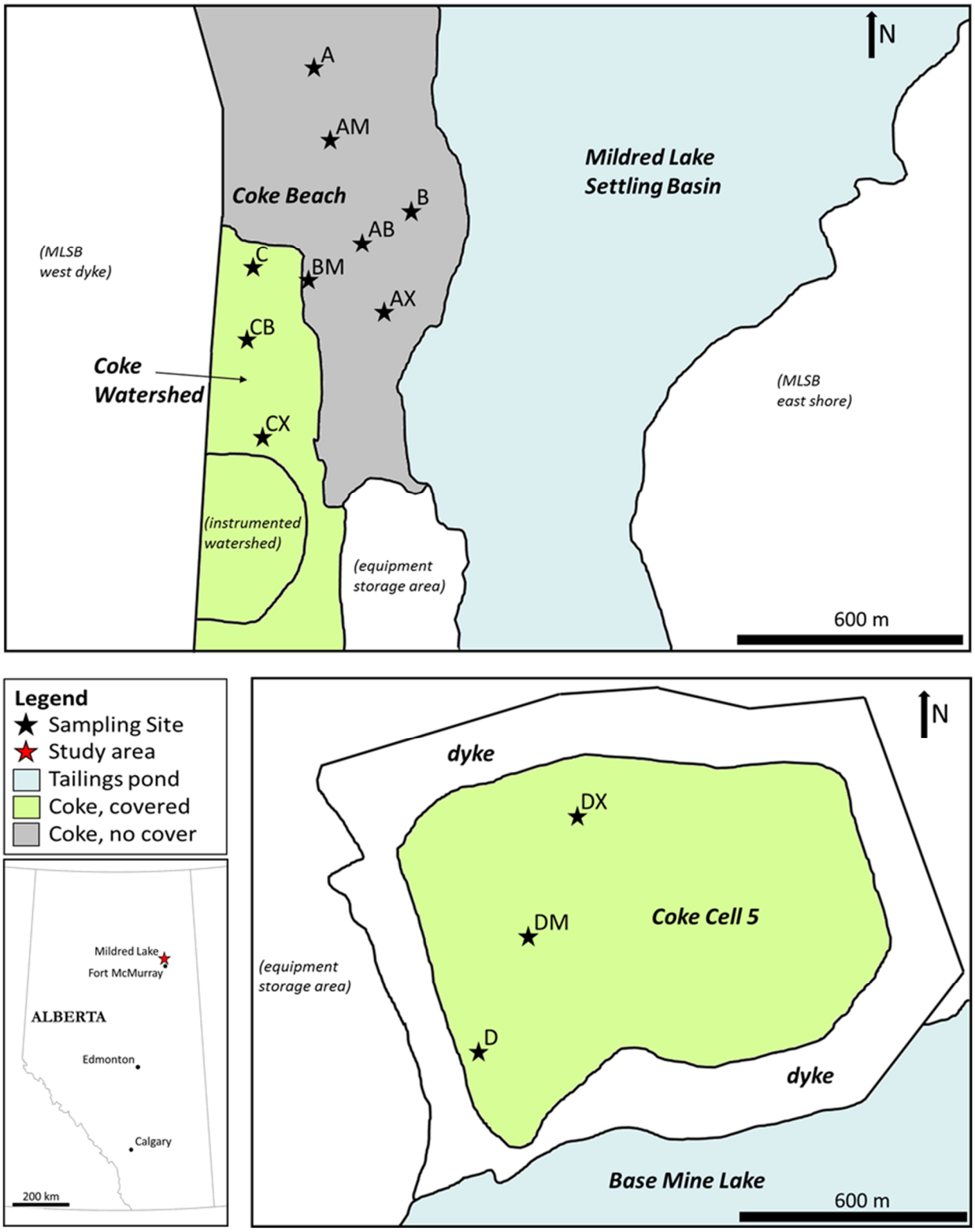

Figure 2-1. Plan view of field site location in Alberta, Canada, and core sampling locations at Coke Beach, Coke Watershed, and Coke Cell 5.

2.3 Materials & Methods

2.3.1 Sample Collection

Core samples were collected along transects of the three coke deposits, with specific locations selected to capture spatial variability in geochemical conditions (Figure 2-1). Sites A, AM, AB, and AX form a ~700 m transect along Coke Beach. Sites C, CB, and CX form a ~450 m transect along Coke Watershed. Sites B, AB, BM, and CB form a ~550 m transect extending inland from the Mildred Lake Setting Basin. Sites D, DM, and DX form a ~700 m transect across Coke Cell 5. Core samples were collected using an amphibious track-mounted sonic drill rig in July 2014. Sequential 2 m long cores were collected to a depth of 8 m at 12 locations CB (n = 6), CW (n = 3), and CC5 (n = 3). In cases of vibration-induced compaction of unsaturated coke, one bulk sample was collected from the end of the interval for which the true depth was known. The cores were subsampled at 0.5 m intervals and transferred into 1L high-density polyethylene (HDPE) bottles. The bottles were sealed, transported on ice to the University of Saskatchewan, and stored at -18°C until analysis. Prior to analysis, the samples were transferred into an anaerobic chamber, where they were thawed and vacuum-filtered. Subsamples were then transferred to 40 mL amber glass vials, frozen, and then freeze-dried for 24 h.

2.3.2 Elemental Analyses

Bulk elemental analyses were performed for samples from a range of depths and locations at CB (n = 17), CW (n = 3), and CC5 (n = 8). These analyses provided the preliminary information to identify deposit-scale and depth-dependent changes in coke geochemistry. Three of these samples were sent as blind triplicates to assess reproducibility of results. Total C and S contents were determined using a LECO CS230 analyzer (LECO Corporation, 2008). Major element concentrations were determined by a lithium borate fusion digestion with inductively coupled plasma optical emission spectrometry (ICP-OES) detection. Trace element concentrations were quantified using a lithium borate fusion digestion with inductively-coupled plasma mass spectrometry (ICP-MS) detection, and aqua regia digestion with ICP-MS detection (Table 2-1).

Table 2-1. Analytical methods used for bulk elemental analyses and elements that were analysed. Parentheses indicate analytes with mean concentrations <5 mg kg^{-1} or below detection limit.

Method	Analyte
LECO CS230	Total C, Total S
Li borate fusion ICP-OES	Si, Al, Fe, Ti, Ca, K, Na, Mg, P, Mn, Cr
Li borate fusion ICP-MS	V, Ni, Zr, Sr, Ba, Ce, La, Nd, Co, Y (Be, Cs, Dy, Er, Eu, Ga, Gd, Hf, Ho, Lu, Nb, Pr, Rb, Sc, Sm, Sn, Ta, Tb, Th, Tm, U, W, Yb)
Aqua regia ICP-MS	Mo, Cu, Zn, Pb (As, Cd, Sb, Bi, Ag, Au, Hg, Tl, Se)

Bulk elemental analysis results were examined statistically using elemental correlation matrices and by comparing summary statistics for each deposit. Pearson correlation matrices were generated, in order to study the significance and robustness of correlations. A centred logratio transformation was first applied to the dataset; for every sample, each value was first divided by the geometric mean of all analytes for that sample, then the $\log_{10}$ of the resulting quotient was calculated. This transformation is used to "open" a "closed" dataset – such as a compositional dataset where all analytes must sum to ~100 % – by transforming the data such than analytes instead sum to zero.

2.3.3 Specific Surface Area Analyses

Brunauer-Emmett-Teller N_2 adsorption isotherms were measured using a Quanta Chrome Nova 2200e surface area analyzer (Brunauer et al., 1938). Coke samples (n = 13) representing the three deposits studied were freeze-dried and analyzed in order to determine if longterm field storage conditions, age, depth, weathering, saturation, or any other factors induce variation in surface area. Blind duplicates of six samples and lab duplicates of three samples were analyzed to confirm data reproducibility.

2.3.4 X-Ray Diffraction

X-ray diffraction (XRD) was performed using two different techniques to assess potential mineralogical hosts for trace elements within the coke matrix. Freeze-dried samples were first ground to <100 μm under an anoxic atmosphere. Conventional Cu Kα source XRD (λ = 1.54) was performed using a Panalytical Empyrean diffractometer, operated at 45 kV and 40 mA, with a Ni Kβ filter and a 0.5° incident beam slit size. Samples were slurried with methanol and mounted on a glass plate for analysis. Data was collected as 1-dimensional diffraction patterns from 3-80° 2θ with a 2θ resolution of 0.016°.

Synchrotron-based powder XRD was performed at beamline 08-B1-1 (CMCF BM) at the Canadian Light Source. Samples were loaded into 0.8 mm diameter polyimide (Kapton) capillary tubes for analysis. Data were collected as 2-dimensional diffraction patterns using an incident beam energy of 18 keV ($\lambda = 0.68879$) and a Rayonix MX300HE area detector. Data reduction was performed using GSAS-II software (Toby and Von Dreele, 2013) by calibrating 2D patterns using a lanthanum hexaboride standard, subtracting the capillary background signal, and radially integrating the patterns using a 2θ resolution of 0.005°. Phase identification was performed using Match! software (Version 3.1.0) by Crystal Impact with the Crystallography Open Database (Gražulis et al., 2009).

2.3.5 Electron Micro-Analysis

Scanning electron microscopy (SEM) was used to assess the micro-scale morphology and internal structure of coke particles. A Phenom G2 Pure SEM was used to examine freeze-dried, uncoated, unground coke powder samples ($n = 4$) mounted on carbon tape. Electron microprobe analyses (EMPA) were employed to test the chemical composition of small crystalline oxide mineral particles hosted within the carbonaceous coke matrix. A JEOL JXA-8600 Superprobe was used to examine thin sections ($n = 5$) that were prepared previously for optical and spectroscopic studies. Sections were carbon-coated prior to analysis to render them homogeneously conductive.

2.3.6 Bulk XAS Analyses

Synchrotron-based bulk X-ray absorption spectroscopy (XAS) was performed at the Canadian Light Source (CLS). Vanadium and Ni K-edge XANES spectra were collected at the 06-ID-1 hard X-ray micro-analysis beamline (HXMA). Iron and S K-edge XANES spectra were collected at the 06-B1-1 soft X-ray micro-characterization beamline (SXRMB). Measurements were made using a beam spot size of ~1 mm (vertical) by ~3 mm (horizontal) at both beamlines. A set of samples representing a range of depths from the three coke deposits were studied. Samples AB000, AB200, AB700, CX050, CX300, CX500, DM050, DM550, DM950 correspond to locations (Figure 2-1) and depths (in cm below surface).

Samples prepared for V and Ni measurements at HXMA were freeze-dried. Approximately 0.1 g of sample was secured in beamline-specific Teflon sample holders with polyimide (Kapton) tape. Samples were stored under anoxic conditions and transported to the synchrotron in an anoxic vacuum container. Data were collected in fluorescence mode, using a 32-element Ge detector oriented orthogonally to the incident beam and at 45° relative to the sample. Absorption spectra

for V and Ni foils were collected in transmission mode simultaneously during sample spectra acquisition at the V and Ni K-edges respectively, to perform energy calibration on sample spectra. Samples prepared for Fe and S measurements at SXRMB were freeze-dried and ground using a mortar and pestle in an anaerobic chamber. Approximately 0.05 g of sample was mounted on carbon tape adhered to a conductive copper plate. Samples were stored under anoxic conditions and transported to the synchrotron in a vacuum container. Data were collected under high vacuum (-5 x 10^8 Torr) in both fluorescence yield (FY) and total electron yield (TEY) modes.

Data processing and analysis was performed using Athena software (Version 0.9.21), which is a component of the Demeter software package (Ravel and Newville, 2005). Energy calibration, pre-edge background subtraction and post-edge normalization were performed prior to linear combination fitting (LCF). A LCF fitting range of -25 eV to +60 eV relative to the K-edge was employed for all fitting, as this was found to capture the spectral features of interest in the XANES region. Individual component weights and the sum of weights were not constrained. The R-factor was the primary assessment of goodness of fit, but an individual component weight <0 or >1, a sum of weights far from 1, or large fitting residuals indicated a poor fit. Spectra for vanadyl octaethyl porphyrin (VOOEP), vanadyl tetraphenyl porphyrin (VOTPP), Ni octaethyl porphyrin (NiOEP), and Ni tetraphenyl porphyrin (NiTPP) compounds (Sigma-Aldrich, MO) were collected at HXMA. These standards were included in LCF to account for some of the expected variability of porphyrin complexes in coke.

Finite difference modelling of the near-edge structure (FDMNES) (Bunau and Joly, 2009) of the V and Ni porphyrin molecules were performed to assess the potential effect that distortions in the metallated porphyrin core have on the K-edge XANES spectra. Porphyrin molecular structures proposed by Molinaro and Ibers (1976), Meyer (1972) and Maclean et al. (1996) were used as the base cases for this modelling. Both organic and inorganic S standard K-edge XANES spectra were obtained from the European Synchrotron Research Facility XANES database, (i.e. Bohic et al., 2008). Iron K-edge XANES spectra for pyrite (FeS_2), magnetite (Fe_3O_4), and Fe(III) sulfate standards were collected at SXRMB, and spectra for ilmenite ($FeTiO_3$), akaganeite (β-FeOOH), and lepidocrocite (γ- FeOOH) were obtained from the Advanced Light Source (ALS) X-ray Microprobe Beamline 10.3.2 XAS Database.

2.4 Results & Discussion

2.4.1 Physical Characteristics

Specific surface area was generally quite low (< 9 m^2g^{-1}). This range was generally consistent with the values of 10 m^2g^{-1} (Har, 1981), 11 m^2g^{-1} (Fedorak and Coy, 2006), and 8 m^2g^{-1} (Pourrezaei et al.,2014) previously obtained for Syncrude fluid petroleum coke. Micro-pores are negligible in fluid coke (Har, 1981; Pourrezaei et al., 2014) and the measured surface areas are attributed to primary surfaces. The low surface area of fluid petroleum coke – compared to that of activated carbon materials (>750 m^2g^{-1}) – is attributed to low porosity (Pourrezaei et al., 2014). Pores measuring between 2 and 40 nm (mesopores) dominated surface porosity of coke and are therefore expected to play a significant role in adsorption reactions (Pourrezaei et al., 2014). Both increasing and decreasing trends with depth were observed at each site (Table 2-2). The observed depth trends may have been caused by subtle particle size gradation with depth as a result of hydraulic deposition.

Table 2-2. Coke particle specific surface area for various depths at four sampling sites (Fig. 2-1). SSA measurement error is ± 2 %.

Site	Depth (m)	Specific Surface Area ($m^2 g^{-1}$)
AB	0.0	0.09
	2.0	1.64
	4.5	3.95
	7.0	4.22
AM	2.0	3.98
	3.0	6.82
	6.5	0.50
CX	0.5	5.57
	3.0	1.96
	5.0	0.01
DM	0.5	8.51
	2.5	6.53
	5.5	7.20
	9.5	5.30

Scanning electron microscopy revealed distinct micro-scale structural heterogeneities within coke particles. Successive concentric sub-spherical layers are the primary observable morphological feature in cross-sections of coke particles (Figure 2-2a). Perpendicularly radiating

micro-structures were observed in the space between layers (Figure 2-2b). These structures are likely a result of material addition and rapid heating and cooling cycles during coking.

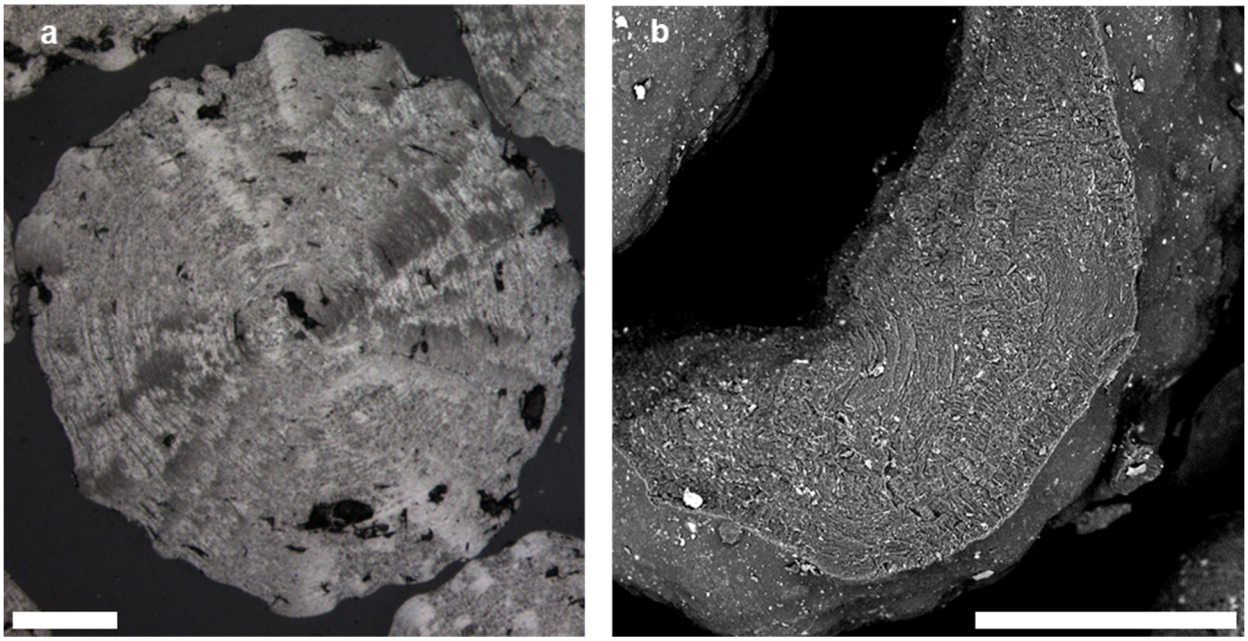

Figure 2-2. a) Optical reflected light image of coke particle section showing visible concentric ring micro-structure; b) Back-scattered electron image of interior of coke particle (broken open), showing perpendicularly-radiating micro-structures. Scale bars are 50 μm.

2.4.2 Chemical Characteristics

Bulk elemental analyses revealed that coke was composed of C, S, Si, Al, Fe, Ti, Ca, K, Na, Mg, and a suite of trace elements dominated by V and Ni (Figure 2-3) (Appendix A). The balance of the composition was likely comprised of other light, volatile elements H (1.50-1.67 %), N (1.3-1.6 %), and O (2.3-2.5 %) as was reported by Har (1981). Very similar volatiles contents were reported by Chung et al. (1996) and Kessler and Hendry (2006). Elemental concentrations are generally consistent with previous studies (Table 2-3). Nickel concentrations are the only notable discrepancy among all analytes compared among all studies. The current study found Ni concentrations roughly half that reported in previous studies, with the exception of Zubot et al. (2012) (Table 2-3). Some previous studies have analyzed fresh coke sampled directly from the coker (Jack et al. 1979a; Har, 1981; Zubot et al., 2012) whereas Kessler and Hendry (2006) and Chung et al. (1996) examined samples collected from coke deposits. A preliminary assessment of elemental associations in coke was possible by performing Pearson correlations including all samples, to refine potential phases and trace metal hosting within coke.

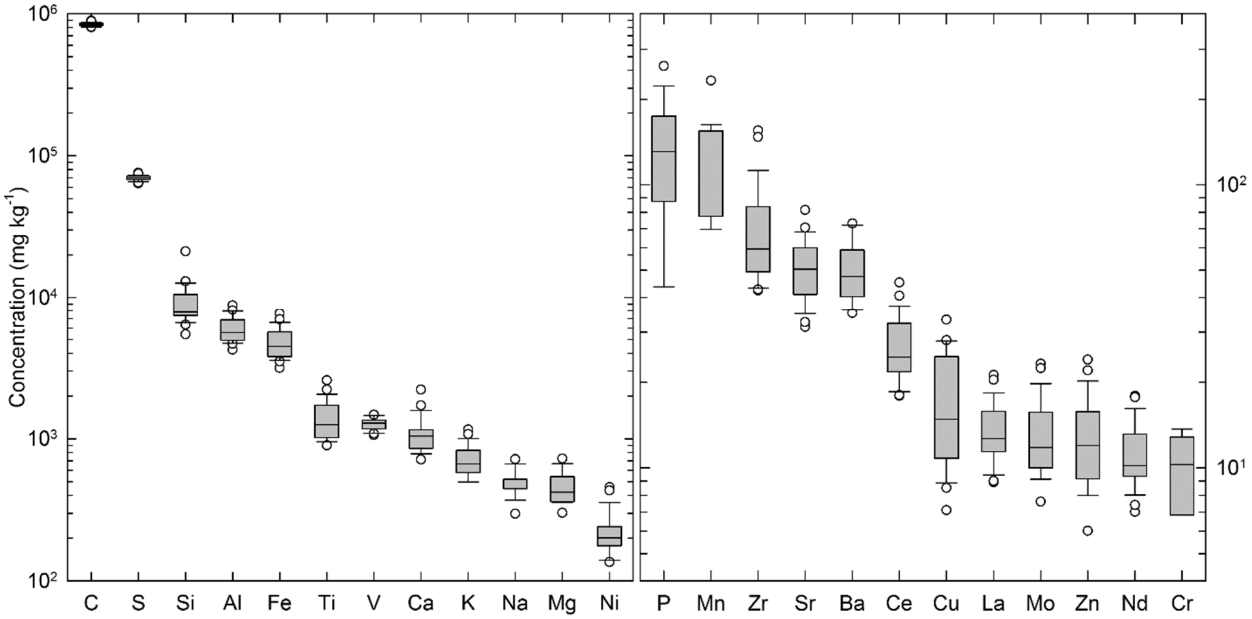

Figure 2-3. Bulk elemental analyses for elements in Syncrude fluid coke from three deposits. Analytes with mean concentrations < 10 mg kg^{-1} are not shown. Box lines define 25th, 50th, and 75th percentiles; lower and upper whiskers define 10th and 90th percentiles; open circles represent outliers.

Table 2-3. Comparison of selected analytes with previous studies of Syncrude fluid coke.

Study	C (wt. %)	S (wt. %)	Fe (mg kg^{-1})	Ti (mg kg^{-1})	V (mg kg^{-1})	Ni (mg kg^{-1})
1	~81.6	~3.3	~2570	~1160	~1590	~660
2	79.0 - 81.5	5.8 - 7.1	4080 - 6150	1288 - 1730	1518 - 1947	548 - 712
3	80.7 - 83.7	6.2 - 6.8	3538 - 6721	1150 - 2367	1599 - 1766	475 - 520
4	78.0 - 84.4	7.0 - 8.1	3022 - 8733	1140 - 3512	1134 - 1540	469 - 588
5	75.3 - 88.9	5.6 - 7.2	4480 - 8390	1560 - 2460	1007 - 1369	35 - 68
6	80.1 - 89.3	6.4 - 7.6	3150 - 7630	900 - 2580	1060 - 1480	136 - 457

1) Jack et al. (1979a), n = 1, singlet; 2) Har (1981), n = 10, duplicate; 3) Chung et al. (1996), n = 5, singlet; 4) Kessler and Hendry (2006), n = 3, triplicate; 5) Zubot et al. (2012), n = 29, singlet; 6) this study, n = 28, singlet, select triplicate

Relationships among all statistics are reported for a sample size n = 28 and a significance level of 5 % (p = 0.05). Carbon and S were strongly correlated (R = 0.96), as was expected. All elements which were negatively correlated with C – Fe, Ti, P, Zr, Ce, Nd, and Y – were also negatively correlated with S at similar R values. Vanadium was not correlated with Ni. At the bulk scale V is correlated with S (R = 0.89) and C (R = 0.83) – and hence the organic phase – rather than the inorganic, Ti (R = -0.71) or Fe (R = -0.45) oxide phases. Nickel correlations were weaker, and less significant than V correlations. This lack of definitive Ni association in coke could be induced by either hosting in multiple different phases or by Ni existing in simple ionic form.

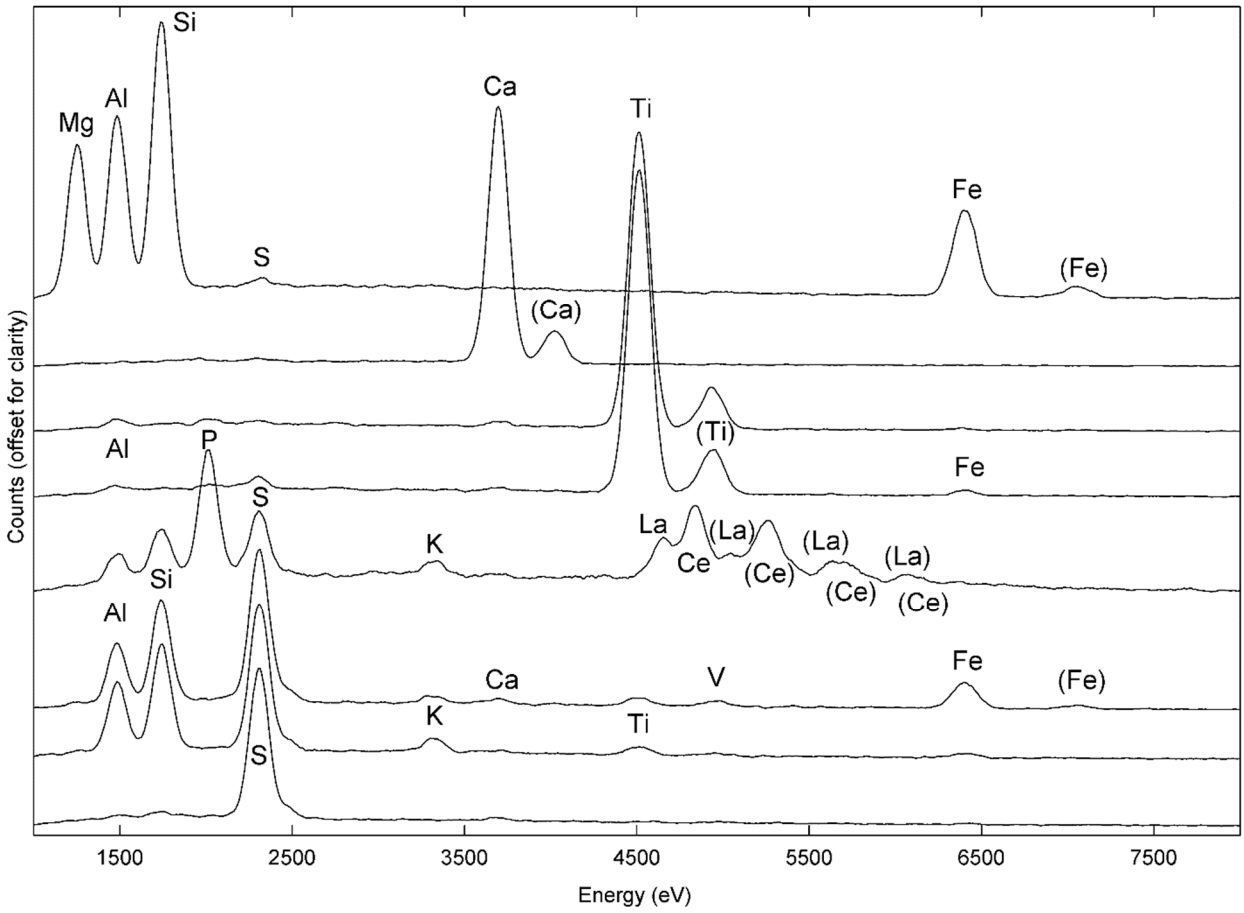

Figure 2-4. Selected EMPA energy dispersive X-ray spectra of coke matrix (bottom spectrum) and selected inorganic inclusions in coke particles.

Iron and Ti showed strong correlations at the bulk scale (R = 0.80), indicating a potential association within oxide phases. While EDX spectra revealed discrete Ti crystals disseminated throughout the coke matrix (Figure 2-4), particular regions within coke grains exhibited a higher concentration of collocated sub-micron sized Fe and Ti particulate. Silicon, Al, K, and Mg, were correlated with one another (R = 0.49-0.67) in bulk chemistry, potentially as a result of their association within aluminosilicate and clay minerals. Bulk elemental correlations among Si and K, Mg, and Al were not as strong as the correlations amongst K, Mg, and Al. The EDX spectra revealed distinct Si crystals disseminated throughout the coke matrix, but particular regions within coke grains exhibited elevated concentrations of collocated sub-micron sized Al, K, Mg, and Si particulate (Figure 2-4). Phosphorus exhibited strong correlations with REEs (La, Ce, Nd, and Y) at the bulk scale. Furthermore, EDX spectra of discrete P crystals disseminated throughout the coke matrix exhibited peaks for Ce and La (Figure 2-4). Elements commonly found in monazite, (Ce, La, Nd, Y) PO_4, were significantly correlated in bulk chemistry with Ti, Fe, Zr, and other

elements. This correlation is likely attributable to association of Fe-Ti particles and monazite particles in the ore feed. Strontium was correlated with Ca (R = 0.50), potentially indicating an association with carbonate minerals.

The elemental composition of coke was generally consistent among and within the three coke deposits (Appendix B). While mean elemental concentrations were similar (within 1 σ) among deposits, some spatial trends were observed. The mean Fe and Ti concentrations in coke samples obtained from CB are higher, by 1.3 and 1.5 times, respectively, compared with the other two deposits. These higher concentrations likely corresponded to coke possessing a larger inorganic fraction. The presence of Fe and Ti is geochemically relevant as coke containing oxide particles may be more capable of acting as adsorption sites for aqueous trace metals (Blackmore et al., 1996; Zubot et al., 2012). The V content was higher in CC5 by ~9 % on average as compared with the other two deposits. Since CC5 represents a historical coke deposition area which has been inactive since 2000, this subtle concentration difference may reflect a slight change in the bitumen feed composition or the coking method. Nickel did not exhibit a similar trend, indicating that the perceived trend in V was either a statistical artifact or that V and Ni were hosted differently. The elements Al, Ca, K, Mg, and Na each have nearly identical concentrations in CB and CC5 samples, but are lower in the samples from CW. However, the CW sample size was small so this apparent trend may not be meaningful.

2.4.3 Mineralogical Characteristics

X-ray diffraction patterns for all samples were dominated by the aromatic, asphaltenic molecules that comprise the majority of the coke matrix (Figure 2-5). Both the inorganic, crystalline mineralogical phases and the organic, amorphous and aromatic asphaltenic carbon matrix were investigated. Synchrotron PXRD revealed more information about both the structure of the carbonaceous component in coke and the crystalline phases hosted therein. The aromatic background lineshape was more clearly resolved in the synchrotron PXRD patterns than in the Cu Kα source patterns; most notably in the unresolved shoulder at low 2θ angles and in the missing broad low-magnitude feature at high 2θ. Synchrotron PXRD also facilitated the detection of several crystalline phases within the asphaltenic matrix that were not discernible using a conventional Cu Kα source XRD due to poor 2θ resolution. While XRD is well suited to, and more commonly used in, the identification of crystalline phases, the technique also provided detailed structural information about the volumetrically-larger non-crystalline component.

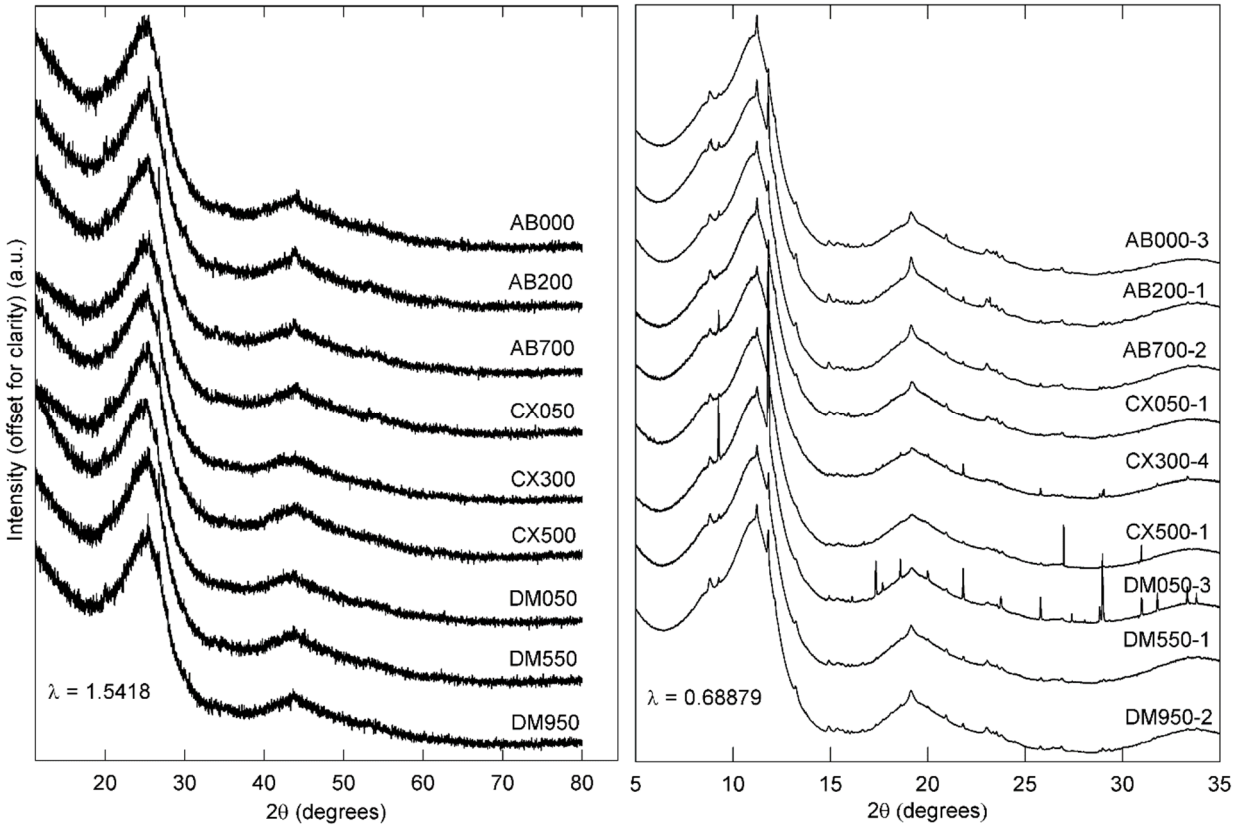

Figure 2-5. Conventional Cu Kα source X-ray diffraction patterns (a) and synchrotron powder X-ray diffraction patterns (b) for bulk coke samples. Sites AB, CX, and DM are from CB, CW, and CC5 coke deposits respectively. Abscissae scaled to show equivalent 2θ ranges.

2.4.3.1 Inorganic components

The crystalline fraction contains aromatic crystallite carbon, SiO_2, TiO_2, a hydrated Ni sulfate (Angel and Finger, 1988), and an organically-complexed V phase (Miyoshi et al., 2012), Muscovite or a similar phyllosilicate phase was detected in some samples. These were the only phases with figure-of-merit (FOM) values >0.8 (Appendix D) that were possible given the bulk coke chemical composition. Small differences were observed in the relative magnitudes of crystalline phase diffraction lines/peaks, though only for samples collected from different deposits. Diffraction patterns for samples from the CW deposit (Site CX) had consistently higher FOM values for the Ni sulfate and the organically-complexed V phase than any of the other patterns. Diffraction patterns for samples from the CB deposit (Site AB) all had considerably lower FOM values for the muscovite-like phase than any of the other patterns. Finally, diffraction patterns for samples from the CC5 deposit (Site DM) had the lowest FOM values for TiO_2, which supported the deposit-scale trends observed in Ti bulk chemistry, though the relationship may not be

significant. Meaningful quantitative phase identification (Rietveld refinement or similar) of these secondary crystalline minerals was not possible given the considerable organic carbon diffraction signal of coke. The large amount of background subtraction preprocessing necessary to remove this signal would render the magnitudes of crystalline-phase peaks unreliable.

The ash (non-carbonaceous) content of fluid coke is typically 4 – 7 %, due to clay particles trapped in the bitumen feedstock (Jack et al., 1979a; Chung et al., 1996). Har (1981) found the ash content of Syncrude fluid coke to be variable but slightly higher at 7 – 8.5 % for all particle sizes. Ash associated with fluid coke is formed when coke is combusted in the coke furnace, and different ashing temperatures influence the suite of minerals present (Jang and Etsell, 2006). Low-temperature ashing (LTA) induces minimal mineral phase transformation as compared to the coking process itself; Syncrude fluid coke ashed using LTA has previously been analyzed via XRD. Results suggest that the quartz, kaolinite, illite, feldspars, anhydrite, and hematite are the dominant crystalline phases (Jang and Etsell, 2006).

Coke particles uptake and include various mineral phases owing to the heterogeneous composition of the bitumen feed. While EMPA EDX spot analyses of discrete (sub) micron-scale crystals within coke particles provided only qualitative elemental information, this technique confirmed the presence of Ti- and Fe-bearing crystals and alkali-aluminosilicate clay particles disseminated throughout most coke particles. Distinct crystals of quartz, calcite, dolomite, and Fe-sulfide particles were detected within some coke particles. Monazite (La, Ce) crystals were observed, though less frequently. All of these EDX findings are in agreement with bulk elemental analyses and correlations.

Since all observed minerals were found included within coke particles – occasionally forming the particle core – they were most likely derived from the ore rather than being formed during coking or introduced post-deposition. This interpretation is consistent with previous observations which showed that Ti- (and Zr-) bearing minerals present in oil sands ore are concentrated in the froth during bitumen recovery (Kaminsky, et al., 2008). These and other minerals – including Ti oxides, Fe sulfides, Fe carbonates, Fe-Ti oxides, and REE oxides – were often found intergrown with silicate minerals in samples of the oil sands ore feedstock (Kaminsky et al., 2008).

2.4.3.2 Organic components

Diffraction patterns for samples from all deposits and depths were similar with respect to the carbonaceous matrix. The diffraction patterns obtained for coke appear very similar to those reported for coal by Lu et al. (2001) suggesting that the structural forms of carbon are comparable between these two materials. Coal contains short-range, localized, crystalline, graphitic structures, but also contains a large proportion of disorganized, amorphous carbon (Lu et al., 2001). This variety gives rise to three main amorphous carbon diffraction bands, matching those observed for coke samples (Figure 2-5b). These bands loosely approximated the locations of equivalent reflections in pure, crystalline graphite, but were far broader due to the amorphous content. The bands were located at ~11.04°, ~19.34°, and ~34.06° in units of 2θ, or 0.140, 0.244, and 0.425 in units of [sinθ / λ]. The first corresponds to the (002) band which arises from the interlayer spacing (Lu, et al., 2001). The last two correspond to the (10) and (11) bands which arise from the hexagonal aromatic ring structure (Yen et al., 1961; Lu et al., 2001). The mean layer distance "d_m" between aromatic sheets was determined using the position of the (002) band:

$$d_m = \frac{\lambda}{2\sin\theta} = \frac{0.68879\ \text{Å}}{2\sin\left(\frac{11.04°}{2}\right)} = 3.58\ \text{Å} \qquad \text{Equation 2-1.}$$

The interlayer distance between successive aromatic sheets is a function of sheet flatness, the presence of sheet imperfections, and the inclusion of heteroatoms like S or metals in the asphaltenic micelles. Pure graphite, which is composed of flat aromatic sheets free from inclusions or imperfections by comparison, has an interlayer distance of 3.34 Å (Yen et al., 1961). An early study on coke made from electrode pitch binder found the material to have interlayer spacing of 3.47-3.52 Å, but mentioned that clusters composed of fewer aromatic sheets can display larger interlayer spacing (Pollack and Alexander, 1960). The value of 3.58 Å obtained for the coke in this study is larger, as bitumen-derived coke may contain more impurities, and thus more asphaltenic sheet imperfections, than electrode binder pitch cokes.

The small asymmetric shoulder on the left side of the (002) band is the γ band (Fig. 2-5). It is found at ~8.93° 2θ or 0.113 [sinθ / λ]. This band arises from the presence of saturated aliphatic side chains attached to the edges of aromatic carbon crystallites (Lu et al., 2001). The distance between saturated portions of the molecules ("d_γ") was calculated with a modified version of Equation 2-1, but using the γ band position:

$$d_\gamma = \frac{5\lambda}{8\sin\theta} = \frac{5(0.68879\ \text{Å})}{8\sin\left(\frac{8.93°}{2}\right)} = 5.53\ \text{Å} \qquad \text{Equation 2-2.}$$

This mean distance of 5.53 Å is slightly smaller than the distances reported by Yen et al. (1961) for asphaltenes in bitumen (5.6 – 6.0 Å). Asphaltene micelle breakage, subsequent hydrogenation, saturation, and addition of more aliphatic side chains during coking could explain the decrease in mean distance between saturated side chains.

2.4.4 Bulk XANES Analyses

2.4.4.1 Vanadium and nickel

Bulk V K-edge XANES spectra for all samples exhibited similar lineshapes, characterized by a flattened, tilted, asymmetric white-line (centred at ~5491 eV) and a pre-edge peak roughly 0.45 the height of the absorption edge (5469 eV). These features are broadly consistent with V organically-complexed in the +4 oxidation state (Figure 2-6a). While vanadyl porphyrin complexes are the predominant form of V in heavy oil and bituminous deposits (Lewan and Maynard, 1982), there were several differences between bulk coke and vanadyl porphyrin reference spectra. Differences included pre-edge peak splitting, pre-edge peak magnitude decrease, and near-edge flattening. Model porphyrin standards were insufficient to completely describe bulk V K-edge spectra. Finite difference modelling of the near-edge structure (FDMNES) (Bunau and Joly, 2009) of model porphyrins (Molinaro and Ibers, 1976) revealed that the V pre-edge feature shape and magnitude were sensitive to changes in first-shell interatomic distances of only ±0.02 Å. The subtle pre-edge peak-splitting observed in V bulk coke spectra could be in part explained by either a slight decrease in V=O bond distance or a slight increase in V-N distance, though predicted magnitudes and energies were not accurate (Appendix E). However, neither of these distortion mechanisms flattened the near-edge region to the extent seen in bulk coke spectra.

Vanadium XANES spectra of raw, pre-coking asphaltene collected by Lytle (1983) (Figure 2-6a) shows considerable broadening of most near-edge features compared with pure porphyrins. The high-temperature, oxidizing conditions during fluid coking (Asaoka et al., 1983) may promote some replacement of N atoms by O atoms around the porphyrinic metal centre in asphaltene micelles. Square-pyramidal O coordination, as in vanadyl bis-phenyl butane dionate (VOPBD) (Hon et al., 1965), was therefore also considered. A V K-edge XANES spectrum for VOPBD from Wong et al. (1984) was used as a proxy for this coordination type in LCF (Figure 2-6a). Conversion of porphyrinic V to octahedrally-coordinated V was previously noted by Miller and Fisher (1999) in association with thermal treatment of asphaltenes (hydrocracking). Vanadium (III) octahedrally coordinated by O atoms displays a small pre-edge peak shifted to slightly higher energy as

compared with the porphyrinic pre-edge peak (Maylotte et al., 1981; Wong et al., 1984). A XANES spectrum for V(III) substituted into distorted octahedral sites in the phyllosilicate mineral roscoelite ($KAlV_2Si_3O_{10}(OH)_2$) (Maylotte et al., 1981; Wong et al., 1984) displayed two distinct, asymmetrical peaks at ~5486 and ~5499 eV, straddling the energy of the single rounded porphyrin peak at ~5490 eV. Octahedral coordination of V(III) with O can also occur in V_2O_3 and as V substituted in some spinels or ferro-titanian oxide minerals (Balan et al., 2006). However, the near-edge doublet peak feature in these compounds was not consistent with bulk spectra and provided poor fitting results (Appendix F).

Combining spectra for the square-pyramidal V(IV)-N, V(IV)-O, and octahedral V(III)-O coordination types flattened the XANES lineshape and better explained the pre-edge peak magnitude decrease and splitting in coke spectra (Figure 2-6a). Fitting of bulk coke suggested that square-pyramidal N and O coordination dominated and distorted octahedral V(III)-O coordination was a minor component. Including VOPBD-like coordination in fits was highly favourable as it halved the R-factor and considerably minimized fitting residuals.

Bulk Ni K-edge XANES spectra for bulk coke were characterized by four main features (Figure 2-6b). A small pre-edge feature at 8334 eV and shoulder at 8340 eV were generally consistent among all samples. Similar to V, porphyrins are also an important host for Ni in petroleum systems (Lewan and Maynard, 1982; Lewan, 1984). Two peaks at ~8352 eV and ~8359 eV that formed a doublet feature on the principal edge were generally consistent with Ni porphyrins such as Ni octaethyl porphyrin (NiOEP) and Ni tetraphenyl porphyrin (NiTPP). However, these peaks fluctuated in relative magnitude among bulk samples, indicating slight variations in the Ni coordination environment. The NiOEP standard was a superior fit for most samples' spectra (Table 2-4b). Though, like V, Ni porphyrin standards were insufficient to fully explain the shape of the Ni K-edge XANES, especially the increased magnitude of the ~8352 eV feature.

Spectra obtained for asphaltene samples (Lytle, 1983) appeared to be intermediary between bulk Ni K-edge XANES for coke and NiOEP reference spectra (Figure 2-6b). The sharp shoulder feature at ~8340 eV was found to shift to slightly higher energy from porphyrin to asphaltene to coke. The shoulder at ~8340 eV and the spectral lineshape after 8370 eV are consistent between the porphyrin standard and the asphaltene sample, but both regions become broadened and smoothed in coke spectra. The two peaks at ~8352 eV and ~8359 eV show a greater magnitude

disparity in the Ni XANES spectra for the porphyrin standard, but more similar magnitudes in both the coke and asphaltene spectra. These spectral relationships support the conclusion that organo-metallic Ni sites show increasing distortion and variability as porphyrins are incorporated into asphaltenes, and then subsequently as asphaltenes undergo coking. Finite difference modelling of the near-edge structure (FDMNES) for the NiOEP and NiTPP compounds could not fully describe the experimental Ni K-edge XANES for these porphyrin standards. However, modelling showed that slightly inflated interatomic distances between Ni and the surrounding N and C atoms increased the relative magnitude of the lower energy peak in the porphyrin spectra (Appendix G). Subtle variations in asphaltene metal site chemistry could therefore be partially responsible for fluctuations in the Ni K-edge XANES spectra for bulk coke samples (Figure 2-6b).

Inorganic Ni compounds examined – NiO, $NiSO_4 \bullet 6H_2O$, $Ni(OH)_2$, $NiCO_3 \bullet 2Ni(OH)_2$ – had a prominent, narrow white-line feature centred around 8349 - 8352 eV. An increase in magnitude of the ~8352 eV feature relative to the ~8359 eV feature could therefore be attributed to the presence of inorganic Ni compounds. Statistically strong fits (R-factor < 0.0060) of Ni K-edge XANES for bulk coke were achieved using NiOEP, NiTPP, and NiO standards. This inorganic phase is consistent with Ni octahedral oxygen coordination, similar to V bulk coke XANES results and with what was proposed by Miller and Fisher (1999). However, XRD phase identification consistently suggested Ni sulfate was also present in coke (Figure 2-5b). Furthermore, a portion of Ni in flexicoker coke was present in a simple ionic form, at a 1:1 ratio molar ratio with sulfate (Jack et al., 1979). Fitting of Ni K-edge XANES for bulk coke with NiOEP, NiTPP, and $NiSO_4 \bullet 6H_2O$ standard spectra yielded weaker fits, both statistically and visually (R-factor ≈ 0.011).

Table 2-4a. Linear combination fitting (LCF) results for V fits shown in Figure 2-6.

Sample	VOOEP	VOTPP	VOPBD	roscoelite	Sum	R-factor
AB000	20 ± 2 %	35 ± 2 %	46 ± 2 %	1 ± 1 %	102 %	0.0017
AB200	20 ± 2 %	33 ± 2 %	44 ± 2 %	4 ± 1 %	102 %	0.0015
AB700	29 ± 2 %	25 ± 2 %	40 ± 2 %	8 ± 1 %	103 %	0.0014
CX050	18 ± 2 %	37 ± 2 %	46 ± 2 %	1 ± 1 %	102 %	0.0016
CX300	12 ± 2 %	40 ± 2 %	50 ± 2 %	0 %	101 %	0.0019
CX500	23 ± 2 %	30 ± 2 %	43 ± 2 %	6 ± 1 %	102 %	0.0015
DM050	15 ± 2 %	38 ± 2 %	47 ± 2 %	1 ± 1 %	102 %	0.0017
DM550	25 ± 2 %	28 ± 2 %	40 ± 2 %	9 ± 1 %	102 %	0.0014
DM950	26 ± 2 %	29 ± 2 %	40 ± 2 %	8 ± 1 %	102 %	0.0013

Table 2-4b. Linear combination fitting (LCF) results for Ni fits shown in Figure 2-6.

Sample	NiOEP	NiTPP	NiO	Sum	R-factor
AB000	40 ± 2 %	44 ± 3 %	12 ± 1 %	96 %	0.0037
AB200	50 ± 2 %	42 ± 3 %	6 ± 1 %	97 %	0.0043
AB700	31 ± 3 %	61 ± 4 %	5 ± 1 %	97 %	0.0058
CX050	58 ± 2 %	32 ± 3 %	8 ± 1 %	97 %	0.0035
CX300	61 ± 2 %	28 ± 3 %	10 ± 1 %	98 %	0.0033
CX500	51 ± 3 %	44 ± 3 %	2 ± 1 %	97 %	0.0052
DM050	56 ± 2 %	33 ± 3 %	9 ± 1 %	97 %	0.0034
DM550	49 ± 3 %	44 ± 3 %	3 ± 1 %	95 %	0.0056
DM950	47 ± 3 %	45 ± 3 %	4 ± 1 %	97 %	0.0051

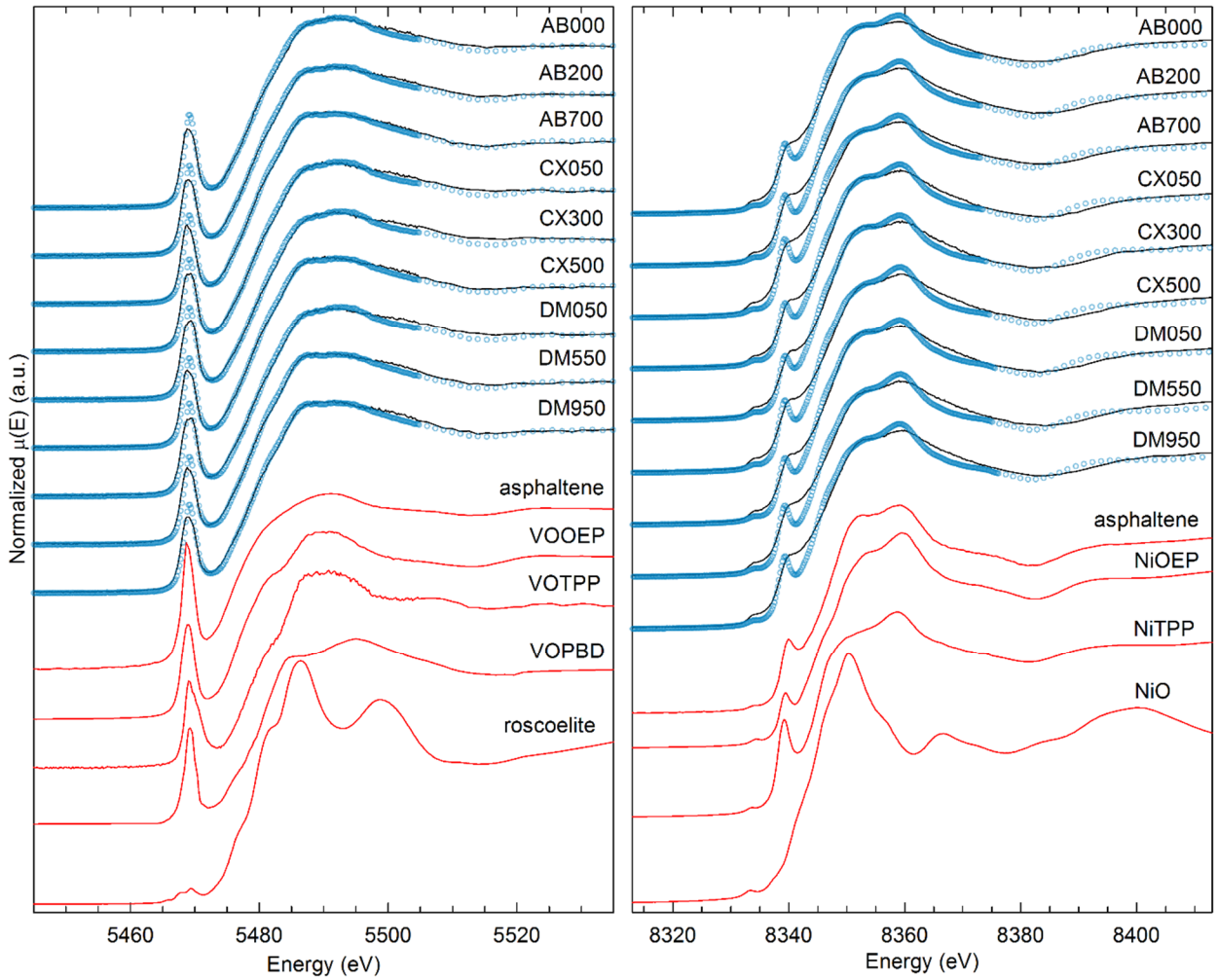

Figure 2-6. Comparison of V (a) and Ni (b) K-edge XANES spectra for bulk coke, with spectra for asphaltene (Lytle, 1983), porphyrin-like square-pyramidal coordination standards (VOOEP, VOTPP, VOPBD, NiOEP, NiTPP), and inorganic octahedral coordination standards (roscoelite, NiO). Fits shown with open circles.

2.4.4.2 Sulfur and iron

Sulfur K-edge XANES spectra for all samples revealed a prominent white-line peak at 2473.8 eV, a smaller secondary feature at 2475.8 eV, and a broad plateau from 2480-2483 eV (Figure 2-7a). These peaks correspond well with values for thiophenic sulfur (Zeng et al., 2013). Discrepancies were apparent in the S K-edge XANES spectra lineshape compared to the dibenzothiophene standard at energies greater than 2478 eV. Features at 2473.8 and 2475.8 eV in coke sample spectra were also dampened and broadened compared to the dibenzothiophene standard spectra. Linear combination fitting using a variety of organic and inorganic sulfur standard spectra confirmed that thiophenic coordination was the best fit. Sulfur K-edge XANES spectra are generally consistent with asphaltene S K-edge spectra reported by George and Gorbaty (1989) and Pomerantz et al. (2014), reflecting the large asphaltenic content of coke. George and Gorbaty (1989) concluded that S in asphaltenes is almost entirely thiophenic. Bejarano et al. (2003) came to a similar conclusion with X-ray photoelectron spectroscopic (XPS) analysis of Syncrude fluid coke. While the local atomic interaction between S sites and the surrounding aromatic cycles are distinctly thiophenic, longer-range interactions into the asphaltene micelle structure do not possess the same pure thiophenic character seem in standard compounds.

Iron K-edge XANES spectra exhibited greater variability among samples compared to other elements (Figure 2-7b). The spectra were characterized by two main features: a broad low-magnitude pre-edge feature centred at 7113.5 eV and a rounded white-line feature centred at 7132 eV. A variable double-shoulder feature was found between these two energies. These spectra could not be fit using a single reference standard. Distinct Fe-S grains were observed in coke particles using EMPA. Sulfur K-edge XANES did not exhibit features characteristic of sulfide minerals, which represent a minor fraction of the total S in coke. Both bulk-scale chemistry and micro-spatial spectroscopic relationships were observed between Fe and Ti, suggesting the presence of an ilmenite-like phase. In addition to pyrite, ilmentite, and magnetite, akaganeite, lepidocrocite, goethite, hematite, Fe(III) sulfate, jarosite, siderite, and ferrosmectite spectra were also included in the fitting process. Combinatorial LCF of the near-edge spectra was performed, first by assessing all unique combinations of two of the eleven Fe standards (C = 55), for each of the nine spectra. While the best of these combinations of two standards provided statistically acceptable fits (R-factor < 0.010), the residuals between fit and experimental spectra were large. Fitting was also performed using all unique combinations of three of the eleven Fe standards (C =

165). The best of these fits were superior both statistically (R-factor < 0.005) and with respect to fitting residuals. The best fits for all spectra included pyrite (25-35 %), magnetite or ilmenite (40-60 %), with the balance comprising one of akaganeite, lepidocrocite, or Fe(III) sulfate (15-25 %).

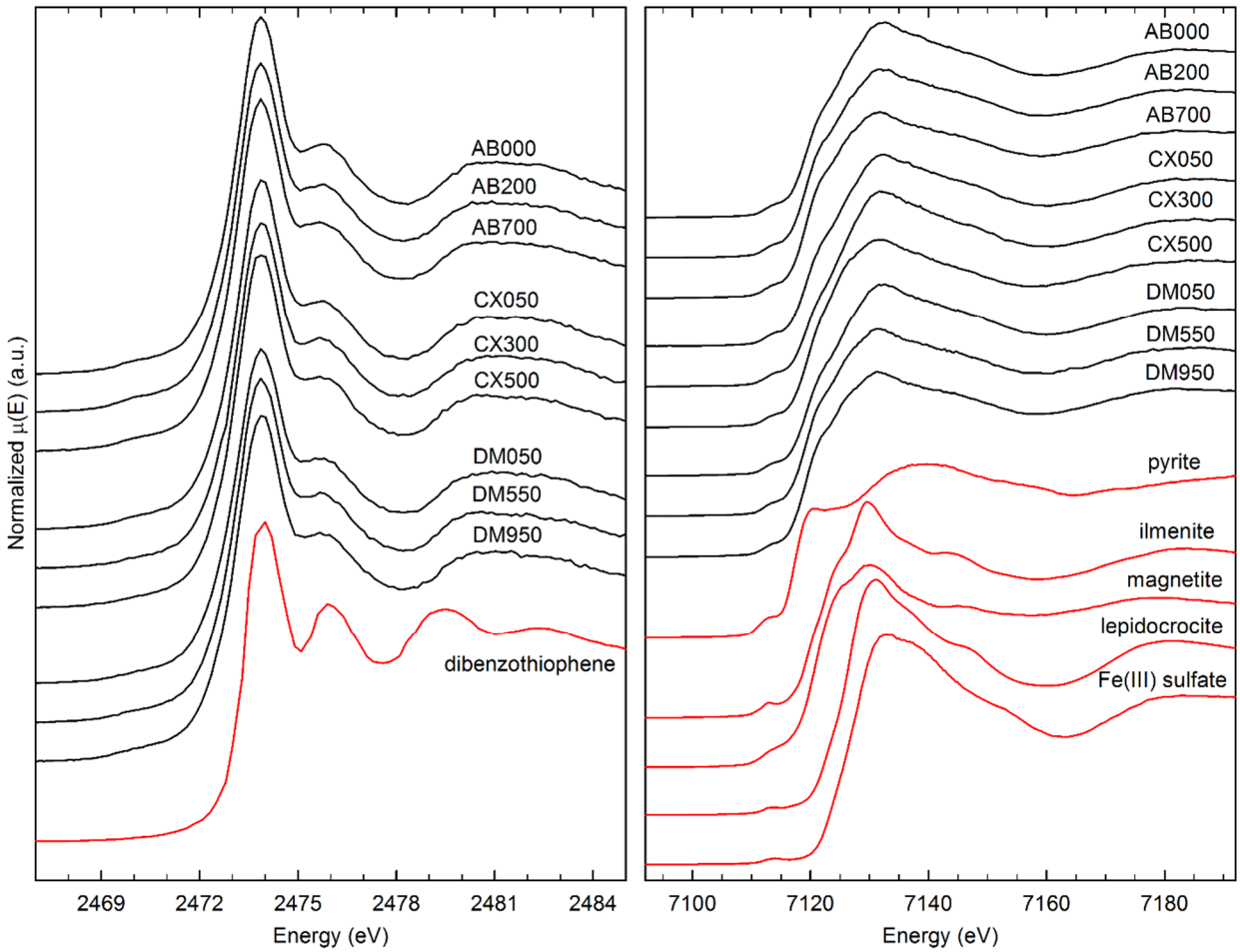

Figure 2-7. Comparison of bulk coke S (a) and Fe (b) XANES spectra with spectra for thiophene (Bohic et al., 2008), pyrite, ilmenite, magnetite, lepidocrocite, and iron(III) sulfate.

2.5 Conclusions

The current study examined the linkage between the geochemical characteristics and the bulk form of trace elements in fluid petroleum coke. Relationships between changes in chemistry and metal speciation were observed in bulk elemental and mineralogical analyses, though these fluctuations were generally small. Coke contains a variety of mineral phases as inclusions and as disseminated micron-scale particles. Coke mineralogy, bulk elemental composition, and bulk speciation of trace metals fluctuated only slightly among depths, deposits of different ages, and storage conditions. Weathering had a limited impact on bulk coke chemistry.

Linear combination fitting of bulk V K-edge XANES suggests that V is hosted in a number of different atomic coordination environments. Square-pyramidal VO^{2+} N coordination (porphyrinic), square-pyramidal VO^{2+} O coordination (dionatic/altered porphyrinic), and distorted octahedral V(III) O coordination (phyllosilicate substitution) appear to be the predominant forms. Bulk Ni chemistry is generally consistent with porphyrinic speciation, with deviations resulting either from asphaltenic metal site structural heterogeneity or inorganic coordination as an oxide or similar octahedrally-coordinated phase. This research showed that V and Ni are not exclusively hosted in stable porphyrinic coordination in coke. The dominant form of S is thiophenic coordination. Iron appears to be hosted in a combination of pyrite and ilmenite-like phases, with a tertiary component comprised of oxyhydroxides or sulfates.

Studying bulk coke geochemistry confirmed that coke deposits are a large reservoir for V, Ni, and other trace elements. The bulk-scale chemical information gleaned from this research provided the basis for further exploration of micro-scale trace element comportment in fluid petroleum coke particles and mobility of these elements within coke deposits.

CHAPTER 3 VANADIUM AND NICKEL GEOCHEMISTRY IN OIL SANDS FLUID PETROLEUM COKE DEPOSITS

3.1 Introduction

Petroleum coke is generated in large quantities during upgrading of oil sands bitumen to synthetic crude oil. Vanadium and Ni have been identified as toxic components of coke leachates (Fedorak and Coy, 2006; Puttaswamy and Liber, 2011). Baker et al. (2012) found through *in situ* microcosm experiments that amending (capping) other sediments with coke in a constructed wetland was associated with increased uptake of V and Ni by a macrophytic green alga and benthic invertebrates. A potential mechanism of V toxicity has been found to arise from the structural similarities of vanadate and phosphate ions, allowing vanadate to bind to phosphate sites on (Na^+,K^+)-ATPase or other enzymes, inhibiting proper functions (VanEtten et al., 1974; Cantley et al., 1977). Coke is a predominantly carbonaceous material, but it contains elevated sulfur and trace element concentrations, rendering it unsuitable for use in most industrial applications. Oil sands coke cannot be safely used as a combustion source nor can it be readily used for electrode manufacture (AER, 2015). It has generally been stockpiled in subaerial deposits near upgrading facilities, thus wind-blown coke dust can lead to widespread contamination (Zhang et al., 2016). As coke deposits increase in size, the use of coke as a material for constructing reclamation landscapes (AER, 2015) or for treating oil sands process-affected water (OSPW) (Zubot et al., 2012) is becoming increasingly favoured. While the geotechnical and physical properties of petroleum coke may make it amenable to such usage, its geochemical behaviour remains poorly understood.

Coke is generated via delayed coking, fluid coking, or flexicoking. Delayed coke is formed, and accumulates during a ~24-hour cycle, in a single coking vessel, after which the coke is extracted and the next cycle begun. Fluid coke is generated via continuous circulation between a coke burner unit and a fluidized bed reactor (coker) (Blaser, 1992; Anthony, 1995). Hot bitumen is sprayed into the coker, where it coats the surfaces of existing coke grains. Short-chain hydrocarbons ranging from naphtha to heavy gas oil are cracked off the complex long-chain hydrocarbon molecules; onion-skin layers of trace metal-rich asphaltenic material are left on coke

grain surfaces with each successive coking cycle (Dunlop et al., 1958; Blaser, 1992; Matsen, 1996). Flexicoking, is similar to fluid coking but adds a gasification step to reduce the C, S, and volatile content (Furimsky, 1998). Differences in temperature and coke particle formation lead to variation in the physical and chemical properties of coke derived from the various processes. Fluid coke was the focus of the current study. Vanadium and Ni are present primarily as organic complexes in petroleum deposits, specifically in metalloporphyrins and in other porphyrinic-like atomic coordination environments within asphaltenic micelles (Reynolds et al., 1987; Filby and Strong, 1991).

Vanadium mobility within coke deposits is likely dependent on solid phase comportment, oxidation state and thus availability of oxygen, pore water or process water chemistry, and pH conditions (Wehrli and Stumm, 1989). Zubot (2010) reported that V mobility was enhanced under oxic, alkaline pH conditions. Vanadium can exist in six possible oxidation states, but +3, +4, and +5 dominate under most natural conditions (Baes and Mesmer, 1976). Oxidized V(V) species are more prevalent than V(IV) species in the supernatant of OSPW-coke mixtures, under oxidizing conditions and neutral-alkaline pH (Jensen-Fontaine, 2012). Modelling and field data suggested that temperature and pressure gradients can induce convective air flow through the highly air-permeable unsaturated zone in coke stockpiles (Lahmira et al., 2013). Therefore, considerable oxygen ingress is expected to promote oxidizing conditions in the unsaturated zone and the upper portion of the saturated zone. Nickel is considerably less redox-sensitive than V, with only one common oxidation state in natural settings, Ni(II). The mobilization of Ni from coke is dependent on pH conditions and solid phase speciation. For example, Zajic et al. (1977) noted that slight increases in pH caused decreases in Ni concentration in coke pore water. In leaching experiments on flexicoker coke a portion of the Ni content was readily leached using only water (Jack et al., 1979). Sequential extractions experiments have demonstrated that most metals are either flushed with water (water soluble fraction) or remain firmly bound to the coke matrix (residual fraction); coke deposit pore water trace metal concentrations are attributable to the water soluble phases (Kessler and Hendry, 2006).

The current research examined controls on V and Ni mobility in oil sands fluid coke deposits. The research focused on both redox and pH controls, integrating aqueous and solid-phase analyses to assess speciation of V and Ni in fluid to coke and develop a better understanding of how these elements are hosted after undergoing coking. Understanding the *in situ* fate of the trace

elements of concern as coke and OSPW interact was of primary importance to the current study. In order to expand upon the various laboratory experiments which have studied the interaction of coke and OSPW, a field-based geochemical approach was taken in this study.

3.2 Study Site

Three fluid coke deposits were investigated at the Syncrude Mildred Lake oil sands mine located 40 km north of Fort McMurray, Alberta. These deposits exhibited varied environmental conditions, including hydrological and redox conditions, and presence of a vegetated soil cover. The principal focus was on Coke Beach (CB), an active deposit 1.5 km^2 in size containing 31 million m^3 of uncovered coke (Figure 3-1). Coke Beach was consequently ideal for studying the direct interaction of precipitation infiltration and oxygen ingress on coke deposit water chemistry. The other two coke deposits, Coke Watershed (CW) and Coke Cell 5 (CC5), are smaller, inactive, and have been capped with reclamation soil and vegetated.

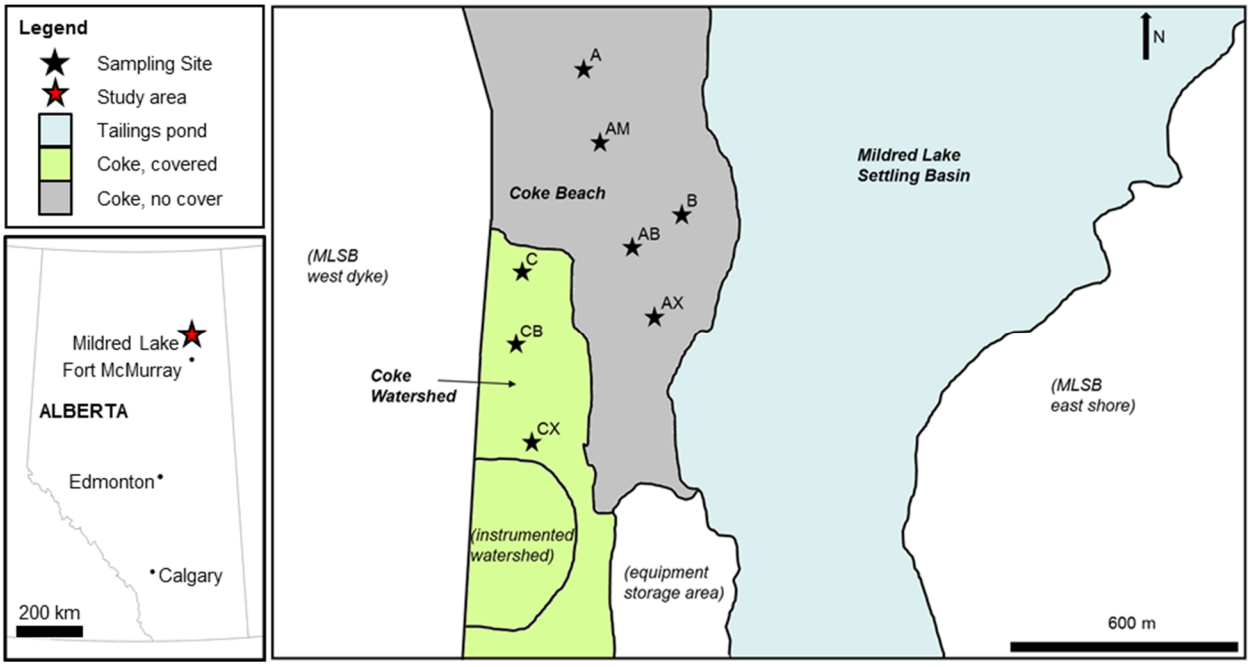

Figure 3-1. Maps showing location of study area and locations of multi-level well water sampling locations and Coke Beach (CB) and Coke Watershed (CW).

The portions of CW for which core were collected contained interbedded layers of coke, sand fill, oil sands mature fine tailings and residual bitumen. The entire sampled depth of the CC5 deposit was homogenously comprised of coke. Water sampling locations were selected throughout CB to capture the spatial variability in water chemistry both along the length of deposit (Sites A, AM, and AB) and with proximity to the adjacent Mildred Lake Settling Basin (MLSB) (Sites AX

and B). Locations in the CW deposit were chosen to best observe the relationships of coke, pore water, and the other fill materials.

3.3 Materials & Methods

3.3.1 Well Installations

Multi-level sampling wells were installed at regular depth intervals at sampling locations at CB (n = 5) in July 2014 and CW (n = 3) in August 2014. These wells were constructed by bundling between eight and ten ¼" polyethylene (PE) tubes of varying lengths to a central ¾" cross-linked polyethylene (PEX) tube. Wells were installed to a maximum depth of 8 m because the water level was located 0.5-5.0 m below surface for all locations with a distinct geochemical transition zone 1-3 m below the water table. Wells were positioned at ~0.25 or ~0.5 m spacing in the first metre below the water table and ~1 m spacing below that. The PE tubing was notched and screened over a 10 cm interval with 125 µm Nitex mesh. The multi-level wells were installed by pushing the desired depth of 3" drill stem with a knock-off tip at the base, using a Fraste ML sonic drill rig. The well assembly was lowered down the casing to the base of the hole. The casing and assembly were filled with water to minimize buoyancy.

3.3.2 Water Sampling and Analyses

Water samples were collected from the 8 multi-level wells comprising 67 sampling locations (Figure 3-1). Sampling at CB was conducted in August 2014 and at CW in September 2014 to allow the pore water around the well to equilibrate in the near-hole environment. The water table was measured in the central well with a manual water level meter. Three well volumes were purged prior to sampling to ensure representative pore water samples were obtained. Clean ¼" silicone tubing (Masterflex) was used for each sampling location; it was connected to ¼" PE tubing and routed through the peristaltic pump head.

Measurements of pH, reduction-oxidation potential (Eh), electrical conductivity (EC) and temperature were performed using an inline flow-through cell. Calibration of the pH electrode (Orion 8156BNUWP ROSS Ultra) was checked before each measurement and recalibrated if necessary using a 3-point calibration with NIST-traceable pH 7, 4 and 10 buffer solutions (Thermo Scientific). The performance of the Eh electrode (Orion 9678BNWP Sureflow) was checked before each measurement using ZoBell's (ZoBell, 1946; Nordstrom, 1977) and Light's (Light, 1972) solutions (RICCA Chemical). A standard 1413 µS cm^{-1} electrolyte solution (Thermo Scientific) was used to check the calibration of the conductivity cell between measurements.

Alkalinity was determined immediately after collection on water samples filtered to 0.45 μm by titrating with normalized H_2SO_4 to the bromocresol green methyl red endpoint. A Hach DR2800 spectrophotometer was used to determine ammonia (NH_3) concentrations using the salicylate method (HACH Method 10031) and sulfide (H_2S) concentrations using the methylene blue method (HACH Method 8131).

Samples for quantification of inorganic anions and stable isotopes of water were passed through 0.45 μm membranes and stored in HDPE bottles. Inorganic anion (Br, Cl, F, NO_3, NO_2, PO_4, SO_4) concentrations were determined by ion chromatography (IC), while stable isotopes of water were analyzed with a Picarro cavity ring-down spectroscopy L2120-i water vapour analyzer (Wassenaar et al., 2008). Samples for trace element and major cation analysis were passed through a 0.1 μm membrane, acidified to < pH 2 using concentrated trace metals grade nitric acid (Omnitrace, EMD Millipore), and stored in HDPE bottles. Trace elements were quantified using inductively-coupled plasma mass spectrometry (ICP-MS), whereas major cation concentrations were determined by inductively-coupled plasma optical emission spectrometry (ICP-OES). Water samples were stored on ice in the dark immediately after collection. Thermodynamic modelling of groundwater geochemistry was performed using PHREEQCi (Version 3.1.5) (Parkhurst and Appelo, 1999) with the MINTEQA2 V4 database.

3.3.3 Core Sampling and Analyses

Continuous core samples were collected at CB (n = 6), CW (n = 3), and CC5 (n = 3). Cores from CB and CW were situated within 1 m of multi-level wells to facilitate comparison of solid- and aqueous-phase chemistry. Core samples were obtained in 0.5-m intervals to a total depth of between 6 and 8 m. Thin sections of selected coke samples were made to perform electron microprobe analyses and micro-focused synchrotron X-ray absorption spectroscopic studies. Samples (n = 12) were selected for thin section preparation, from CB (n = 6), CW (n = 3), and CC5 (n = 3). Freeze-dried samples were vacuum-embedded in Epotek 301 and mounted onto 27x47 mm quartz-glass slides using cyanoacrylate adhesive, which exhibits low trace element concentrations. These sections were then ground to a thickness of 30 μm and polished using 0.5 μm diamond with synthetic kerosene. Precautions were taken to avoid dissolution of water-soluble phases.

3.3.4 Electron Micro-Analyses

Electron microprobe analyses (EMPA) and transmission electron microscopy (TEM) were used to collect energy-dispersive X-ray (EDX) spectra at points throughout coke particles. These techniques helped in establishing spatial elemental correlations and were used to explore the micro-scale influence of physical morphology on micro-mineralogy and chemistry. A JEOL JXA-8600 Superprobe EMP with 10 μm resolution was used to examine thin sections with an accelerating voltage of 15 kV. A Hitachi 7700 TEM with sub-micron resolution was used to examine 300 nm sections through single coke particles mounted on a copper 200-mesh grid with an accelerating voltage of 100 kV.

3.3.5 Synchrotron-Based Micro-Analyses

Vanadium and Ni μXRF mapping and K-edge μXANES were collected on beamline 13-ID-E at the Advanced Photon Source at Argonne National Laboratory. Six thin sections, comprising depth profiles of samples from Site AB and Site AM on Coke Beach, were used to study the micro-scale spatial distribution and form of V and Ni. Preliminary μXANES measurements suggested the presence of micro-spatial variations in V concentration and coordination. Therefore, μXRF maps were collected using selected incident beam energies spanning the V K-edge. Selected energies (5460, 5469, 5486, 5492, 5600 eV) corresponded to spectral features that fluctuated in relative magnitude and would thus be sensitive to changes in V speciation. Micro-XRF mapping was also performed at a 15500 eV incident energy to acquire fluorescence data for the Ni Kα line. The synchrotron beam was focused to a 2x2 μm spot size. Samples were rastered across the beam and fluorescence counts were measured at each pixel (2x2 μm) with a dwell time of 25 ms $pixel^{-1}$ using a 4-element Si drift detector (Hitachi Vortex ME4). Beamline-specific software (GSECARS X-ray Microprobe Map Viewer, Version 8) and non-specific matrix manipulation software (Mathworks MATLAB 2010a) were used for XRF data processing. Target spots for μXANES were selected within the μXRF maps based on the location of zones of variable V and Ni concentration. Transects consisting of three to four spots were selected for μXANES measurements to assess spatial variability in V and Ni speciation within coke particles.

Reduction and processing of μXANES data were performed using Athena, a component of the Demeter software package (Version 0.9.21) running on the Ifeffit engine (Ravel and Newville, 2005). Linear combination fitting (LCF) was performed using the same software, using a fitting

range of -25 eV to +50 eV relative to the absorption edge, as this captured XANES features of interest. Vanadyl and Ni octaethyl and tetraphenyl porphyrins (VOOEP, VOTPP, NiOEP, NiTPP), vanadyl bis-phenyl butane dionate (VOPBD), roscoelite ($K(Al,V)_3Si_3O_{10}(OH)_2$) (Wong et al., 1984), and Ni oxide (NiO) standards were used for LCF. Finite difference modelling of the near-edge structure (FDMNES) (Bunau and Joly, 2009) of VOOEP (Molinaro and Ibers, 1976), VOPBD (Hon et al., 1965), NiOEP (Meyer, 1972), and NiTPP (Maclean et al., 1996) K-edge spectra was performed to assess effects of molecular distortion on XANES lineshape.

3.4 Results & Discussion

3.4.1 Aqueous Geochemistry

3.4.1.1 Geochemical parameters

Values of $\delta^{18}O$ and $\delta^{2}H$ ranged from -19.5 to -12.1 ‰ and -158.4 to -114.2 ‰, respectively. The lower, more depleted values generally corresponded to samples collected in the first 1 to 2 m below the water table and the higher, more enriched, values corresponded to deeper pore water samples. Precipitation samples (snow and rain) (Baer, 2014) exhibit a relationship ($y = 7.3x – 8.4$) very similar to the Syncrude local meteoric water line (LMWL) ($y = 7.2x – 14.6$). Oil sands process-affected water (MLSB water and CB deposit pore water) exhibited a relationship which was significantly different ($y = 6.2x – 34.9$) (Figure 3-2a). This trend is consistent with OSPW undergoing additional evaporative fractionation. Coke Beach pore water $\delta^{18}O$ and $\delta^{2}H$ values obtained in this study can be described as a mixture of local precipitation and MLSB process water (Figure 3-2a)..

Major ions including Na and Cl, ranging from 30 to 820 mg L^{-1} and 0.2 to 735 mg L^{-1} respectively, exhibited a sharp increase in concentration approximately 2 m below the water table. This trend was similar to that exhibited by stable isotopes of water values. There was thus a correlation between $\delta^{18}O$ values and concentrations of Na ($R = 0.85$) and Cl ($R = 0.77$) (Figure 3-2b). Electrical conductivity (EC) values ranged between 270 and 3740 µS cm^{-1} and increased sharply 2 to 3 m below the water table. Values of EC were well-correlated ($p << 0.05$) with alkalinity ($R = 0.86$) and major ions including Na ($R = 0.97$) and Cl ($R = 0.95$) suggesting shallow freshwater contained fewer ions and was therefore less electrically conductive.

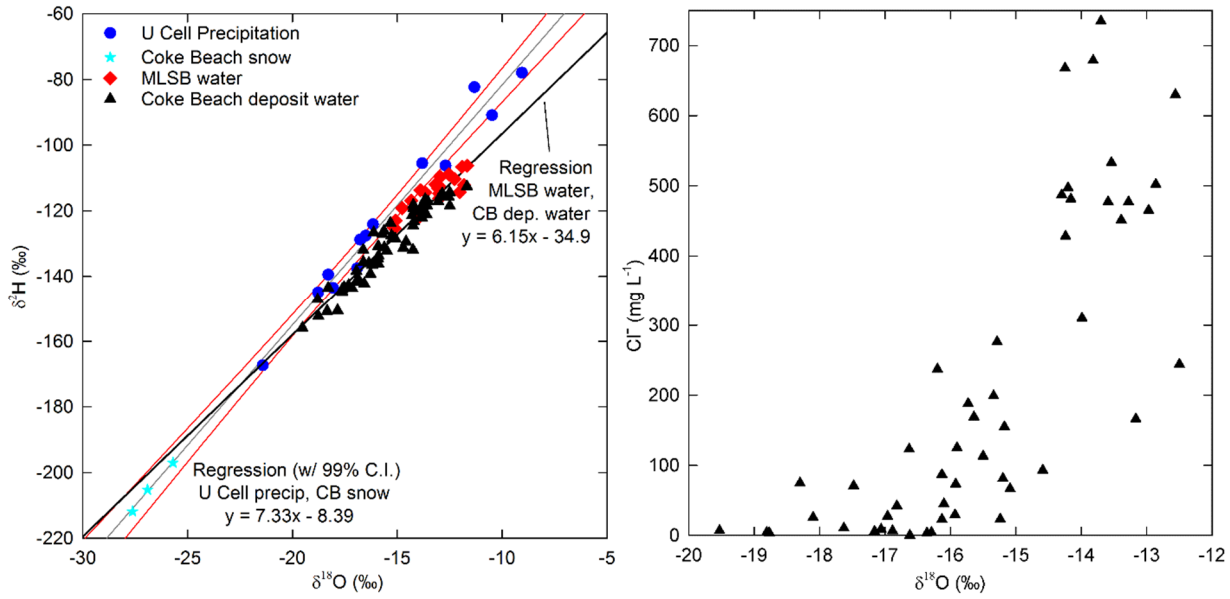

Figure 3-2. a) Comparison of Coke Beach deposit water with local precipitation and MLSB process water isotopic signatures. The linear regression for precipitation and snow samples (grey line) and 99 % confidence intervals (red curves), and the linear regression for MLSB and Coke beach deposit water (black line) are shown. All data from Baer (2014) except Coke Beach deposit water. b) Relationship between Na concentrations and $\delta^{18}O$ values.

The reduction-oxidation potential (Eh) values ranged from 0.1 to 0.5 V, and generally exhibited downward-decreasing trends, consistent with more oxidizing shallow pore water and more reducing deeper pore water. Sulfate concentrations varied between 35 and 550 mg L^{-1} and exhibited trends similar to those of EC, Na, Cl, and alkalinity to a depth of ~3.5 m below the water. Below this depth, sulfate concentrations decreased sharply. Conversely, while sulfide (S^{2-}) concentrations (Appendix H) at shallow depths ranged from 0 to 5 µg L^{-1}, sharp increases to 18 to 25 µg L^{-1} were observed at depths greater than 6 m at Sites A, AB, and AX, suggesting reducing conditions. Deviations from this redox profile are interpreted to be caused by pulses of fresh precipitation influx followed by re-establishment of the process water signature. Hydraulic deposition and the relatively homogenous physical properties of coke result in good sorting and high permeability in coke deposits (Zubot, 2010; Lahmira et al., 2013). These factors are likely responsible for the strong geochemical mixing in the shallow part of uncovered coke deposits.

Pore water pH values ranged from 6.2 to 8.4 and generally exhibited downward-increasing trends. Concentrations of Ca, Mg, Sr, Ba, and Mn were elevated in a zone 1 to 3 m below the water table. However, these elements often exhibited low concentrations immediately below the water table. This group of elements is often generally associated with carbonate minerals. The low pH

near the water table could lead to carbonate dissolution, thus mobilizing these elements in this zone. Low concentrations in the very upper saturated zone were most likely a result of freshwater dilution. Pore water Fe concentrations display a similar trend to Mn at Sites A, AM, and B, suggesting that carbonate dissolution may also contribute to Fe mobility. At Site AB and AX, Fe concentrations exhibit a downward-increasing trend. This comportment may be more indicative of a redox control consistent with shallow oxic conditions and deep reducing conditions. Iron(III) is much less soluble than Fe(II), at circumneutral pH, so shallow Fe concentrations at these sites may be low due to precipitation of Fe(III) oxyhydroxide phases.

There was a zone of elevated NH_4^+ pore water concentrations between 1.5 and 2.0 m below the water table at all locations (Figure 3-3b). This trend was not consistently correlated with the depth profile of other analytes, indicating that NH_4^+ mobility may be influenced by different factors. The observed maximum could be a result of ion exchange of NH_4^+, or perhaps biodegradation of organic material in coke by microbial communities at that depth. A consistent concomitant decrease in another major cation would be expected at the same depth if a cation exchange mechanism was responsible. However, no consistent inverse relationship was observed between NH_4^+ and any other major cation for all sites. There was also insufficient evidence to substantiate a biodegradation mechanism leading to depth-specific NH_4^+ release.

There exist some limitations on the interpretation of coke deposit pore water data because samples were collected at a single time point. Geochemical parameter depth profiles which were partially inconsistent with the trends described above (Site B, Figure 3-3) suggest transient near-surface conditions. No values have been reported for the field hydraulic conductivity of Syncrude fluid petroleum coke but values are expected to be similar to sand, based on particle size distribution. Typical saturated K values for sand are between 10^{-6} and 10^{-3} m s^{-1} (Freeze and Cherry, 1979). If the assumption that coke behaves similarly is valid, precipitation events may have rapid influence on geochemical conditions near the water table. Aeolian removal of fine coke particles near surface and mechanical sorting resulted in preferential coarsening of the upper ~0.5 m at CB, further promoting rapid infiltration of precipitation.

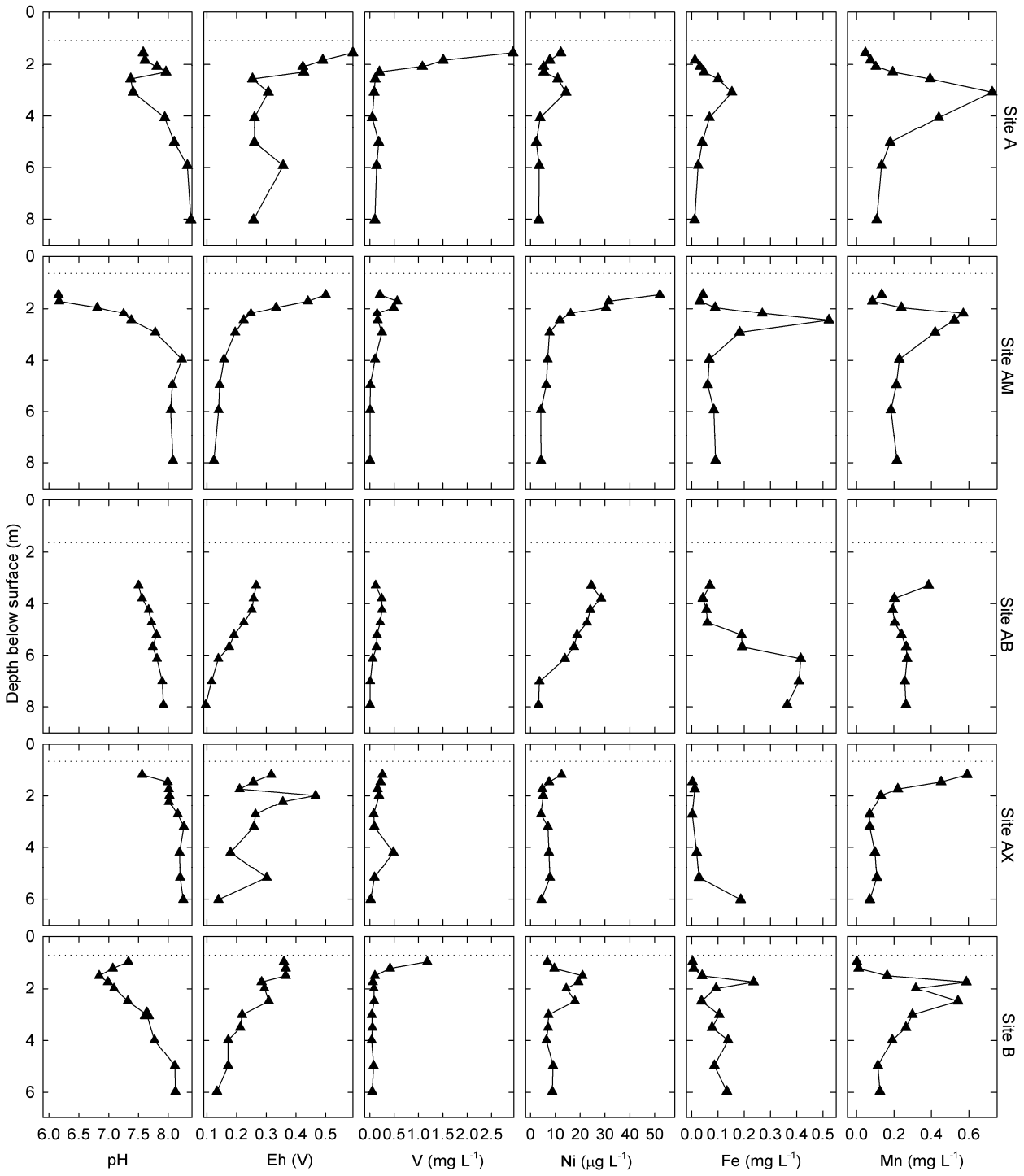

Figure 3-3a. Depth profiles of pore-water pH, Eh, V, Ni, Fe, and Mn for Sites A, AM, AB, AX, and B at Coke Beach. The horizontal dotted line represents the water table elevation at the time of sampling.

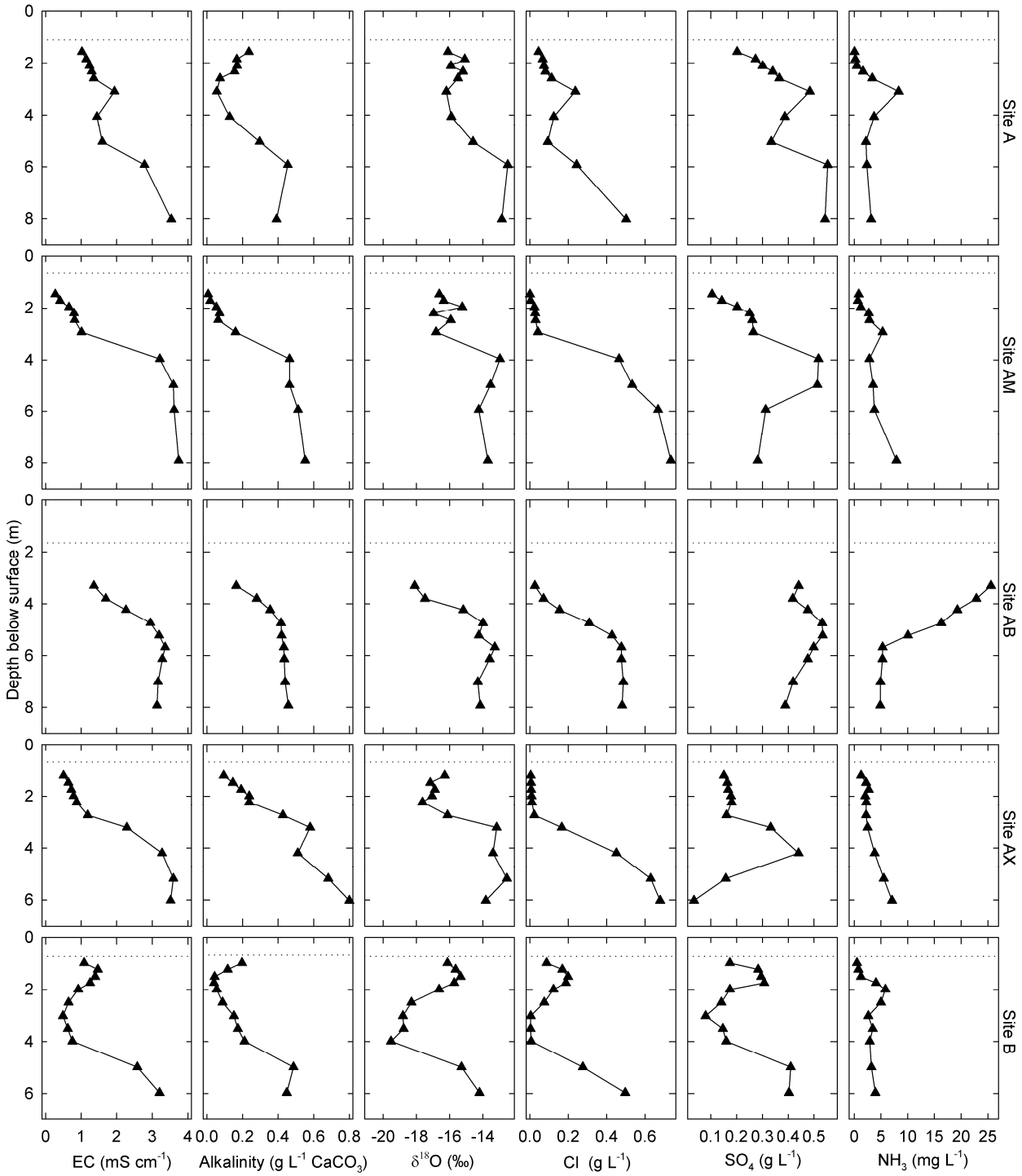

Figure 3-3b. Depth profiles of pore-water electrical conductivity, alkalinity (as $CaCO_3$), $\delta^{18}O$, and concentration of chloride, sulfate, and N as NH_3 for Sites A, AM, AB, AX, and B at Coke Beach. The horizontal dotted line represents the water table elevation at the time of sampling.

3.4.1.2 Vanadium and nickel

Vanadium pore water concentrations varied between < 0.01 and 2.95 mg L^{-1}, and often exhibited an overall downward-decreasing trend significantly ($p << 0.05$) correlated with Eh values ($R = 0.65$) (Figures 3-3, 3-5). Pore water redox conditions suggested that V should be present in the V(V) oxidation state predominantly as $VO_2(OH)_2^{1-}$ (Figure 3-5a) despite solid-phase speciation being dominated by organically-complexed V(IV) (as VO^{2+}) and inorganic V(III) (Chapter 2, this thesis). Higher Eh values indicate more oxidizing conditions, and V(V) oxyanionic aqueous species generally have a higher mobility than reduced V species (Wehrli and Stumm, 1989). Considerable oxygen ingress is expected in the upper zone of the uncovered CB deposit given the high permeability of coke deposits (Lahmira et al., 2013). Li et al. (2007) reported that both V(IV) and V(V) species could be found in the pore water of a capped coke deposit; however, Jensen-Fontaine (2012) demonstrated that V(IV) species can rapidly oxidize to V(V) in oxic settings.

At shallow depths in some wells, infiltration of precipitation depressed the pH to <6.5. The mobility of V generally decreased under more acidic, though oxic, conditions resulting in complex V comportment immediately below the water table. Pourrezaei et al. (2014) found the point of zero charge (pH_{PZC}) of oil sands fluid coke to be 6.5 ± 0.3. The net coke surface charge was therefore expected to be negative at most observed field conditions where pH was neutral-alkaline. However, pH values near the water table, at or slightly below the pH_{PZC}, might generate positively-charged surfaces that could promote adsorption of aqueous V(V) oxyanionic species. More labile V(V) anionic species may be preferentially adsorbed to coke surfaces under these conditions, leaving the less abundant, reduced, V(IV) species as the dominant phases in pore water. Several previous laboratory studies have found that, in general, V(V) leachability and mobility increases at alkaline pH, which supports the field data from this study well (Wehrli and Stumm, 1989; Puttaswamy and Liber, 2011; Pourrezaei et al., 2014). Specifically, V release from coke to the liquid phase was previously observed at higher pH (Zubot, 2010). However, longterm interactions between coke and OSPW exhibited a mechanism which gradually decreased the aqueous V concentration (Zubot et al., 2012). This result suggests the partitioning of V between coke and the aqueous phase may dynamically fluctuate in coke deposits. Aqueous V mobility below the maximum sampling depth of 8 m is expected to be limited by anoxic, alkaline conditions.

Pore water Ni concentrations ranged between 2 and 60 μg L^{-1} in the CB deposit, and exhibited a significant ($p << 0.05$) strong negative correlation with pH (R = -0.80) (Figure 3-4). Nickel was not correlated to Eh trends at any location. Nickel is less redox-sensitive than V, existing exclusively in the Ni(II) oxidation state (Figure 3-5b). While Ni pore water speciation itself is not fully understood, the concentration of Ni was consistently higher at more acidic pH values, with no notable exceptions at any location. This relationship was observed in a previous laboratory study. Aqueous Ni concentrations in coke pore water were found to decrease at more alkaline pH (Zajic et al., 1977). Elevated sulfate concentrations, present in OSPW, have been associated with greater leaching of Ni and, more generally, other cationic metal species (Puttaswamy and Liber, 2012). Nickel and sulfate concentrations were not correlated in the CB deposit dataset because the system is further complicated via dilution by low ionic-strength slightly-acidic precipitation, presence of other ions, variable redox conditions, and solid-phase Ni speciation. While aqueous Ni concentrations in coke pore water were generally low, the strong correlation with pH suggests that if deposit geochemical conditions became more acidic in the future, additional Ni could be mobilized from coke. Coke pore water Ni concentrations below the sampling depth are likely low, since alkaline conditions are expected to dominate in the absence of precipitation infiltration.

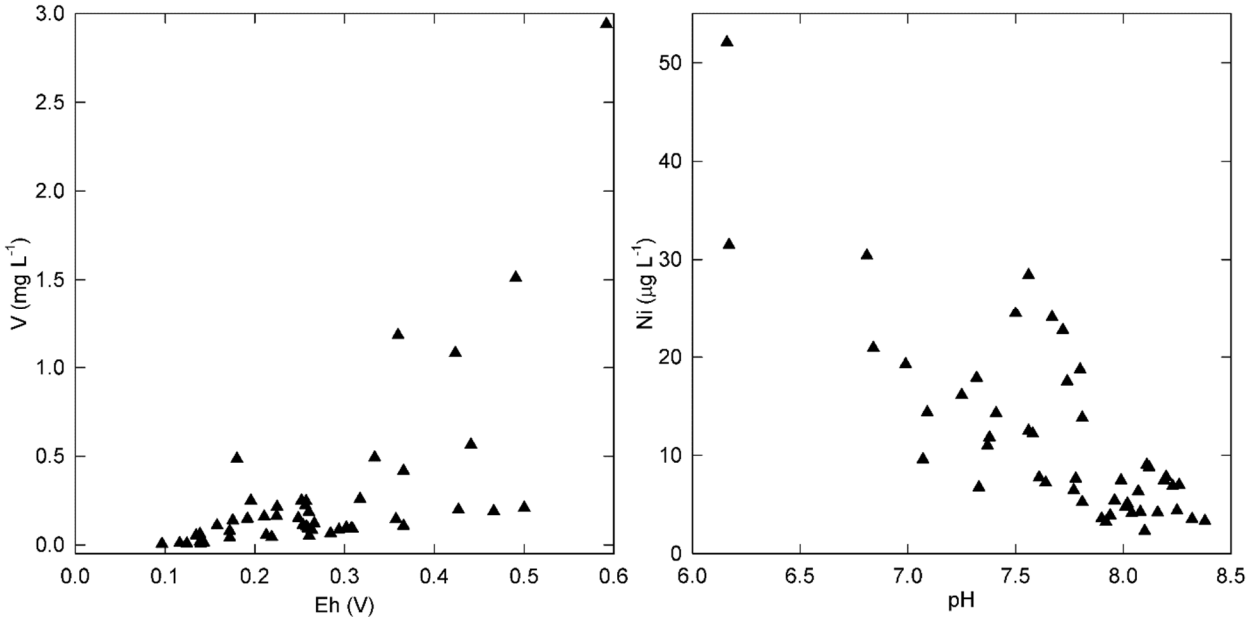

Figure 3-4. Relationships between trace metal pore water concentrations, pH, and Eh.

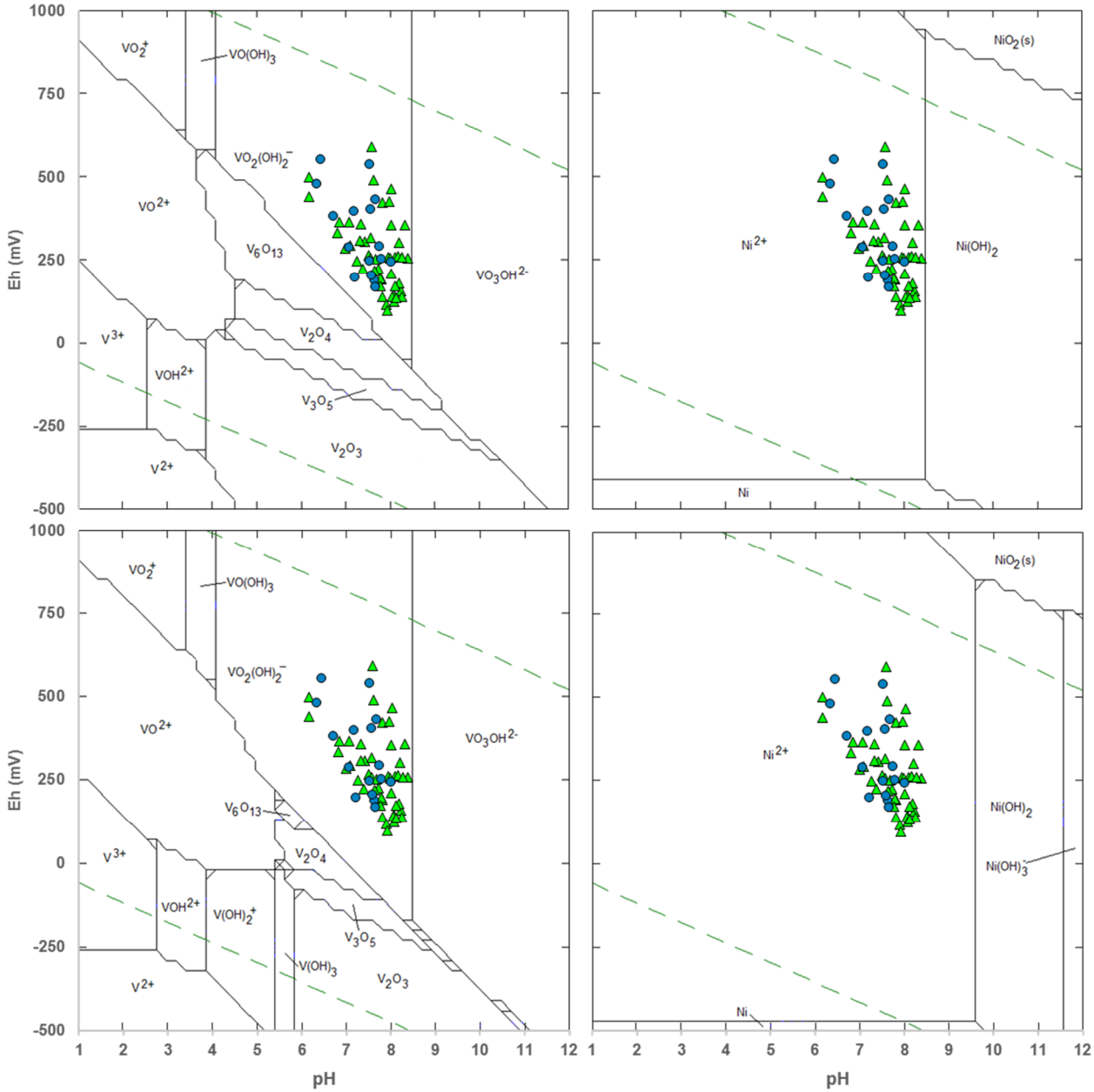

Figure 3-5. Eh-pH coke deposit pore water speciation predominance diagrams for V (a,c) and Ni (b,d) under shallow conditions (ionic strength = 0.01 M, $[V]_{tot} = 6x10^{-5}$ M, $[Ni]_{tot} = 1x10^{-6}$ M) (a,b) and deep conditions (ionic strength = 0.06 M, $[V]_{tot} = 1x10^{-6}$ M, $[Ni]_{tot} = 2x10^{-8}$ M). Green triangles signify Coke Beach samples (Figure 3-3a) and blue circles signify Coke Watershed samples (Appendix H).

Mass balance calculations estimated the fraction of V and Ni released from coke into the aqueous phase. Mean solid-phase V (1280 mg kg^{-1}) and Ni (230 mg kg^{-1}) concentrations (Chapter 2, this thesis), maximum pore-water V (2.95 mg L^{-1}) and Ni (0.06 mg L^{-1}), dry bulk density (1090 kg m^{-3}; Har, 1981), typical bulk porosity (~0.3), and saturated steady-state conditions were

assumed. This calculation yielded extremely small aqueous-to-solid partitioning coefficients for both V (0.063 %) and Ni (0.007 %). The highest observed pore water V and Ni concentrations are small compared to the total solid-phase concentrations. These concentrations are consistent with (same order of magnitude as) coke lysimeter pore water values and pore water concentrations calculated from leaching experiments (Kessler and Hendry). Thus the solid-phase fraction which hosts readily leachable V and Ni is either volumetrically small or is contained within coke grains in such a way that it is largely inaccessible to pore water.

3.4.2 Solid-Phase Micro-Spatial Geochemistry

3.4.2.1 Electron micro-analyses

The core of coke particles most often consisted of a small fragment of a previous coke particle but could occasionally be comprised of an inorganic particle. The remainder of most coke particles consisted of a series of sub-spherical, concentric layers (Figure 3-6). Each layer was comprised of a ~8 μm thick organic-rich ring with a ~2 μm thick inorganic-rich ring margin. Energy dispersive X-ray (EDX) spectra collected using both TEM and EMP confirmed that the chemistry of organic-rich rings was dominated by C and S, and the inorganic-rich ring margins exhibited elevated K, Al, Si, Ca, Mg, and often Fe and Ti (Chapter 2, this thesis).

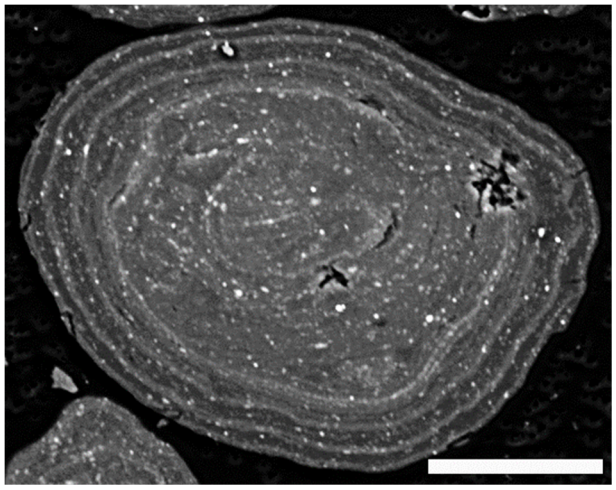

Figure 3-6. Backscattered electron image of coke particle (sample DM550) showing the core of the grain, and several alternating concentric organic-rich rings (darker) and inorganic-rich ring margins (lighter). Small bright spots are crystalline inorganic mineral fragments. Scale bar is 50 μm.

Micro-XRF mapping at the V Kα line often revealed distinct Ti-bearing particles hosted throughout coke particles because V Kα and Ti Kβ lines overlap in energy. The morphology and lack of consistent correlation with other elements suggest that these were crystalline Ti oxide

micro-particles (rutile). Synchrotron powder X-ray diffraction (Chapter 2, this thesis) data also suggested the presence of this phase. Overlap of the V Kα and Ti Kβ fluorescence lines was accounted for by subtracting an empirically-derived factor (typically 0.1 – 0.2) of the Ti Kα map from the V Kα map to remove disseminated Ti hotspots from the V Kα map. Occasionally, a spatial correlation was observed between Ti and Fe in micro-particles, which suggested the presence of an ilmenite-like phase. This finding was corroborated by previous bulk coke Fe K-edge XANES analysis (Chapter 2, this thesis).

3.4.2.2 Vanadium and nickel μXRF and μXANES

Micro-scale XRF mapping displayed a heterogeneous, concentric V and Ni spatial distribution within the majority of coke particles (Figure 3-7). Vanadium and Ni were found throughout coke particles, but were generally concentrated in the inorganic-rich ring margins. Vanadium and Ni K-edge μXANES spectra varied between alternating rings and ring margins in coke particle cross-sections. Vanadium μXANES spectra from rings were most qualitatively similar to bulk coke V spectra. Bulk coke V K-edge XANES spectra pre-edge peak magnitudes were generally consistent with the V(IV) oxidation state (Chapter 2, this thesis). Fitting of bulk coke V K-edge XANES spectra (Figure 2-7, Table 2-4) suggested that a combination of square-pyramidal N and O coordination explained the lineshape. This finding is generally consistent with the organic-rich composition of the rings.

Vanadium K-edge μXANES spectra acquired in the ring margins consistently displayed a different type of V speciation (Figure 3-7b). The pre-edge peak magnitude in these spectra was smaller than in spectra from organic regions. These spectra exhibited a doublet feature at ~5486 and ~5499 eV, which was not observed in spectra for porphyrin-like compounds or asphaltene samples (Lytle, 1983). Spatial variations within coke grains suggested alteration of the local atomic coordination of V during fluid coking. The doublet feature in the spectra from ring margins was characteristic of octahedrally coordinated V(III) (Maylotte et al., 1981; Wong et al., 1984). The spectra from ring margins quantitatively resembled that of V(III) substituted into distorted octahedral oxygen-coordinated sites in phyllosilicate minerals (Wong et al., 1984). The phyllosilicate roscoelite, which contains V(III) coordinated in this manner, exhibits V K-edge XANES spectra (Wong et al., 1984) similar to ring margins of coke particles. Roscoelite-like, distorted octahedrally-coordinated V(III) was previously observed in coals (Maylotte, et al., 1981). Compounds like V_2O_3 and V_2S_3 (Maylotte et al., 1981), and V substituted into some ferro-titanian

oxides (Balan et al., 2006) also represent V(III) in octahedral coordination. However, while the overall XANES lineshape of these spectra were qualitatively similar to spectra from the ring margins in coke particles, energy positions and relative magnitudes of these peaks were different.

Fitting V K-edge μXANES spectra from different regions within coke particles provided insight into the distribution and relative proportions porphyrin-like V(IV) square-pyramidal N coordination, dionate-like V(IV) square-pyramidal O coordination, and roscoelite-like V(III) distorted octahedral O coordination. At spot V3 – an organic-rich ring (Figure 3-7a) – LCF suggested the square pyramidal vanadyl porphyrin-like components described >65 %, and the distorted octahedral inorganic V(III) component <30 %, of the experimental V spectra. At spot V1 – a ring margin (Figure 3-7a) – the square pyramidal vanadyl type components described only <45 %, and the distorted octahedral V(III) component >50 %, of the experimental V spectra (Table 3-1). The R-factor for all fitting results was <0.0050 indicating a good quality of fit. The sum of components for all fitting results remained consistent and close to 100 % when the sum was unconstrained, indicating that these are likely the only dominant phases.

Coke Ni K-edge XANES spectra consistently showed a distinct doublet feature on the white line with peaks at ~8352 and ~8359 eV. All spectra exhibited a rounded shoulder at 8340 eV and a small pre-edge feature at 8334 eV. Nickel μXANES spot Ni2, and other spectra from organic rings, were most comparable to bulk Ni spectra (Figure 3-7d), which were generally consistent with porphyrin-like, square-pyramidal N coordination. Progressing from spot Ni2 to Ni1 to Ni3, the lower energy peak of the doublet feature not only increased in magnitude, but also shifted slightly from ~8352 eV to ~8351 eV. The Ni μXANES lineshape after ~8370 eV is similar among spots, and consistent with that of bulk coke. Nickel K-edge XANES spectra for asphaltene samples (Lytle, 1983) were essentially identical qualitatively and quantitatively to spectra for a Ni porphyrin compound (Figure 3-8b). This finding indicated that the initial Ni coordination is porphyrinic and that the fluid coking process alters this coordination. Two potential mechanisms are proposed to account for the observed micro-scale spatial variability in Ni coordination between rings and ring margins.

The reversal in magnitude of the two peaks and the broadening of the 8340 eV shoulder could be due to considerable distortion of the organo-metallic asphaltenic Ni site during coking. Finite difference modelling of the near-edge structure of Ni porphyrin molecules demonstrated that inflation and deflation of the overall molecular structure strongly influenced Ni XANES

doublet feature lineshape (Appendix G). Structural inflation of atomic distances around the Ni metal centre of 3-10 % caused the lower energy peak of the doublet feature to increase in magnitude; generating lineshapes similar to that observed at spot Ni3. While there may be distortions and variability in Ni speciation proximal to the organo-metallic Ni centres in asphaltenic micelles, the spectral similarity among all spots at higher energy implies an underlying constant long-range Ni speciation.

Secondly, conditions during fluid coking may be distort asphaltenic Ni sites such that Ni is liberated from the organic phase and oxidized forming an inorganic phase. Nickel(II) oxide, for example, typically displays a strong whiteline feature at ~8350 eV but no secondary peak at ~8359 eV, and a pre-edge peak at 8333 eV but no shoulder at 8340 eV (Figure 3-7d). Fitting Ni μXANES spectra with porphyrin and NiO standards yielded quantitatively acceptable fits (R-factor <0.03) (Table 3-1b) but qualitatively poor fits (Figure 3-8b). Spectra for many inorganic Ni compounds (sulfate, hydroxide, carbonate) exhibit similar lineshapes; therefore, including more than one inorganic standard in fitting resulted in assignment of negative component weights. Consequently, the NiO reference spectrum, in addition to Ni porphyrin spectra, provided the best fit. While the relative magnitudes of the doublet peaks were reasonably well approximated, it was not possible to simulate the dampening of the 8340 eV shoulder (Figure 3-8b). This inconsistency could be due to a contribution from an unknown Ni-bearing phase or could be explained by variability in the magnitude of distortion in Ni asphaltenic sites in coke.

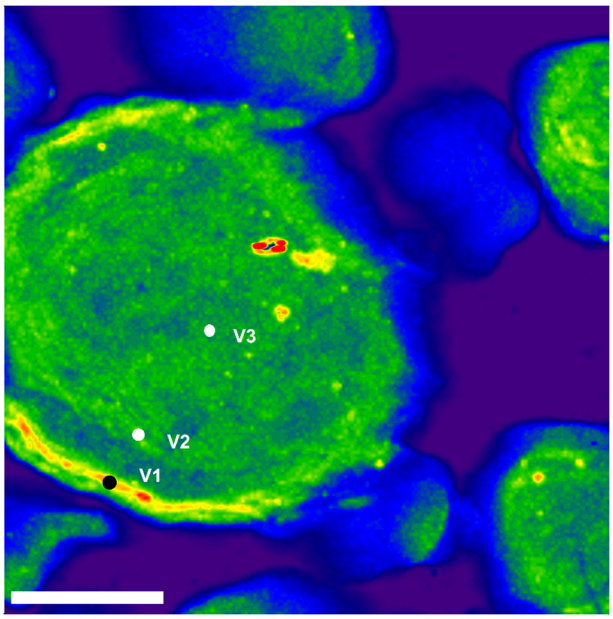

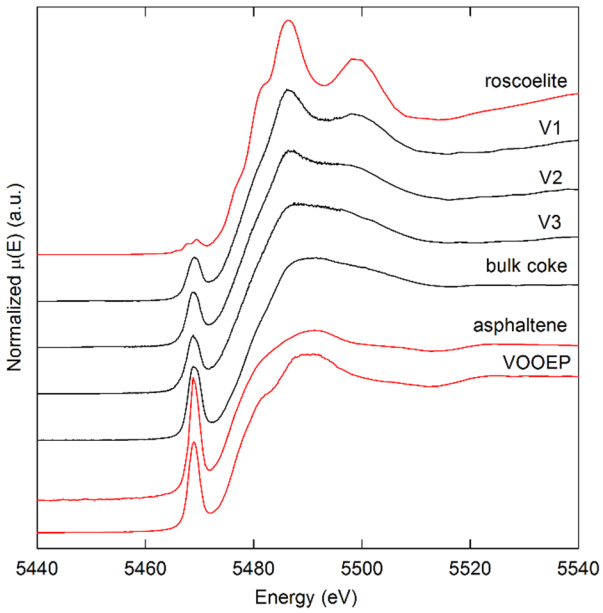

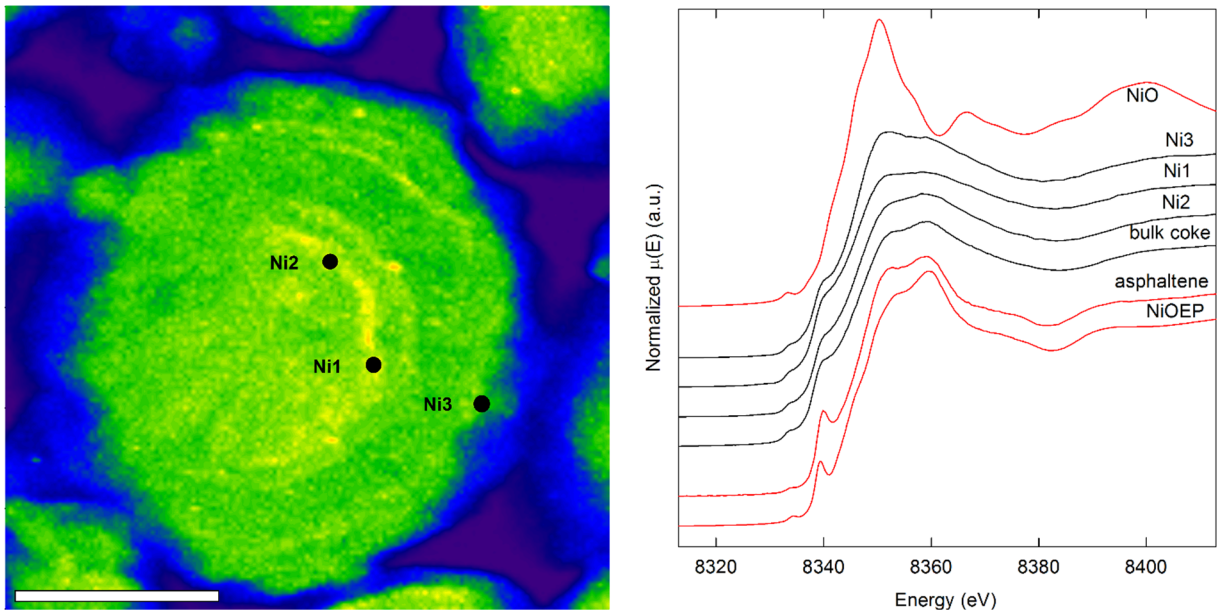

Figure 3-7. a) Vanadium Kα μXRF map (sample AB200 Map3), collected with a 5600 eV incident energy, Ti Kβ-subtracted. Scale bar is 100 μm. Note that the point hotspots are Ti (oxide) micro-crystals for which the Ti Kβ signal could not be fully subtracted. b) Comparison of V μXANES spectra from spots V1, V2, and V3 with bulk coke, asphaltene (Lytle, 1983), vanadyl octaethyl porphyrin, and roscoelite spectra. c) Nickel Kα μXRF map (sample AB700b Map 1); collected with a 15500 eV incident energy. Scale bar is 100μm. d) Comparison of Ni μXANES spectra from spots Ni3, Ni1, and Ni2 with bulk coke, asphaltene (Lytle, 1983), Ni octaethyl porphyrin, and Ni oxide spectra.

Table 3-1. Linear combination fitting results for V K-edge μXANES at three different spots in a coke particle (sample AB200, Map 3). Linear combination fitting results for Ni K-edge μXANES at three different spots in a coke particle (sample AB700, Map 1).

Spot	Roscoelite	VOOEP	VOTPP	VOPBD	Sum	R-factor
V1	53 ± 1 %	23 ± 1 %	18 ± 2 %	10 ± 2 %	103 %	0.0016
V2	34 ± 1 %	50 ± 2 %	9 ± 2 %	11 ± 3 %	104 %	0.0027
V3	25 ± 1 %	59 ± 2 %	9 ± 3 %	12 ± 3 %	104 %	0.0046
	NiO	**NiOEP**	**NiTPP**		**Sum**	**R-factor**
Ni3	25 ± 1 %	36 ± 2 %	36 ± 2 %		97 %	0.0053
Ni1	18 ± 2 %	13 ± 4 %	65 ± 5 %		96 %	0.0269
Ni2	12 ± 2 %	39 ± 3 %	44 ± 4 %		95 %	0.0170

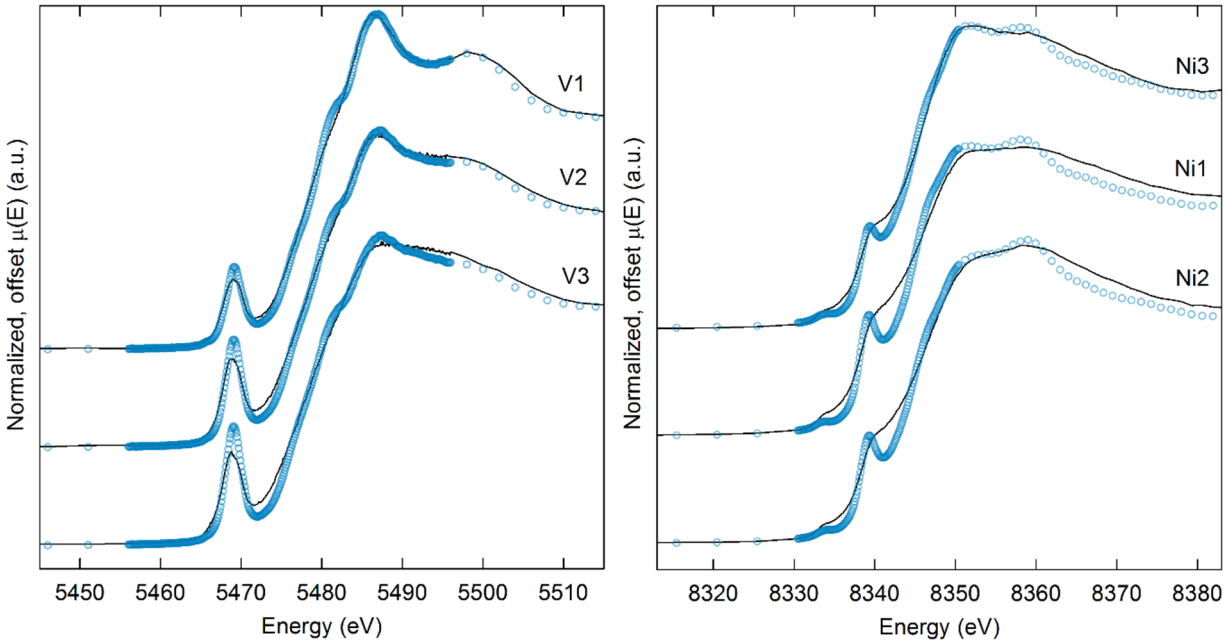

Figure 3-8. a) Vanadium K-edge μXAS spectra showing the representative range of variability in speciation. Spectra collected at three points in a single coke particle: Spots V1 (ring margin), V2 (intermediate), V3 (organic ring / core). Open circles show fit. b) Nickel K-edge μXAS spectra showing the representative range of variability in speciation. Spectra collected at three points in a single coke particle: Spot Ni3 (ring margin, rim), Spot Ni1 (intermediate), Spot Ni2 (organic ring / core). Open circles show fits.

3.4.2.3 Vanadium speciation mapping

While μXANES provided detailed speciation information for selected spots, speciation maps of entire coke particles were more revealing. The ratio of the magnitude of the X-ray absorption at 5486 eV and 5492 eV was found to be diagnostic of V speciation (Figure 3-8b). A ~1:1 ratio corresponds to background organic speciation whereas increasingly higher ratios indicate the presence of the doublet feature (Figure 3-8b). By collecting two spatially-coincident V Kα μXRF maps using incident beam energies of 5486 eV and 5492 eV, this ratio could be calculated pixel-by-pixel for the entire map area (Figure 3-9b). While pure roscoelite itself is not necessarily presumed present in coke, this evidence very strongly suggests that V is locally concentrated within the concentric rings as V(III) octahedrally coordinated by oxygen in a phyllosilicate phase.

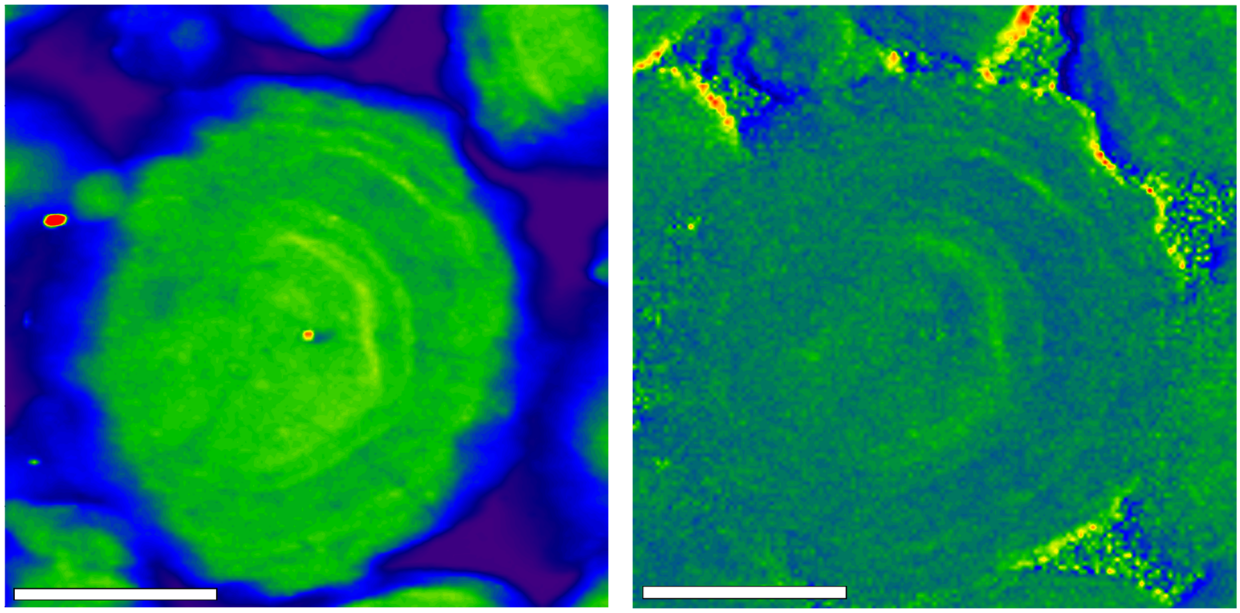

Figure 3-9. a) Vanadium Kα μXRF map, sample AB700b Map 1; collected with a 5600 eV incident energy, Ti Kβ-subtracted; b) Vanadium speciation map of sample AB700b Map1, pixel-by-pixel quotient of 5486 eV & 5492 eV incident energy VKα maps, Ti Kβ-subtracted. Scale bars 100 μm.

3.4.3 Conceptual Model

Observed micro-scale spatial variations in V and Ni solid-phase speciation have a number of potential implications for V and Ni release and mobility. Fluid coke particles grow within the coker and accumulate V and Ni derived from the bitumen feed, but the mean V and Ni concentrations in the bitumen feed are only 250 and ~85 mg kg^{-1} respectively (Har, 1981; Booz-Allen & Hamilton Inc., 1982). Porphyrin-like organically-complexed coordination is relatively stable (Lewan and Maynard, 1982; Dechaine and Gray, 2010), and is therefore unlikely to be a principal source of V or Ni released to coke pore water.

Fluid coking involves multiple cycles of organic material addition to the surface of sub-spherical grains as coke particles are continuously circulated from the coker to the burner vessel. This process accounts for the observed concentric morphology, but does not explain the radial fluctuations in trace metal concentration. In the coker vessel, a layer comprised mostly of organic, asphaltenic molecules – with some disseminated micron-sized inorganic particles – is added to the subspherical surface of each coke particle. During the brief residence time in the burner vessel (i.e., < 30 seconds), a portion of this organic material layer is partially oxidized/combusted (Blaser, 1992; Zubot, 2010). This slight combustion could be sufficient to burn off some of the organic material, liberating a fraction of the metals from the asphaltenic metal sites where they were hosted

in the bitumen feedstock. These metals become concentrated on the partially-combusted particle surface and are left behind there with the remaining, uncombusted inorganic fraction (ash). The subsequent coker vessel cycle then adds another layer of primarily-organic material, and the cycle continues, each time generating a ring of concentrated inorganic material and liberated metals. A study of organo-metallic sites in asphaltenes showed that V sites tended to be located near the periphery of micelles, whereas Ni sites tended to be found closer to the centre (Bausell et al., 1992). Therefore, the extreme conditions in fluid coking may preferentially liberate more V than Ni from the organic phase. However, the Ni metal sites left intact in the interior of asphaltenic micelles may still undergo structural modifications (Miller and Fisher, 1999). In coke grain ring margins, V appears to be hosted largely inorganically, while Ni is hosted either inorganically or in strongly distorted organic sites. Critically – since it is from the burner vessel that the coke particles which have grown too large are extracted for slurrying to deposition areas – the outer rim of most coke particles will be an inorganic ring margin. This phenomenon was observed in most V and Ni μXRF maps.

Chung et al. (1996) suggested that the metal-containing compounds in coke are stably hosted in the carbon matrix, so their potential for contact with pore water, and furthermore their leachability, are limited. This suggestion is likely true of the stably-bound, organically-complexed V and Ni in coke particle rings. However, erosion, weathering, or fragmentation of coke particles could directly expose the ring margins of inorganically-hosted elements to pore water. Even though the organic rings generally comprise more volume than ring margins in coke particles, higher V and Ni concentrations and less stable, inorganic speciation in ring margins may pose a greater risk of mobilization.

3.5 Conclusions

The current research aimed to determine how trace metal release from fluid petroleum coke was linked with coke deposit aqueous-phase geochemistry and micro-scale variations in speciation. Relationships were established between groundwater redox geochemical conditions and trace metal release. Groundwater depth profiles of pH, EC, major inorganic ions, stable isotopes of water, and cationic trace metals (Ni) showed considerable mixing between the slightly-acidic low ionic strength precipitation and underlying OSPW pore water. Profiles for Eh, sulfate, sulfide, and anionic trace metals (V), and Fe provided evidence for oxygen ingress and mixing. The effects of water-mixing and redox-mixing often overprinted to generate complex depth

profiles for the aqueous parameters influenced by both factors. In general, water depth profiles from the current study show that unsaturated, oxic coke storage conditions may lead to the mobilization of V from coke into the process water. Saturated anoxic conditions would therefore be preferable for the storage of coke in the field in order to minimize V release. The micro-scale spatial variations in trace metal concentration and speciation within petroleum coke particles were then studied, in order to explain the mobilization mechanism. Concentric zonation of trace element (V & Ni) concentration and speciation was categorically observed via EMP EDX, synchrotron μXRF and μXANES data, and was concluded to be a direct effect of the fluid coking process. Vanadium and Ni were both concluded to be organically-complexed in coke. However, oxidation and partial combustion during the coking process was found to transfer some V to an inorganic phase and distort Ni organo-metal centres.

CHAPTER 4 CONCLUSIONS

4.1 Summary of Findings

The objective of this research was to better understand how trace element (V and Ni) speciation and redox geochemical conditions control metal mobility in petroleum coke deposits. This question was examined by assessing spatial variation in redox geochemistry in three coke deposits, studying V and Ni solid-phase speciation in coke, and linking aqueous-phase geochemical factors to V and Ni mobilization.

Bulk elemental analyses confirmed that coke composition is dominated by C (84.2 ± 2.3 wt. %) and S (7.0 ± 2.6 wt. %). Coke was also found to contain a secondary fraction of inorganic material, including Si, Al, Fe, Ti, Ca, K, Na, and Mg, as well a suite of trace elements dominated by V (1280 ± 120 mg kg^{-1}) and Ni (230 ± 80 mg kg^{-1}). Phase identification of synchrotron PXRD patterns showed that coke contains aromatic carbon crystallites, Si and Ti oxides, a hydrated Ni sulfate phase, an organically-complexed porphyrin-like V phase, and muscovite or a similar phyllosilicate phase. Furthermore, EMP EDX analyses revealed micro-crystals of Ti-Fe (oxide), K-Al-Si-Mg (phyllosilicates), Ca-Mg (carbonates), pyrite, and quartz.

A number of bulk coke elemental correlations were observed. Carbon, S, V, and Ni were all correlated because of their general association with the organic coke matrix. Iron and Ti were strongly correlated likely due to their association in oxide micro-particles. Potassium, Al, Mg, and to a lesser extent Si were correlated in relation to the phyllosilicate phases in coke. The correlation of P and REES agree with EDX spot analyses in predicting monazite micro-crystals. Strontium was correlated to Ca, potentially indicating its substitution in carbonate minerals. No statistically significant differences in bulk elemental composition between the three coke deposits studied were observed.

Bulk V K-edge XANES revealed that all samples show very similar speciation; porphyrin reference spectra explained the overall shape of the near-edge, but a second phase was needed to explain higher absorption (5486 & 5498 eV) on either side of the characteristic rounded porphyrin whiteline feature (5492 eV). Bulk Ni K-edge XANES exhibited slight variation among samples in the relative height of two spectral features (8352 & 8359 eV). Bulk S K-edge XANES revealed

that all samples have essentially identical S speciation. Fitting results suggested that S sites in coke are at least locally thiophenic in character. This finding corroborates previous investigations of S speciation in SCL fluid coke using XPS, and in asphaltenes using XANES. There was some variability in Fe K-edge XANES at the bulk scale, though no trends with location or depth were apparent. Spectra were dominated by pyrite and ilmenite-magnetite phases, both corroborated by EDX. A minor oxyhydroxide component could be present; this was also predicted by thermodynamic aqueous-phase modelling.

The onion-skin morphology of coke particles was confirmed by SEM analyses, displaying concentric subspherical layers of higher atomic number elements. Interstitial zones between successive shells tend to display perpendicularly-radiating rapid-crystallization structures. Vanadium K-edge μXANES spectra corresponding to concentric zones relatively consistently display higher absorption at 5486 eV and 5498 eV, creating a doublet feature. Further, the pre-edge peak is shorter and shifted by up to +0.6 eV. The lineshape of this doublet feature and pre-edge position and magnitude agree well with roscoelite spectra acting as a proxy for V(III) substituted in a distorted octahedral oxygen-coordinated phyllosilicate site. EMPA EDX confirmed aluminosilicate content and V concentration was greater in the ring margins, implying that phyllosilicate-hosted, or at least inorganically-complexed, V could feasibly be present. Nickel K-edge μXANES spectra corresponding to ring margins often displayed considerable increases in magnitude to the lower-energy peak of the doublet feature. Modelling showed that a similar change could be effected by slight inflation (distortion) of the interatomic distances around the organically-complexed Ni site. It is also possible that an inorganic Ni phase, such as Ni oxide, was responsible for this change to the spectral lineshape.

Groundwater geochemical parameters – pH, EC, major ions, and stable isotopes of water ($\delta^{18}O$ and $\delta^{2}H$) – all displayed consistent increasing-downward trends and agree on the extent of precipitation infiltration; Eh is highest just below the water table and decreases downwards (Figure 4-1). At all sites, pH displays a very strong negative correlation with Ni release. Redox potential (Eh) exhibits a positive correlation with V release, though at some sites, lower pH conditions induced by precipitation infiltration tend to inhibit mobility. Mass balance calculations suggest that only very small fractions of the total V and Ni need to be released from coke in order to generate elevated aqueous phase concentrations.

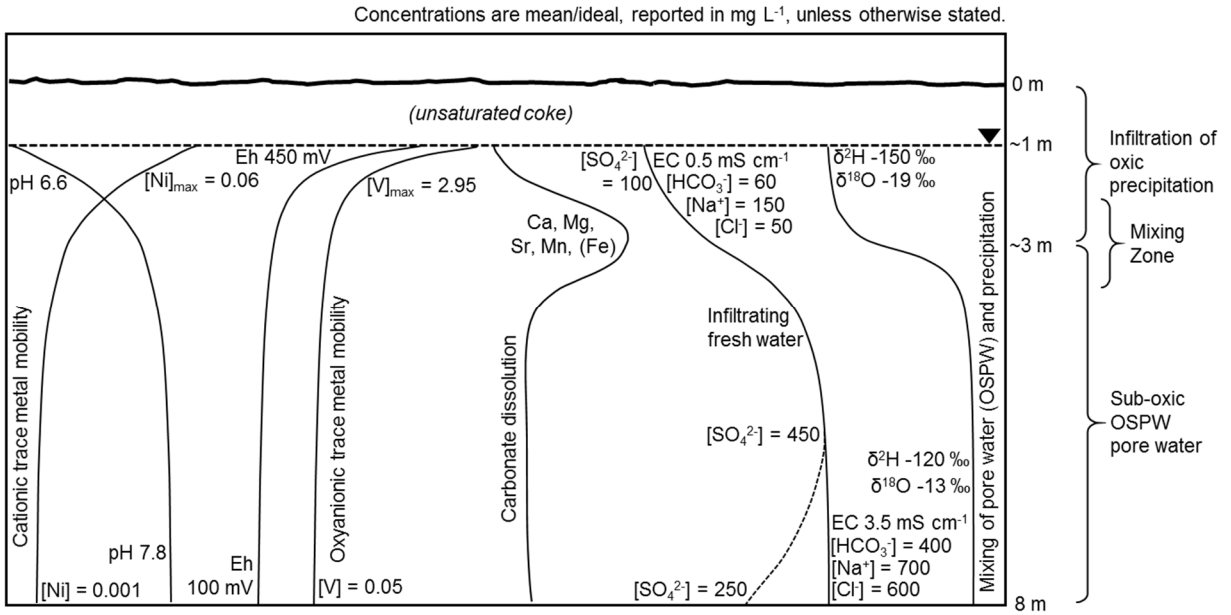

Figure 4-1. Conceptual model of uncovered coke deposit pore water geochemistry.

4.2 Recommendations

Column experiments to controllably test effect of redox, pH, depth, saturation, pore water ionic strength on the release of metals from coke are advised for future work. Now that many of these relationships have been observed in the field, it would be beneficial to test them individually to further deconvolute their individual contributions. It would also be valuable to more explicitly test the hypothesis that V is associated with a readily exchangeable phase (phyllosilicate or other). Future work could compare the leachability of V from unground and ground coke particles to determine whether exposing more of the internal concentric inorganic layers to a leaching solution results in more V release. It would be necessary to normalize the data to account for the obvious increase in surface area induced by pulverization and fragmentation.

Another potential element of concern, Mo, exhibited low solid-phase concentrations (13 ± 4 mg kg^{-1}) but elevated aqueous-phase concentrations (up to 2.2 mg L^{-1}) comparable to those of V. This release represents a considerably larger leachability than V or Ni. Delineating solid-phase speciation and potential mechanisms of Mo release and mobility should be an objective of future research.

The current research examined coke deposit pore water aqueous geochemical data collected on one date only. Therefore, data reflect instantaneous geochemical depth profiles only. It is hypothesized that the geochemistry of coke deposits may be transient. For example, stable

isotopes of water depth profiles at some sampling sites suggested the presence of more complex, dynamic mixing conditions. Future field-based geochemical studies of coke deposit pore water should consider temporal variation by sampling at multiple times throughout the year. Special attention should be given to the effect of spring freshet and late-summer evaporative conditions on near-surface redox geochemical conditions and trace element concentrations.

REFERENCES

AER, 2015. ST98-2015: Alberta's Energy Reserves 2014 and Supply/Demand Outlook 2015–2024. Calgary: Alberta Energy Regulator.

Aide, M., 2005. Geochemical Assessment of Iron and Vanadium relationships in Oxic Soil Environments. Soil & Sediment Contamination, 14, 403-416. doi:10.1080/15320380500180382

Angel, R., Finger, L.W., 1988. Polymorphism of Nickel Sulfate Hexahydrate. Acta Crystallographia, C44, 1869-1873.

Anthony, E.J., 1995. Fluidized bed combustion of alternate solid fuels; status, success and problem of the technology. Progressing Energy and Combustion Science, 21, 239-268.

Asaoka, S., Nakata, S., Shiroto, Y., Takeuchi, C., 1983. Asphaltene Cracking in Catalytic Hydrotreating of Heavy Oils - Study of Changes in Asphaltene Structure during Catalytic Hydroprocessing. Industrial Engineering Chemistry Process Design and Development, 22, 242-248.

Baer, T.J., 2014. An evaluation of the use of natural stable isotopes of water to track water movement through oil sands mine closure landforms. M.Sc. Thesis, Department of Civil and Geological Engineering, University of Saskatchewan. Saskatoon, Saskatchewan.

Baes, C.F., Mesmer, R.E., 1976. The hydrolysis of cations. John Wiley & Sons.

Baker, L.F., Ciborowski, J.J.H., MacKinnon, M.D., 2012. Petroleum coke and soft tailings sediment in constructed wetlands may contribute to the uptake of trace metals by algae and aquatic invertebrates. Science of the Total Environment, 414, 177-186. doi:10.1016/j.scitotenv.2011.10.011

Balan, E., De Villiers, J.P.R., Eeckhout, S.G., Glatzel, P., Toplis, M.J., Fritsch, E., Allard, T., Galoisy, L., Calas, G., 2006. The oxidation state of vanadium in titanomagnetite from layered basic intrusions. American Mineralogist, 91, 953-956. doi:10.2138/am.2006.2192

Baran, E.J., 2001. Review: Spectroscopic studies of oxovanadium coordination compounds. Journal of Coordination Chemistry, 54, 215-238. doi:10.1080/00958970108022636

Bausell, R.A., Caspers, J., Hastings, K.E., Potts, J.D., Van Driesen, R.P., 1992. Demetallization/Desulfurization of High Metal Content Petroleum Feedstocks. In McKetta, J.J. (Ed.), Petroleum Processing Handbook. Marcel Dekker Inc. New York, pp. 677-696.

Bejarano, C., Jia, C.Q., Chung, K.H., 2003. Mechanistic Study of the Carbothermal Reduction of Sulfur Dioxide with Oil Sand Fluid Coke. Industrial and Engineering Chemical Research, 42, 3731-3739. doi:10.1021/ie0206711

Blackmore, D.P.T., Ellis, J., Riley, P.J., 1996. Treatment of a vanadium-containing effluent by adsorption/coprecipitation with iron oxyhydroxide. Water Research, 30(10), 2512-2516.

Blaser, D.E., 1992. Coking, Petroleum (Fluid). In McKetta, J.J. (Ed.), Petroleum Processing Handbook. Marcel Dekker Inc. New York, pp. 253-280.

Bohic, S., Murphy, K., Paulus, W., Cloetens, P., Salomé, M., Susini, J., Double, K., 2008. Intracellular Chemical Imaging of the Developmental Phases of Human Neuromelanin Using Synchrotron X-ray Microspectroscopy. Analytical Chemistry, 80(24), 9557-9566. doi:10.1021/ac801817k

Booz-Allen & Hamilton Inc., 1982. Bitumen and Very Heavy Oil Upgrading. In Schumacher, M. (Ed.), Heavy Oil and Tar Sands Recovery and Upgrading. Noyes Data Corporation, Park Ridge, New Jersey, pp. 374-503.

Brunauer, S., Emmett, P.H., Teller, E., 1938. Adsorption of Gases in Multimolecular Layers. Journal of the American Chemical Society, 60, 309-319.

Bunău, O., Joly, Y., 2009. Self-consistent aspects of x-ray absorption calculations. Journal of Physics: Condensed Matter, 21, 345501 (11pp). doi:10.1088/0953-8984/21/34/345501

Cantley, L.C., Josephson, L., Warner, R., Yanagisawa, M., Lechene, C., Guidotti, G., 1977. Vanadate Is a Potent (Na,K)-ATPase Inhibitor Found in ATP Derived from Muscle. Journal of Biological Chemistry, 21, 7421-7423.

Caumette, G., Lienemann, C.-P., Merdrignac, I., Bouyssiere, B., Lobinski, R., 2009. Element speciation analysis of petroleum and related materials. Journal of Analytical Atomic Spectrometry, 24, 263-276. doi:10.1039/b817888g

Chaurand, P., Rose, J., Briois, V., Salome, M., Proux, O., Nassif, V., Olivi, L., Susini, J., Hazemann, J-L., Bottero, J-Y., 2007. New Methodological Approach for the Vanadium K-Edge X-ray Absorption Near-Edge Structure Interpretation: Application to the

Speciation of Vanadium in Oxide Phases from Steel Slag. Journal of Physical Chemistry B, 111, 5101-5110. doi:10.1021/jp063186i

Chung, K.H., Janke, L.C.G., Dureau, R., Furimsky, E., 1996. Leachability of cokes from Syncrude stockpiles. Environmental Science and Engineering, 9(1), 50-53.

Dechaine, G.P., Gray, M.R., 2010. Chemistry and Association of Vanadium Compounds in Heavy Oil and Bitumen, and Implications for Their Selective Removal. Energy & Fuels, 24, 2795-2808. doi:10.1021/ef100173j

Dunlop, D.D., Griffin, L.I., Moser, J.F., 1958. Particle Size Control in Fluid Coking. Chemical Engineering Progress, 54(8), 39-43.

El Béze, L., Rose, J., Mouillet, V., Farcas, F., Masion, A., Chaurand, P., Bottero, J.-Y., 2012. Location and evolution of the speciation of vanadium in bitumen and model of reclaimed bituminous mixes during ageing: Can vanadium serve as a tracer of the aged and fresh parts of the reclaimed asphalt pavement mixture? Fuel, 102, 423-430. doi:10.1016/j.fuel.2012.06.080

Faure, G., 1998. Principles and Application of Geochemistry (2nd ed.). Prentice Hall, New Jersey.

Fedorak, P.M., Coy, D.L., 2006. Oil sands cokes affect microbial activities. Fuel, 85, 1642-1651. doi:10.1016/j.fuel.2006.02.015

Filby, R.H., 1994. Origin and nature of trace element species in crude oils, bitumens and kerogens: implications for correlation and other geochemical studies. In Parnell, J. (Ed.), Geofluids: Origin, Migration and Evolution of Fluids in Sedimentary Basins. Geological Society Special Publication No. 78, pp. 203-219. doi:10.1144/GSL.SP.1994.078.01.15

Filby, R.H., Strong, D., 1991. Nickel (II) and vanadium (IV) complexes in Alberta oil-sand bitumens. Tar sand and oil upgrading technology. AlChE symposium series, 282.

Fish, R.H., Reynolds, J.G., Gallegos, E.J., 1986. Molecular characterization of nickel and vanadium non-porphyrin compounds found in heavy crude petroleums and bitumens. 191st ACS Meeting, Division of Geochemistry. New York.

Freeze, R.A., Cherry, F.A., 1979. Groundwater. Prentice-Hall, Englewood Cliffs, NJ.

Furimsky, E., 1998. Gasification of oil sand coke: Review. Fuel Processing Technology, 56, 263-290.

Gamal El-Din, M., Fu, H., Wang, N., Chelme-Ayala, P., Perez-Estrada, L.A., Drzewicz, P., Martin, J.W., Zubot, W., Smith, D.W., 2011. Naphthenic acids speciation and removal during petroleum-coke adsorption and ozonation of oil sands process-affected water. Science of the Total Environment, 409, 5119-5125. doi:10.1016/j.scitotenv.2011.08.033

George, G.N., Gorbaty, M.L., 1989. Sulfur K-Edge X-ray Absorption Spectroscopy of Petroleum Asphaltenes and Model Compounds. Journal of the American Chemical Society, 111(9), 3182-3186.

Gražulis, S., Chateigner, D., Downs, R.T., Yokochi, A.F.T., Quiros, M., Lutterotti, L., Manakova, E., Butkus, J., Moeck, P., Le Bail, A., 2009. Crystallography Open Database - an open-access collection of crystal structures. Journal of Applied Crystallography, 42, 726-729. doi:10.1107/S0021889809016690

Har, S., 1981. Characterization of Oil Sands Fluid Coke. M.Sc. Thesis, University of Alberta, Edmonton, AB.

Hon, P.-K., Belford, R.L., Pfluger, C.E., 1965. Bis(1-Phenyl-1,3-Butanedionato) Vanadyl. I. Molecular and Crystal Structure of the cis Form. Journal of Chemical Physics, 43(4), 1323-1333.

Hummel, W., Curti, E., 2003. Nickel Aqueous Speciation and Solubility at Ambient Conditions: A Thermodynamic Elegy. Monatshefte fur Chemie, 134, 941-973. doi:10.1007/s00706-003-0010-8

Isaure, M.-P., Laboudigue, A., Manceau, A., Sarret, G., Tiffreau, C., Trocellier, P., Lamble, G., Hazemann, J.-L., Chateigner, D., 2002. Quantitative Zn speciation in a contaminated dredged sediment by μ-PIXE, μ-SXRF, EXAFS spectroscopy and principal component analysis. Geochimica et Cosmochimica Acta, 66(9), 1549-1567.

Jack, T.R., Sullivan, E.A., Zajic, J.E., 1979a. Comparison of the structure and composition of cokes from the thermal cracking of Athabasca Oil Sands bitumen. Fuel, 58(8), 585-588.

Jack, T.R., Sullivan, E.A., Zajic, J.E., 1979b. Leaching of vanadium and other metals from Athabasca Oil Sands coke and coke ash. Fuel, 58(8), 589-594.

Jacobs, F.S., Bachelor, F.W., Filby, R.H., 1984. Trace metals in Alberta oil sand bitumen components. Caractérisation des huiles lourdes et des résidus pétroliers: symposium international. Editions TECHNIP, Lyon, pp. 173-177.

Jang, H., Etsell, T.H., 2006. Mineralogy and phase transition of oil sands coke ash. Fuel, 85, 1526-1534. doi:10.1016/j.fuel.2005.12.013

Jensen-Fontaine, M., 2012. Vanadium Speciation in Samples Relevant to the Athabasca Oil Sands Region. M.Sc. Thesis, University of Alberta, Edmonton, AB.

Jensen-Fontaine, M., Norwood, W.P., Brown, M., Dixon, D.G., Le, X.C., 2014. Uptake and Speciation of Vanadium in the Benthic Invertebrate Hyalella azteca. Environmental Science and Technology, 48, 731-738. doi:10.1021/es403252k

Kaminsky, H.A.W., Etsell, T.H., Ivey, D.G., Omotoso, O., 2008. Characterization of heavy minerals in the Athabasca oil sands. Minerals Engineering, 21, 264-271. doi:10.1016/j.mineng.2007.09.011

Kasperski, K.L., Mikula, R.J., 2011. Waste Streams of Mined Oil Sands: Characteristics and Remediation. Elements, 7, 387-392. doi:10.2113/gselements.7.6.387

Kessler, S., Hendry, M.J., 2006. Geochemistry and Leaching of Coke from Syncrude and Suncor Sites. University of Saskatchewan, Geological Sciences, Saskatoon.

Lahmira, B., Barbour, L., Huang, M., 2013. Numerical Modeling of Gas Flow in the Suncor Coke Stockpile Covers. Vadose Zone Journal, 13(1), 1-12. doi:10.2136/vzj2013.07.0119

LECO Corporation, 2008. CS230 Carbon/Sulfur Determinator Specification Sheet. St. Joseph, MI. Retrieved from http://www.usbioecuador.com/descargas/leco-inorganica/CS230-ht.pdf

Lewan, M.D., 1984. Factors controlling the proportionality of vanadium to nickel in crude oils. Geochimica et Cosmochimica Acta, 48, 2231-2238.

Lewan, M., Maynard, J.B., 1982. Factors controlling enrichment of vanadium and nickel in the bitumen of organic sedimentary rocks. Geochimica et Cosmochimica Acta, 46, 2547-2560.

Li, X.S., Glasauer, S., Le, X.C., 2007. Speciation of vanadium in oilsand coke and bacterial culture by high performance liquid chromatography inductively coupled plasma mass spectrometry. Analytica Chimica Acta, 602, 17-22. doi:10.1016/j.aca.2007.09.004

Light, T.S., 1972. Standard Solution for Redox Potential Measurements. Analytical Chemistry, 44(6), 1038-1039.

Lu, L., Sahajwalla, V., Kong, C., Harris, D., 2001. Quantitative X-ray diffraction analysis and its application to various coals. Carbon, 39, 1821-1833. doi:10.1016/S0008-6223(00)00318-3

Lytle, F.W., 1983. Cold Lake Asphaltene V and Ni XAS spectra. International X-ray Absorption Society XAFS Database. Retrieved from http://ixs.iit.edu/database/data/Farrel_Lytle_data/RAW/

Maclean, A.L., Foran, G.J., Kennedy, B.J., Turner, P., Hambley, T.W., 1996. Structural Characterization of Nickel(II) Tetraphenylporphyrin. Australian Journal of Chemistry, 49, 1273-1278.

Manceau, A., Marcus, M.A., Tamura, N., 2002. Quantitative Speciation of Heavy Metals in Soils and Sediments by Synchrotron X-ray Techniques. Reviews in Mineralogy and Geochemistry, 49(1), 341-428.

Matsen, J.M., 1996. Scale-up of fluidized bed processes: Principle and practice. Powder Technology, 88(3), 237-244.

Maylotte, D.H., Wong, J., Peters, R., Lytle, F.W., Greegor, R.B., 1981. X-ray Absorption Spectroscopic Investigation of Trace Vanadium Sites in Coal. Science, 214(4520), 554-556.

Meyer, E.F., 1972. The Crystal and Molecular Structure of Nickel(II)octaethylporphyrin. Acta Crystallographia, B28, 2162-2167.

Miller, J.T., Fisher, R.B., 1999. Structural determination by XAFS spectroscopy of non-porphyrin nickel and vanadium in Maya residuum, hydrocracked residuum, and toluene-insoluble solid. Energy & Fuels, 13, 719-727. doi:10.1021/ef9802328

Millson, M.F., Montgomery, D.S., Brown, S.R., 1966. An investigation of the vanadyl porphyrin complexes of the Athabasca oil sands. Geochimica et Cosmochimica Acta, 30, 207-221.

Miyoshi, Y., Takahashi, K., Fujimoto, T., Yoshikawa, H., Matsushita, M.M., Ouchi, Y., Kepenekian, M., Robert, V., Donzello, M.P., Ercolani, C., Awaga, K., 2012. Crystal Structure, Spin Polarization, Solid-State Electrochemistry, and High n-Type Carrier Mobility of a Paramagnetic Semiconductor: Vanadyl Tetrakis(thiadiazole)porphyrazine. Inorganic Chemistry, 51, 456-462. doi:10.1021/ic201880g

Molinaro, F.S., Ibers, J.A., 1976. Crystal and Molecular Structure of 2,3,7,8,12,13,17,18-Octaethylporphinatooxovanadium(IV). Inorganic Chemistry, 15(9), 2278-2283.

Nakata, C., Qualizza, C., MacKinnon, M., Renault, S., 2011. Growth and Physiological Responses of Triticum aestivum and Deschampsia caespitosa Exposed to petroleum Coke. Water, Air, Soil, and Pollution, 216, 59-72. doi:10.1007/s11270-010-0514-x

Nordstrom, D.K., 1977. Thermochemical redox equilibria of ZoBell's solution. Geochimica et Cosmochimica Acta, 41, 1835-1841.

Norwest Corporation, 2003. Oil sands coke properties and summary of relative experience for FT coke capping. Report submitted to Suncor Energy Inc.

Parkhurst, D.L., Appelo, C.A.J., 2013. Description of Input and Examples for PHREEQC - A Computer Program for Speciation, Batch-Reaction, One-Dimensional Transport, and Inverse Geochemical Calculations, in: U.S. Geological Survey Techniques and Methods, Book 6. USGS, p. 497.

Pearson, C.D., Green, J.B., 1993. Vanadium and Nickel Complexes in Petroleum Resid Acid, Base, and Neutral Fractions. Energy & Fuels, 7, 338-346.

Pollack, S.S., Alexander, L.E., 1960. X-Ray Analysis of Electrode Binder Pitches and Their Cokes. Journal of Chemical and Engineering Data, 5(1), 88-93.

Pomerantz, A.E., Bake, K.D., Craddock, P.R., Kurzenhauser, K.W., Kodalen, B.G., Mitra-Kirtley, S., Bolin, T.B., 2014. Sulfur speciation in kerogen and bitumen from gas and oil shales. Organic Geochemistry, 68, 5-12. doi:10.1016/j.orggeochem.2013.12.011

Pourrezaei, P., Alpatova, A., Chelme-Ayala, P., Perez-Estrada, L.A., Jensen-Fontaine, M., Le, X.C., Gamal el-Din, M., 2014. Impact of petroleum coke characteristics on the adsorption of the organic fractions from oil sands process-affected water. International Journal of Environmental Science and Technology, 11, 2037-2050. doi:10.1007/s13762-013-0406-x

Pourrezaei, P., Alpatova, A., Khosravi, K., Drzewicz, P., Chen, Y., Chelme-Ayala, P., & Gamal El-Din, G. (2014). Removal of organic compounds and trace metals from oil sands process-affected water using zero valent iron enhanced by petroleum coke. Journal of Environmental Management, 139, 50-58. doi:10.1016/j.jenvman.2014.03.001

Puttaswamy, N., Liber, K., 2011. Identifying the causes of oil sands coke leachate toxicity to aquatic invertebrates. Environmental Toxicology and Chemistry, 30(11), 2576-2585. doi:10.1002/etc.653

Puttaswamy, N., Liber, K., 2012. Influence of inorganic anions on metals release from oil sands coke and on toxicity of nickel and vanadium to Ceriodaphnia dubia. Chemosphere, 86, 521-529. doi:10.1016/j.chemosphere.2011.10.018

Puttaswamy, N., Turcotte, D., Liber, K., 2010. Variation in toxicity response of Ceriodaphnia dubia to Athabasca oil sands coke leachates. Chemosphere, 80, 489-497. doi:10.1016/j.chemosphere.2010.04.071

Rambabu, N., Azargohar, R., Dalai, A.K., Adjaye, J., 2013. Evaluation and comparison of enrichment efficiency of physical/chemical activations and functionalized activated carbons derived from fluid petroleum coke for environmental applications. Fuel processing Technology, 106, 501-510. doi:10.1016/j.fuproc.2012.09.019

Ravel, B., Newville, M., 2005. ATHENA, ARTEMIS, HEPHAESTUS: data analysis for X-ray absorption spectroscopy using IFEFFIT. Journal of Synchrotron Radiation, 12, 537-541. doi:10.1107/S0909049505012719

Reynolds, J.G., Gallegos, E.J., Fish, R.H., Komlenic, J.J., 1987. Characterization of the Binding Sites of Vanadium Compounds in Heavy Crude Petroleum Extracts by Electron Paramagnetic Resonance Spectroscopy. Energy & Fuels, 64(1), 36-44.

Saraceno, A.J., Fanale, D.T., Coggeshall, N.D., 1961. An Electron Paramagnetic Resonance Investigation of Vanadium in Petroleum Oils. Analytical Chemistry, 33(4), 500-505.

Scott, A., 2011. A review of environmentally-relevant studies of the byproduct coked produced by Syncrude Canada Ltd.

Tanaka, R., Sato, E., Hunt, J.E., Winans, R.E., Sato, S., Takanohashi, T., 2004. Characterization of Asphaltene Aggregates Using X-ray Diffraction and Small-Angle X-ray Scattering. Energy & Fuels, 18, 1118-1125. doi:10.1021/ef034082z

Tanaka, T., Yamashita, H., Tsuchitani, R., Funabiki, T., Yoshida, S., 1988. X-ray Absorption (EXAFS/XANES) Study of Supported Vanadium Oxide Catalysts: Structure of Surface Vanadium Oxide Species on Silica and y-Alumina at a Low Level of Vanadium Loading. Journal of the Chemical Society, 84(9), 2987-2999.

Toby, B.H., Von Dreele, R.B., 2013. GSAS-II: the genesis of a modern open-source all-purpose crystallography software package. Journal of Applied Crystallography, 46(2), 544-549. doi:10.1107/S0021889813003531

Tooulakou, D., Filby, R.H., 1988. Seperation of vanadium and nickel complexes from the Athabasca oil sands asphaltenes. In T. Yen, & J. Moldowan, Geochemical Biomarkers (pp. 221-240). Harwood Academic Publishers.

VanEtten, R.L., Waymack, P.P., Rehkop, D.M., 1974. Transition Metal Ion Inhibition of Enzyme-Catalyzed Phosphate Ester Displacement Reactions. Journal of the American Chemical Society, 96(21), 6782-6785.

Vidano, R., Fischbach, D.B., 1978. New Lines in the Raman Spectra of Carbons and Graphite. Journal of The American Ceramic Society, 61, 13-17.

Wassenaar, L.I., Hendry, M.J., Chostner, V.L., Lis, G.P., 2008. High Resolution Pore Water δ2H and δ18O Measurements by H2O(liquid)-H2O(vapor) Equilibration Laser Spectroscopy. Environmental Science and Technology, 42, 9262-9267. doi:10.1021/es802065s

Wehrli, B., Stumm, W. 1989. Vanadyl in natural waters: Adsorption and hydrolysis promote oxygenation. Geochimica et Cosmochimica Acta, 53, 69-77.

Wiehe, I.A., Liang, K.S., 1996. Asphaltenes, resins, and other petroleum macromolecules. Fluid Phase Equilibria, 117, 201-210.

Wong, J., Lytle, F.W., Messmer, R.P., Maylotte, D.H., 1984. K-edge absorption spectra of selected vanadium compounds. Physical Review B, 30(10), 5596-5610.

Yen, T.F., Erdman, J.G., Pollack, S.S., 1961. Investigation of the Structure of Petroleum Asphaltenes by X-Ray Diffraction. Analytical Chemistry, 33(11), 1578-1594.

Zajic, J.E., Jack, T.R., Sullivan, E.A., Woodfield, G., 1977. Metals, microbes and bituminous sands. Chemical and microbially-assisted leaching of Athabasca oil sands cokes. Report prepared for Alberta Oil Sands Technology and Research Authority (AOSTRA), Agreement #20.

Zeng, T., Arnold, W.A., Toner, B.M., 2013. Microscale Characterization of Sulfur Speciation in Lake Sediments. Environmental Science and Technology, 47, 1287-1296. doi:10.1021/es303914q

Zhang, Y., Shotyk, W., Zaccone, C., Noernberg, T., Pelletier, R., Bicalho, B., Froese, D.G., Davies, L., Martin, J.W., 2016. Airborne Petcoke Dust is a Major Source of Polycyclic Aromatic Hydrocarbons in the Athabasca Oil Sands Region. Environmental Science and Technology, 50, 1711-1720. doi:10.1021/acs.est.5b05092

Zhao, S., Kotlyar, L.S., Woods, J.R., Sparks, B.D., Gao, J., Kung, J., Chung, K.H., 2002. A benchmark assessment of residues: comparison of Athabasca bitumen with conventional and heavy crudes. Fuel, 81, 737-746.

ZoBell, C.E., 1946. Studies on redox potential of marine sediments. Bulletin of the American Association of Petroleum Geologists, 30(4), 477-513.

Zubot, W.A., 2010. Removal of Naphthenic Acids from Oil Sands Process Water using Petroleum Coke. M.Sc. Eng. Thesis, Department of Civil and Environmental Engineering, University of Alberta. Edmonton, Alberta.

Zubot, W.A., MacKinnon, M.D., Chelme-Ayala, P., Smith, D.W., Gamal El-Din, M., 2012. Petroleum coke adsorption as a water management option for oil sands process-affected water. Science of the Total Environment, 427-428, 364-372. doi:10.1016/j.scitotenv.2012.04.024

APPENDIX A: COKE BULK ELEMENTAL ANALYSES

Table A-1. Bulk elemental analysis of coke samples. Mean signifies that the average of triplicates is reported. All values reported in mg kg^{-1}. Methods of analysis are also reported below each element; LECO 230 total carbon & sulfur analysis (LECO), lithium borate fusion (LBF), aqua region digestion (AQ), inductively coupled plasma optical emission spectrometry (OES), inductively coupled plasma mass spectrometry (MS).

Location ID	C LECO	S LECO	Si LBF OES	Al LBF OES	Fe LBF OES	Ti LBF OES	V LBF MS
A000	845800	67100	12997	8788	7625	2578	1284
A200	813900	72200	8836	6247	5736	1798	1287
A600	870000	70000	11688	7941	6926	2218	1411
AB000	821500	70100	9912	6882	5387	1858	1301
AB200	848800	71200	10145	6882	6296	1858	1460
AB450	884700	68400	7481	5611	4197	1259	1280
AB700	845300	68500	6592	4923	3498	1019	1132
AM200	840300	70800	9257	6723	4897	1619	1178
AM350	837600	69600	10566	8100	6506	1679	1313
AM650mean	839000	72633	7932	5435	4967	1279	1312
AX200	860000	70800	7481	5294	4267	1199	1272
AX350	857700	68000	5423	4235	3148	959	1096
AX550	828900	66100	6358	4923	3848	1079	1063
B200	833900	69800	10426	7358	6086	1739	1181
B350	856800	72700	6966	4976	4267	1199	1087
B550	824700	75600	7714	5611	4897	1439	1354
BM000	801800	70300	11221	7358	6576	2038	1352
CX050mean	809733	68167	7714	5647	4734	1419	1273
CX300	823700	72000	12670	4870	3708	899	1336
CX500	872600	63700	7527	4659	3568	899	1095
D100	857500	74700	7714	5082	3778	1019	1475
D450mean	811900	69367	12109	7341	4734	1279	1420
DM050	854000	72200	7340	5188	3848	1079	1470
DM250	851100	68600	7668	5241	3638	1019	1249
DM550	842900	70200	7294	4817	3708	959	1339
DM950	893100	69600	8836	5982	4687	1259	1347
DX050	808100	70700	21179	6617	3918	1019	1406
DX350	845400	64500	6873	4712	3848	1079	1173

Table A-1. continued

Location ID	Ca LBF OES	K LBF OES	Na LBF OES	Mg LBF OES	Ni LBF MS	P LBF OES	Mn LBF OES
A000	1287	1162	519.4	723.9	179.0	261.9	232.4
A200	858	830	371.0	482.6	227.0	174.6	154.9
A600	2216	913	667.8	723.9	349.0	261.9	154.9
AB000	786	747	296.8	482.6	457.0	174.6	154.9
AB200	1072	747	371.0	542.9	433.0	174.6	154.9

AB450	858	664	445.2	422.3	288.0	87.3	77.5
AB700	715	581	445.2	301.6	194.0	43.7	77.5
AM200	1072	830	445.2	482.6	140.0	131.0	154.9
AM350	1072	830	519.4	542.9	217.0	218.3	154.9
AM650mean	1191	664	667.8	422.3	194.0	87.3	154.9
AX200	929	581	445.2	361.9	213.0	87.3	77.5
AX350	858	498	445.2	361.9	177.0	87.3	77.5
AX550	858	581	445.2	361.9	165.0	131.0	77.5
B200	1716	913	445.2	542.9	209.0	174.6	154.9
B350	786	747	371.0	422.3	136.0	131.0	77.5
B550	858	664	445.2	422.3	181.0	131.0	154.9
BM000	1001	996	445.2	603.2	224.0	174.6	232.4
CX050mean	1025	747	371.0	422.3	190.3	116.4	129.1
CX300	929	664	371.0	361.9	227.0	174.6	77.5
CX500	786	498	519.4	301.6	192.0	43.7	0.0
D100	1072	498	519.4	422.3	283.0	87.3	77.5
D450mean	1263	996	717.2	563.0	235.0	160.1	77.5
DM050	1072	581	445.2	422.3	263.0	87.3	77.5
DM250	1072	581	519.4	361.9	140.0	87.3	77.5
DM550	1215	664	445.2	361.9	164.0	43.7	77.5
DM950	1072	664	593.6	422.3	193.0	131.0	77.5
DX050	1573	1079	519.4	663.5	244.0	87.3	0.0
DX350	1001	581	445.2	361.9	155.0	87.3	77.5

Table A-1. continued

Location ID	Zr LBF MS	Sr LBF MS	Ba LBF MS	Ce LBF MS	Cu AQ MS	La LBF MS	Mo AQ MS
A000	155.0	65.1	73.0	45.2	24.7	20.4	18.4
A200	89.9	48.7	59.0	32.5	25.4	16.1	11.8
A600	147.2	81.4	72.0	40.6	25.6	21.2	22.4
AB000	78.6	39.5	38.0	36.9	25.4	16.9	10.1
AB200	96.4	52.6	61.0	33.0	11.8	18.1	15.9
AB450	47.7	46.2	57.0	25.6	21.3	13.0	15.8
AB700	42.4	31.3	36.0	21.5	11.4	12.6	14.6
AM200	75.5	48.0	59.0	31.6	24.3	13.5	19.0
AM350	87.4	67.9	63.0	35.5	8.5	17.1	15.4
AM650mean	68.9	47.9	50.7	24.0	9.7	12.3	10.0
AX200	53.5	42.2	48.0	24.4	27.9	11.5	19.5
AX350	43.2	39.8	41.0	19.9	7.1	12.9	13.5
AX550	42.7	60.6	45.0	22.6	13.7	11.8	11.8
B200	85.5	55.0	73.0	30.5	16.8	15.6	23.2
B350	54.8	53.4	51.0	22.5	10.2	11.4	7.6
B550	60.1	52.1	47.0	27.0	28.1	13.6	9.3
BM000	108.3	42.2	54.0	33.9	10.6	15.9	11.3
CX050mean	60.4	35.2	40.0	25.8	14.9	12.8	11.3
CX300	44.0	38.0	37.0	17.9	12.1	9.5	9.6
CX500	43.6	32.5	38.0	18.0	12.4	11.5	11.7
D100	50.2	43.6	35.0	19.3	15.7	10.7	9.8
D450mean	63.4	70.5	58.7	25.7	14.8	12.9	13.1

DM050	50.8	52.0	43.0	24.0	18.5	11.4	13.7
DM250	53.1	64.6	45.0	23.4	13.1	10.8	12.9
DM550	52.6	59.0	44.0	19.8	16.5	8.9	10.7
DM950	60.7	57.1	42.0	24.7	8.9	11.5	11.8
DX050	58.9	60.3	51.0	23.0	9.3	10.2	7.6
DX350	49.1	40.7	36.0	18.6	33.2	9.0	9.6

Table A-1. continued

Location ID	Zn AQ MS	Nd LBF MS	Co LBF MS	Cr LBF MS	Y LBF MS	Pb AQ MS
A000	18.4	13.0	17.7	11.2	13.7	13.2
A200	11.8	24.0	13.4	9.8	10.3	8.8
A600	22.4	22.0	17.9	11.7	13.7	12.5
AB000	10.1	9.0	15.3	10.1	10.3	9.8
AB200	15.9	12.0	14.8	10.6	10.3	9.1
AB450	15.8	16.0	10.3	9.1	10.3	7.0
AB700	14.6	10.0	8.1	8.2	0.0	6.2
AM200	19.0	18.0	11.7	8.5	6.8	8.3
AM350	15.4	12.0	16.0	9.8	13.7	9.8
AM650mean	10.0	9.7	10.1	8.4	8.6	7.4
AX200	19.5	19.0	9.5	8.6	10.3	5.8
AX350	13.5	6.0	9.3	6.5	0.0	5.3
AX550	11.8	11.0	8.9	9.0	0.0	6.5
B200	23.2	15.0	12.4	9.6	10.3	9.6
B350	7.6	9.0	10.4	7.8	10.3	6.7
B550	9.3	20.0	11.4	8.7	6.8	7.0
BM000	11.3	12.0	14.1	10.4	10.3	11.8
CX050mean	11.3	11.3	10.5	8.4	13.7	7.8
CX300	9.6	8.0	7.0	6.8	13.7	4.8
CX500	11.7	9.0	7.4	7.0	13.7	5.4
D100	9.8	12.0	8.1	8.3	0.0	6.4
D450mean	13.1	12.3	11.5	9.7	9.1	8.0
DM050	13.7	13.0	9.6	10.0	13.7	6.4
DM250	12.9	11.0	9.5	9.5	10.3	6.5
DM550	10.7	10.0	8.7	9.6	10.3	6.7
DM950	11.8	9.0	9.7	11.1	6.8	7.3
DX050	7.6	8.0	9.5	7.2	10.3	7.2
DX350	9.6	19.0	9.7	7.8	0.0	6.6

APPENDIX B: COKE BULK ELEMENTAL ANALYSES PEARSON CORRELATION

Matrix of *R* and *p* for correlations of raw values (n = 28) (upper triangle, NT); matrix of R and p for correlations of centred logratio transformation of values (lower triangle, CLRT); light green ($p<0.05$).

	C	S	Si	Al	Fe	Ti	V	Ca	K	Na	Mg	Ni	P	Mn	Zr	Sr	Ba	Ce	Cu	La	Mo	Zn	Nd	Co	Cr	Y	Pb
C	NT	-0.185	-0.414	-0.252	-0.190	-0.180	-0.127	0.003	-0.467	0.226	-0.264	0.000	-0.214	-0.309	-0.108	0.046	-0.051	-0.156	0.008	-0.062	0.295	0.001	-0.152	0.094	-0.087	-0.210	0.070
	CLRT	0.3460	0.0287	0.1950	0.3320	0.3600	0.5180	0.9880	0.0122	0.2490	0.1740	0.9980	0.2750	0.1090	0.5840	0.8180	0.7960	0.4270	0.9670	0.7540	0.1280	0.9960	0.4390	0.6350	0.6610	0.2850	0.7240
S	0.961		0.116	0.053	0.107	0.064	0.556	0.060	0.064	-0.067	0.136	0.208	0.111	0.229	0.042	0.090	0.072	0.068	0.002	0.020	-0.162	0.161	0.053	0.083	0.094	-0.001	0.188
	0.0000		0.5580	0.7890	0.5880	0.7460	0.0021	0.7640	0.7450	0.7340	0.4890	0.2870	0.5720	0.2420	0.8320	0.6490	0.7160	0.7320	0.9930	0.9190	0.4100	0.4140	0.7900	0.6740	0.6350	0.9940	0.3380
Si	0.010	0.084		0.605	0.370	0.312	0.450	0.541	0.774	0.220	0.738	0.263	0.424	0.063	0.416	0.383	0.403	0.351	-0.108	0.241	0.015	-0.081	0.330	0.122	0.409	0.408	0.099
	0.9580	0.6710		0.0007	0.0526	0.1060	0.0164	0.0030	0.0000	0.2600	0.0000	0.1760	0.0244	0.7500	0.0278	0.0445	0.0336	0.0671	0.5840	0.2170	0.9410	0.6830	0.0863	0.5350	0.0305	0.0312	0.6150
Al	-0.090	-0.070	0.614		0.905	0.867	0.378	0.557	0.864	0.263	0.903	0.353	0.827	0.671	0.862	0.572	0.814	0.900	0.140	0.814	0.502	0.267	0.882	0.689	0.465	0.909	0.477
	0.6510	0.7230	0.0005		0.0000	0.0000	0.0476	0.0021	0.0000	0.1760	0.0000	0.0655	0.0000	0.0001	0.0000	0.0015	0.0000	0.0000	0.4770	0.0000	0.0065	0.1700	0.0000	0.0000	0.0126	0.0000	0.0102
Fe	-0.443	-0.413	-0.100	0.302		0.963	0.304	0.458	0.731	0.121	0.806	0.346	0.867	0.850	0.937	0.445	0.802	0.933	0.212	0.897	0.490	0.377	0.933	0.732	0.460	0.944	0.559
	0.0182	0.0288	0.6130	0.1180		0.0000	0.1160	0.0143	0.0000	0.5390	0.0000	0.0716	0.0000	0.0000	0.0000	0.0176	0.0000	0.0000	0.2790	0.0000	0.0082	0.0481	0.0000	0.0000	0.0138	0.0000	0.0020
Ti	-0.642	-0.633	-0.332	0.087	0.797		0.231	0.397	0.709	0.017	0.788	0.370	0.845	0.872	0.949	0.367	0.752	0.970	0.336	0.926	0.507	0.414	0.947	0.725	0.389	0.957	0.603
	0.0002	0.0003	0.0840	0.6600	0.0000		0.2370	0.0365	0.0000	0.9330	0.0000	0.0526	0.0000	0.0000	0.0000	0.0544	0.0000	0.0000	0.0809	0.0000	0.0059	0.0284	0.0000	0.0000	0.0408	0.0000	0.0007
V	0.832	0.890	0.253	-0.005	-0.446	-0.708		0.394	0.293	0.272	0.466	0.550	0.260	0.184	0.304	0.337	0.164	0.255	0.057	0.184	-0.029	0.136	0.276	0.461	0.349	0.282	0.182
	0.0000	0.0000	0.1940	0.9810	0.0173	0.0000		0.0379	0.1300	0.1620	0.0124	0.0024	0.1820	0.3480	0.1160	0.0791	0.4040	0.1900	0.7740	0.3480	0.8850	0.4910	0.1560	0.0135	0.0687	0.1460	0.3540
Ca	0.144	0.128	0.380	0.024	-0.385	-0.569	0.258		0.549	0.541	0.702	0.187	0.444	0.182	0.580	0.677	0.618	0.402	0.085	0.386	0.500	0.245	0.435	0.417	0.309	0.530	0.361
	0.4640	0.5160	0.0461	0.9020	0.0433	0.0016	0.1850		0.0025	0.0029	0.0000	0.3400	0.0180	0.3540	0.0012	0.0001	0.0005	0.0341	0.6690	0.0426	0.0068	0.2100	0.0208	0.0271	0.1100	0.0038	0.0590
K	-0.112	-0.032	0.694	0.641	0.148	0.024	-0.042	0.181		0.208	0.902	0.131	0.682	0.515	0.737	0.513	0.744	0.706	0.062	0.574	0.260	0.159	0.682	0.451	0.457	0.780	0.324
	0.5720	0.8710	0.0000	0.0002	0.4510	0.9050	0.8330	0.3560		0.2880	0.0000	0.5060	0.0001	0.0051	0.0000	0.0053	0.0000	0.0000	0.7530	0.0014	0.1810	0.4180	0.0001	0.0160	0.0146	0.0000	0.0922
Na	0.619	0.555	0.139	0.078	-0.430	-0.707	0.576	0.530	-0.021		0.308	-0.137	0.084	-0.081	0.207	0.563	0.283	0.046	-0.168	0.067	0.181	0.022	0.077	0.228	0.016	0.167	0.072
	0.0004	0.0022	0.4810	0.6930	0.0225	0.0000	0.0013	0.0037	0.9160		0.1110	0.4860	0.6700	0.6810	0.2900	0.0018	0.1440	0.8150	0.3920	0.7350	0.3570	0.9100	0.6990	0.2430	0.9350	0.3960	0.7160
Mg	-0.317	-0.238	0.645	0.489	0.078	0.044	-0.086	0.366	0.669	-0.024		0.362	0.768	0.545	0.856	0.623	0.782	0.797	0.109	0.726	0.366	0.234	0.807	0.575	0.417	0.861	0.457
	0.1010	0.2220	0.0002	0.0082	0.6930	0.8250	0.6640	0.0553	0.0001	0.9030		0.0581	0.0000	0.0027	0.0000	0.0004	0.0000	0.0000	0.5820	0.0000	0.0556	0.2300	0.0000	0.0014	0.0273	0.0000	0.0144
Ni	0.171	0.199	0.167	-0.056	-0.194	-0.203	0.408	-0.082	-0.298	-0.095	-0.008		0.340	0.186	0.319	0.040	0.135	0.407	0.122	0.489	0.142	0.046	0.447	0.393	0.225	0.342	0.408
	0.3850	0.3110	0.3950	0.7760	0.3220	0.3000	0.0313	0.6790	0.1240	0.6320	0.9680		0.0771	0.3430	0.0983	0.8390	0.4950	0.0315	0.5350	0.0084	0.4710	0.8170	0.0172	0.0386	0.2490	0.0745	0.0311
P	-0.600	-0.540	0.062	0.106	0.464	0.506	-0.539	-0.263	0.119	-0.530	0.292	-0.140		0.709	0.839	0.531	0.709	0.842	0.187	0.820	0.413	0.300	0.856	0.611	0.414	0.814	0.511
	0.0007	0.0031	0.7560	0.5930	0.0130	0.0060	0.0031	0.1760	0.5460	0.0037	0.1310	0.4790		0.0000	0.0000	0.0037	0.0000	0.0000	0.3410	0.0000	0.0291	0.1210	0.0000	0.0006	0.0286	0.0000	0.0054
Mn															0.778	0.180	0.576	0.813	0.262	0.757	0.365	0.353	0.784	0.605	0.225	0.808	0.430
															0.0000	0.3610	0.0013	0.0000	0.1790	0.0000	0.0563	0.0658	0.0000	0.0006	0.2500	0.0000	0.0224
Zr	-0.779	-0.769	-0.020	0.135	0.697	0.781	-0.701	-0.108	0.152	-0.494	0.343	-0.267	0.474			0.506	0.780	0.921	0.256	0.890	0.516	0.368	0.915	0.717	0.432	0.954	0.590
	0.0000	0.0000	0.9210	0.4930	0.0000	0.0000	0.0000	0.5860	0.4410	0.0075	0.0744	0.1690	0.0108			0.0060	0.0000	0.0000	0.1890	0.0000	0.0050	0.0541	0.0000	0.0000	0.0217	0.0000	0.0010
Sr	0.212	0.201	0.111	0.008	-0.395	-0.570	0.229	0.497	0.107	0.513	0.196	-0.282	-0.070		-0.282		0.654	0.457	0.014	0.382	0.316	0.206	0.508	0.594	0.272	0.485	0.314
	0.2800	0.3040	0.5740	0.9670	0.0374	0.0016	0.2400	0.0072	0.5880	0.0053	0.3180	0.1460	0.7230		0.1460		0.0002	0.0146	0.9450	0.0450	0.1020	0.2920	0.0058	0.0009	0.1620	0.0090	0.1040
Ba	-0.064	-0.093	-0.018	0.061	0.037	-0.086	-0.271	0.178	0.299	0.136	0.151	-0.487	-0.031		0.026	0.381		0.760	0.149	0.738	0.678	0.429	0.755	0.572	0.433	0.753	0.598
	0.7460	0.6370	0.9270	0.7590	0.8530	0.6640	0.1640	0.3640	0.1220	0.4890	0.4430	0.0086	0.8750		0.8970	0.0456		0.0000	0.4480	0.0000	0.0001	0.0226	0.0000	0.0015	0.0212	0.0000	0.0008
Ce	-0.523	-0.520	-0.270	0.249	0.568	0.827	-0.603	-0.614	0.025	-0.629	0.020	-0.140	0.380		0.596	-0.364	-0.054		0.310	0.935	0.535	0.380	0.966	0.752	0.433	0.939	0.624
	0.0043	0.0045	0.1650	0.2010	0.0016	0.0000	0.0007	0.0005	0.9000	0.0003	0.9210	0.4780	0.0463		0.0008	0.0569	0.7840		0.1080	0.0000	0.0033	0.0463	0.0000	0.0000	0.0214	0.0000	0.0004
Cu	0.050	0.030	-0.329	-0.531	-0.315	-0.042	0.003	-0.195	-0.347	-0.202	-0.499	-0.039	-0.219		-0.248	-0.237	-0.347	-0.156		0.205	0.278	0.798	0.294	0.226	0.006	0.227	0.399
	0.8010	0.8800	0.0876	0.0036	0.1030	0.8330	0.9890	0.3210	0.0705	0.3040	0.0069	0.8420	0.2620		0.2040	0.2240	0.0703	0.4280		0.2960	0.1520	0.0000	0.1290	0.2470	0.9740	0.2450	0.0357
La	-0.099	-0.150	-0.391	0.034	0.405	0.552	-0.320	-0.547	-0.267	-0.281	-0.182	0.178	0.169		0.286	-0.443	-0.008	0.633	-0.295		0.581	0.342	0.934	0.670	0.350	0.877	0.675
	0.6170	0.4460	0.0399	0.8650	0.0326	0.0023	0.0965	0.0026	0.1700	0.1480	0.3540	0.3650	0.3910		0.1400	0.0183	0.9670	0.0003	0.1280		0.0012	0.0746	0.0000	0.0001	0.0682	0.0000	0.0001
Mo	0.127	-0.021	-0.413	-0.192	-0.244	-0.120	-0.136	0.082	-0.441	0.129	-0.528	-0.099	-0.280		-0.197	-0.108	0.279	-0.018	0.095	0.228		0.438	0.473	0.452	0.210	0.461	0.535
	0.5190	0.9150	0.0288	0.3280	0.2120	0.5440	0.4910	0.6770	0.0188	0.5140	0.0039	0.6160	0.1500		0.3150	0.5830	0.1500	0.9270	0.6300	0.2440		0.0197	0.0111	0.0157	0.2820	0.0136	0.0034
Zn	-0.025	-0.027	-0.465	-0.585	-0.203	-0.072	-0.075	-0.173	-0.419	-0.074	-0.555	-0.237	-0.208		-0.232	-0.145	-0.049	-0.250	0.761	-0.303	0.190		0.381	0.340	0.063	0.319	0.702
	0.8980	0.8900	0.0126	0.0011	0.3000	0.7160	0.7050	0.3790	0.0264	0.7070	0.0022	0.2250	0.2880		0.2350	0.4620	0.8030	0.2000	0.0000	0.1170	0.3330		0.0452	0.0763	0.7500	0.0975	0.0000
Nd	-0.475	-0.489	-0.339	0.122	0.569	0.754	-0.548	-0.484	-0.001	-0.547	0.143	-0.106	0.414		0.608	-0.200	-0.035	0.780	-0.176	0.556	-0.218	-0.232		0.731	0.401	0.934	0.617
	0.0107	0.0082	0.0773	0.5350	0.0016	0.0000	0.0025	0.0091	0.9960	0.0026	0.4680	0.5920	0.0284		0.0006	0.3070	0.8580	0.0000	0.3690	0.0021	0.2650	0.2340		0.0000	0.0344	0.0000	0.0005
Co	0.562	0.514	-0.290	-0.079	-0.158	-0.285	0.554	-0.021	-0.271	0.361	-0.432	0.132	-0.448		-0.414	0.318	-0.243	-0.132	0.028	-0.103	0.092	-0.013	-0.190		0.338	0.760	0.521
	0.0018	0.0051	0.1340	0.6880	0.4210	0.1410	0.0022	0.9160	0.1640	0.0594	0.0218	0.5030	0.0169		0.0285	0.0994	0.2120	0.5030	0.8880	0.6040	0.6430	0.9460	0.3320		0.0787	0.0000	0.0045
Cr																										0.382	0.210
																										0.0448	0.2830
Y	-0.488	-0.506	-0.085	0.382	0.643	0.730	-0.502	-0.161	0.296	-0.345	0.343	-0.226	0.216		0.722	-0.229	-0.091	0.631	-0.273	0.313	-0.287	-0.323	0.669	-0.041			0.540
	0.0085	0.0060	0.6660	0.0447	0.0002	0.0000	0.0066	0.4120	0.1260	0.0722	0.0737	0.2470	0.2710		0.0000	0.2400	0.6440	0.0003	0.1610	0.1040	0.1380	0.0940	0.0001	0.8370			0.0030
Pb	-0.371	-0.370	-0.437	-0.420	-0.035	0.262	-0.452	-0.426	-0.375	-0.368	-0.350	0.108	0.032		0.146	-0.323	0.090	0.295	0.115	0.308	0.253	0.367	0.158	-0.213		-0.055	NT
	0.0518	0.0529	0.0200	0.0260	0.8590	0.1790	0.0156	0.0238	0.0494	0.0537	0.0681	0.5830	0.8730		0.4590	0.0934	0.6500	0.1270	0.5590	0.1110	0.1950	0.0547	0.4230	0.2760		0.7800	CLRT

APPENDIX C: COKE BULK ELEMENTAL ANALYSES, COMPARISON OF DEPOSITS

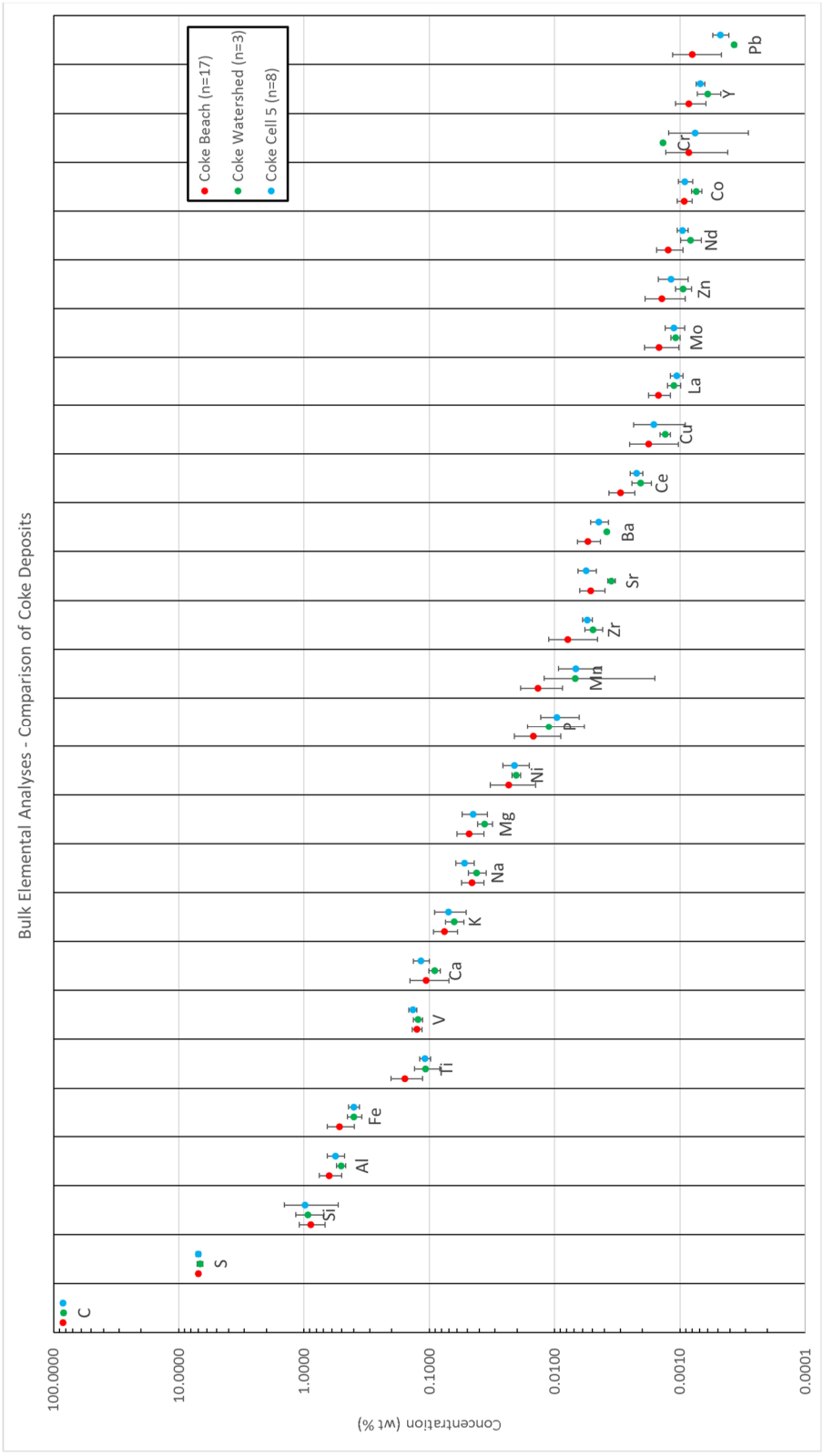

Table C-1. Summary statistics for bulk elemental analyses of coke deposits; Coke Beach (CB, n = 17), Coke Watershed (CW, n = 3), Coke Cell 5 (CC5, n = 8). All means and standard deviations in mg kg^{-1}.

	C	S	Si	Al	Fe	Ti	V
Coke ALL Mean	842169	69913	9212	5980	4760	1384	1284
Coke ALL St. Dev.	22614	2625	3045	1193	1178	431	118
CB Mean	841806	70225	8882	6311	5243	1578	1257
CB St. Dev.	20090	2236	2054	1277	1252	441	112
CW Mean	835344	67956	9304	5059	4003	1072	1235
CW St. Dev.	26954	3392	2382	425	520	245	102
CC5 Mean	845500	69983	9877	5622	4020	1089	1360
CC5 St. Dev.	25119	2744	4548	879	407	110	99

	Ca	K	Na	Mg	Ni	P	Mn
Coke ALL Mean	1079	732.4	473.4	459.6	223.9	129.9	109.7
Coke ALL St. Dev.	313	176.2	95.5	113.8	77.5	58.1	55.9
CB Mean	1067	761.9	458.3	482.6	234.3	148.9	136.7
CB St. Dev.	370	166.6	92.6	117.0	91.5	60.0	49.9
CW Mean	913	636.5	420.5	361.9	203.1	111.6	68.9
CW St. Dev.	98	103.5	70.0	49.3	16.9	53.6	53.1
CC5 Mean	1168	705.7	525.6	447.4	209.6	96.4	67.8
CC5 St. Dev.	173	199.1	87.2	102.4	50.3	32.5	25.6

	Zr	Sr	Ba	Ce	Cu	La	Mo
Coke ALL Mean	68.7	51.0	49.9	26.7	16.9	13.3	13.3
Coke ALL St. Dev.	28.8	12.0	11.3	7.0	7.1	3.2	4.1
CB Mean	78.7	51.4	54.6	29.8	17.8	14.9	14.7
CB St. Dev.	32.9	11.8	11.3	7.0	7.5	3.0	4.5
CW Mean	49.3	35.2	38.3	20.6	13.1	11.3	10.9
CW St. Dev.	7.8	2.2	1.2	3.7	1.2	1.3	0.9
CC5 Mean	54.9	56.0	44.3	22.3	16.3	10.7	11.1
CC5 St. Dev.	5.0	9.5	7.2	2.5	7.1	1.2	2.0

	Zn	Nd	Co	Cr	Y	Pb
Coke ALL Mean	12.9	11.2	9.1	8.8	7.8	6.6
Coke ALL St. Dev.	4.5	2.9	1.3	4.6	2.1	3.2
CB Mean	14.0	12.4	9.3	8.6	8.5	8.0
CB St. Dev.	5.0	3.0	1.3	4.4	2.3	3.4
CW Mean	9.4	8.3	7.4	13.7	6.0	3.7
CW St. Dev.	1.4	1.5	0.7	0.0	1.3	0.1
CC5 Mean	11.8	9.5	9.1	7.6	6.9	4.8
CC5 St. Dev.	3.2	0.9	1.2	4.7	0.5	0.7

APPENDIX D: X-RAY DIFFRACTION PHASE IDENTIFICATION

Figure-of-merit values for chemically-possible crystalline phases identified in synchrotron PXRD patterns of bulk coke samples using "Match!" software, Version 3.0, by Crystal Impact, with the ICDD PDF database.

Table D-1. "C" denotes aromatic carbon crystallites and "VOTTDPz" indicates the organically-complexed V phase.

Sample	C	SiO_2	TiO_2	$NiSO_4$ $6H_2O$	VOTTDPz	Muscovite
AB000-3	0.856	0.853	0.836	0.847	0.843	0.790
AB200-1	0.845	0.850	0.826	0.848	0.869	0.805
AB700-2	0.859	0.862	0.826	0.847	0.810	0.792
CX050-1	0.868	0.844	0.838	0.886	0.881	0.850
CX300-4	0.831	0.831	0.797	0.883	0.879	0.842
CX500-1	0.863	0.851	0.834	0.876	0.875	0.829
DM050-3	0.835	0.846	0.802	0.869	0.850	0.833
DM550-1	0.840	0.856	0.811	0.848	0.857	0.852
DM950-2	0.871	0.854	0.815	0.835	0.848	0.803

APPENDIX E: VANADIUM PORPHYRIN MOLECULE XAS MODELLING

Table E-1. Vanadyl octaethyl porphyrin atomic coordinates, from Molinaro and Ibers (1976)

Atom	x (Å)	y (Å)	z (Å)	cont'd	x (Å)	y (Å)	z (Å)
V	-4.77	1.34	4.65	C	-5.30	-1.71	4.12
O	-3.88	1.81	3.39	C	-4.71	-3.02	4.32
N	-3.45	1.43	6.28	C	-3.59	-2.85	5.07
N	-5.60	3.13	5.39	C	-3.47	-1.42	5.34
N	-6.68	0.95	3.88	C	-2.49	-0.81	6.11
N	-4.54	-0.75	4.78	C	-0.23	0.39	7.90
C	-2.47	0.51	6.55	C	-0.48	-0.43	9.16
C	-1.45	1.09	7.39	C	-1.10	3.41	8.46
C	-1.83	2.37	7.65	C	-1.51	3.46	9.88
C	-3.09	2.58	6.96	C	-5.20	6.55	6.89
C	-3.81	3.76	6.93	C	-4.11	7.27	6.14
C	-4.97	4.03	6.22	C	-7.73	6.18	4.97
C	-5.66	5.30	6.18	C	-7.41	6.80	3.62
C	-6.72	5.15	5.35	C	-9.86	2.04	2.20
C	-6.69	3.78	4.87	C	-9.53	2.80	0.93
C	-7.62	3.21	4.02	C	-9.11	-1.06	1.82
C	-7.63	1.89	3.56	C	-8.67	-1.18	0.39
C	-8.67	1.30	2.75	C	-5.34	-4.37	3.86
C	-8.36	-0.02	2.60	C	-4.72	-4.79	2.61

By systematically adjusting interatomic distances between V and the surrounding atoms in porphyrin molecular models, and then computing the expected near-edge spectrum using, it was possible to associate particular structural distortions with variations in the magnitude and position of features in the V K-edge. By increasing the radius of the cluster of atoms included in the computation, it was possible to determine which atoms interacted with the central V atom to generate near-edge features in the first place.

The V=O (vanadyl) bond is responsible for the white-line peak observed at ~5490 eV. The pre-edge peak at 5469.3 eV is induced by the four N ligands in a square-planar arrangement around the V atom. By including the first shell of C atoms from the pyrrole groups in the computation, the shoulder at ~5480 eV appears. Finally, when increasing the effective modelling radius to include all C atoms from the structure, all near-edge features converged to their expected energy positions. When the V=O bond distance was decreased from 1.61 Å (Molinaro and Ibers 1976), the computed pre-edge feature was found to drift to higher energy and grow in magnitude until it eventually split into a doublet structure with smaller magnitude. This occurred at a V=O distance of 1.56 Å. When the V=O distance was increased from 1.61 Å, the computed pre-edge feature drifted to lower

energy and smaller magnitude, then split into a doublet structure with larger magnitude. This occurred at a V=O distance of 1.65 Å (Figure E-1a).

When the V-N distances were decreased from 2.10 Å (Molinaro and Ibers 1976), the pre-edge feature drifted to lower energy and eventually split into a doublet structure with low magnitude at 2.04 Å. When the V-N distances were increased from 2.10 Å, the pre-edge feature split into a doublet structure with the higher-energy peak dramatically increasing in magnitude at a V-N distance of just 2.12 Å (Figure E-1b).

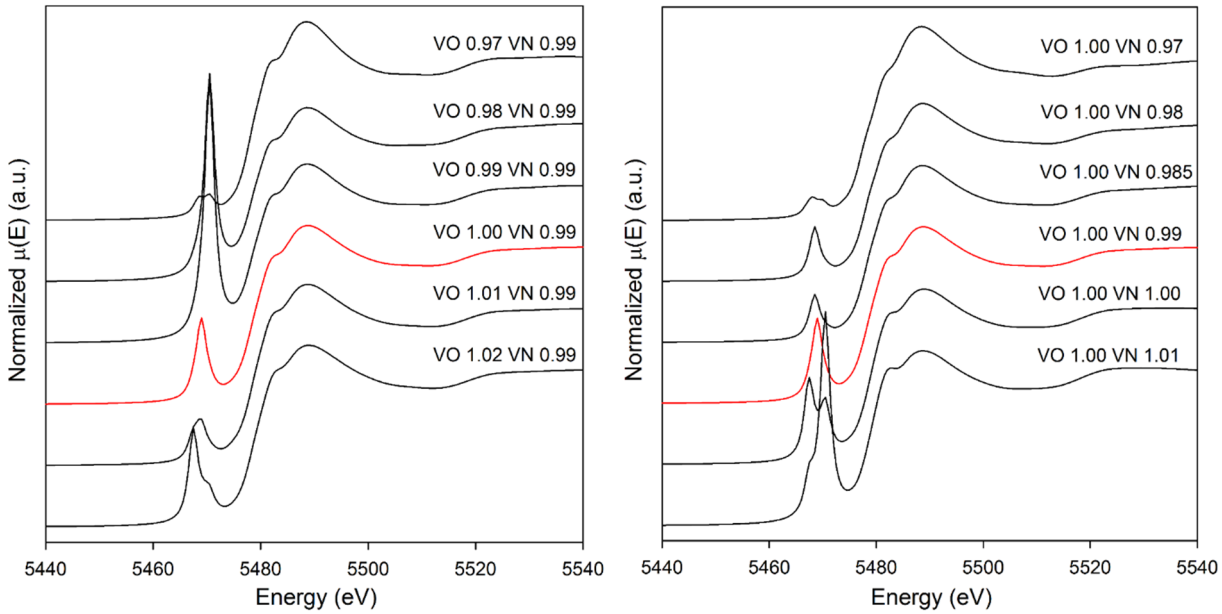

Figure E-1. a) Modelling the effect of systematically varying the porphyrin V=O bond distance on the V pre-edge and near-edge features, while holding V-N distance constant. b) Modelling the effect of systematically varying the porphyrin V-N bond distance on the V pre-edge and near-edge features, while holding V=O distance constant.

Previous studies such as Reynolds et al. (1987) had noted the potential substitution of S for N atoms surrounding the central V atom in porphyrin complexes. This substitution was modelled and the XANES spectra computed, resulting in a consistent and extreme splitting of the pre-edge feature (data not shown). Thus it was concluded that this substitution mechanism is not appreciably present in coke porphyrin complexes.

The effect of progressively substituting O for the four N atoms around the VO metal centre was investigated next, because fitting sample spectra with VOPBD standard spectra (vanadyl square pyramidal O coordination) yielded good fits. Since the VOOEP molecule described by the atomic coordinates in Molinaro and Ibers (1976) contains some distortion, all four unique N-O

single substitutions, all six unique N-O double substitutions, all four unique N-O triple substitutions, and finally the complete N-O quadruple substitution, were modelled. For simplicity, O atoms were simply substituted in at the N atomic coordinates, since it is unknown what true distortions would be introduced by actual substitution of an O atom.

Regardless of substitution position, increasing the number of substitutions from single to double to triple to quadruple dramatically increased the magnitude of the ~5481 eV shoulder (Figure E-2). The peak at ~5489 eV was also seen to increase in magnitude with more N-O substitution, though not as dramatically as the aforementioned shoulder. While single and double N-O substitutions had limited influence on the pre-edge peak (5469.8 eV), triple and quadruple substitutions greatly diminished the magnitude of this feature.

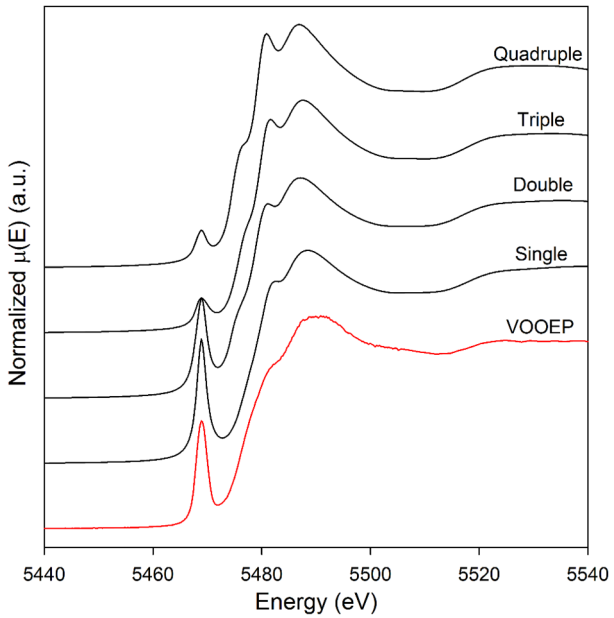

Figure E-2. Graph showing the effect of systematically substituting N atoms with O atoms. Best fit for single, double, triple, and quadruple N-O substitutions are shown.

APPENDIX F: VANADIUM BULK COKE K-EDGE XANES LCF

Table F-1. Summary of V K-edge bulk coke spectra fitting results. Individual component values were not forced between 0-100 %, and the sum of components was not forced to 100 %. Fits 4 & 5 (containing roscoelite *and* V_2O_3) are not listed because V_2O_3 component weights were negative. R-factor represents goodness of fit.

Fit #	VOOEP	VOTPP	VOPBD	Roscoe.	V_2O_3	V_2O_4	Sum	R-factor
1	27 (3) %	68 (2) %			6 (2) %		101%	0.0036
2	30 (3) %	60 (3) %				12 (3) %	101%	0.0035
3	29 (3) %	61 (4) %			1 (3) %	10 (5) %	101%	0.0035
6	28 (3) %	60 (3) %		7 (1) %		6 (3) %	101%	0.0032
7	31 (2) %	62 (2) %		8 (1) %			100%	0.0032
8	20 (2) %	30 (2) %	46 (2) %			7 (2) %	103%	0.0015
9	15 (2) %	35 (2) %	47 (2) %		6 (1) %		102%	0.0015
10	21 (2) %	33 (2) %	44 (2) %	4 (1) %			102%	0.0015
11	20 (2) %	31 (2) %	44 (2) %	4 (1) %		4 (2) %	102%	0.0014

Table F-2. Fit selection decision matrix

Statement 1	• Fit 2 (porph-V_2O_4) is better than Fit 1 (porph-V_2O_3) • Fit 7 (porph-roscoe) is better than Fit 1 (porph-V_2O_3) • Fit 4 (porph-roscoe-V_2O_3-V_2O_4) rejects V_2O_3 from the fit • Fit 5 (porph-roscoe-V_2O_3) rejects V_2O_3 from the fit • Fit 6 (porph-roscoe-V_2O_4) is better than Fit 2 (porph-V_2O_4) • Fit 6 (porph-roscoe-V_2O_4) is better than Fit 7 (porph-roscoe) → ***Both roscoelite-like and V_2O_4-like coordination are more favoured than V_2O_3***
Statement 2	• Fit 8 (porph-V_2O_4-VOPBD) is better than Fit 2 (porph-V_2O_4) • Fit 9 (porph-V_2O_3-VOPBD) is better than Fit 1 (porph-V_2O_3) • Fit 10 (porph-roscoe-VOPBD) is better than Fit 7 (porph-roscoe) → ***VOPBD-like coordination is very favourable***
Statement 3	• Fit 9 (porph-V_2O_3-VOPBD) is better than Fit 8 (porph-V_2O_4-VOPBD) • Fit 10 (porph-roscoe-VOPBD) is better than Fit 8 (porph-V_2O_4-VOPBD) → ***V(III) is favoured over V(IV) as the dominant inorganically-complexed form***
Statement 4	• Fit 10 (porph-roscoe-VOPBD) is better than Fit 9 (porph-V_2O_3-VOPBD) → ***Prefer roscoelite-like over V_2O_3-like coordination as dominant V(III) species***

APPENDIX G: NICKEL PORPHYRIN MOLECULE XAS MODELLING

Table G-1. Nickel octaethyl porphyrin atomic coordinates, one quadrant only. Cartesian coordinates calculated from fractional unit cell coordinates in Meyer (1972).

Table G-2. Nickel tetraphenyl porphyrin atomic coordinates, one quadrant only. Cartesian coordinates calculated from fractional unit cell coordinates in Maclean (1996).

Atom	x (Å)	y (Å)	z (Å)
Ni	0	3.73	1.73
N	1.93	3.61	1.72
C	2.83	4.62	1.41
C	2.70	2.50	2.02
C	4.18	4.12	1.49
C	4.12	2.82	1.90
C	5.41	4.91	1.14
C	5.24	1.85	2.13
C	5.71	4.88	-0.33
C	5.60	1.06	0.89
C	2.20	1.25	2.24

Atom	x (Å)	y (Å)	z (Å)
Ni	0	7.53	-3.47
N	1.67	8.51	-3.45
C	1.84	9.85	-3.23
C	3.23	10.20	-3.38
C	3.88	9.09	-3.73
C	2.93	8.03	-3.75
C	3.25	6.69	-3.92
C	4.65	6.30	-4.27
C	4.98	5.96	-5.56
C	6.26	5.60	-5.89
C	7.23	5.55	-4.93
C	6.94	5.90	-3.63
C	5.65	6.27	-3.32

Nickel octaethyl porphyrin (NiOEP) models were first generated using atomic coordinates from one quarter of porphyrin macrocycle (Meyer, 1972). Model 1 consisted of a 3D spherical cluster and Model 2 consisted of a 2D flake cluster, both based on Meyer (1972). In Model 1, increasing the modelling radius up to 5.7 Å led to best agreement between model and experimental XANES for NiOEP. In Model 2, increasing the modelling radius up to 6.18 Å led to best agreement between model and experimental XANES for NiOEP. A comparison of Model 1 and Model 2 showed no effect on XANES features; XANES modelling results from the two models supported one another. However, the models generally predicted the Ni porphyrin main edge doublet feature peaks to be shifted by roughly -1 eV in energy; they were situated at ~8352 and ~8359 eV in experimental data, but at ~8351 and 8357 eV in calculated spectra.

Next, modelling was performed to examine the effect of structural modifications to the Ni tetraphenyl porphyrin (NiTPP) structure (Maclean, et al., 1996) on Ni K-edge XANES (Figure G-1). Bulk inflation of the structure led to large increases in the relative magnitude of the lower energy feature of the Ni main edge doublet feature. For extreme inflation (20 %) of structure, this lower energy peak (~8351 eV) is considerably higher than the second peak.

Overall, systematic inflation/deflation XANES modelling revealed that the experimental NiTPP standard possessed the same, though slightly deflated, structure as described by Maclean

et al. (1996). The effect of increasing the effective modelling radius was also examined. It was found that calculated XANES spectra converged towards experimental spectra as the effective modelling radius was increased from 2 – 6 Å.

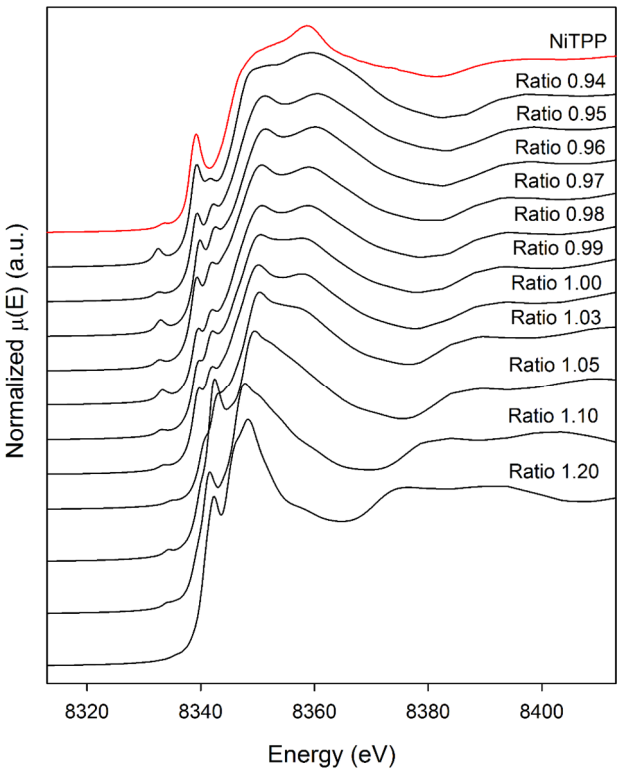

Figure G-1. Graph showing the effect of overall deflation/inflation of the Ni porphyrin molecular structure on the Ni near-edge spectra.

APPENDIX H: COKE DEPOSIT WATER SAMPLE GEOCHEMISTRY

Table H-1. Basic multi-level well sampling information. The depth below surface (DBS), below the water table (DBWT), and the elevation above sea level (ASL) are reported. Sites A, AB, AM, AX, and B are located at the Coke Beach deposit, and Sites C, CB, and CX are located at the Coke Watershed deposit. A sample ("SDW") was taken of the water used to fill the sonic drill rig casing during well installation.

Site	DBS (cm)	Well ID	DBWT (cm)	Elev. ASL (cm)	Date	Time
SA	155	SA-150	46	34948	2014-07-30	1654
SA	184	SA-175	75	34919	2014-07-30	1635
SA	210	SA-200	101	34893	2014-07-30	1613
SA	232	SA-225	123	34871	2014-07-30	1551
SA	258	SA-250	149	34845	2014-07-30	1511
SA	309	SA-300	300	34794	2014-07-30	1447
SA	406	SA-400	297	34697	2014-07-30	1413
SA	503	SA-500	394	34600	2014-07-30	1352
SA	592	SA-600	483	34511	2014-07-30	1327
SA	802	SA-800	693	34301	2014-07-30	1245
SAB	330	SAB-300	166	34777	2014-08-01	1236
SAB	380	SAB-350	216	34727	2014-08-01	1218
SAB	423	SAB-400	259	34684	2014-08-01	1158
SAB	474	SAB-450	310	34633	2014-08-01	1126
SAB	522	SAB-500	358	34585	2014-08-01	1029
SAB	568	SAB-550	404	34539	2014-08-01	1004
SAB	613	SAB-600	449	34494	2014-07-31	1601
SAB	702	SAB-700	538	34405	2014-07-31	1545
SAB	793	SAB-800	629	34314	2014-07-31	1527
SAM	146	SAM-150	81	34972	2014-07-31	1426
SAM	171	SAM-175	106	34947	2014-07-31	1407
SAM	196	SAM-200	131	34922	2014-07-31	1349
SAM	220	SAM-500	155	34898	2014-07-31	1119
SAM	246	SAM-225	181	34872	2014-07-31	1331
SAM	293	SAM-250	228	34825	2014-07-31	1314
SAM	396	SAM-300	331	34722	2014-07-31	1256
SAM	497	SAM-400	432	34621	2014-07-31	1143
SAM	594	SAM-600	529	34524	2014-07-31	1057
SAM	791	SAM-800	726	34327	2014-07-31	1031
SAX	119	SAX-100	52	34874	2014-08-02	959
SAX	147	SAX-125	80	34846	2014-08-02	934
SAX	174	SAX-150	107	34819	2014-08-01	1720
SAX	199	SAX-175	132	34794	2014-08-01	1653
SAX	223	SAX-200	156	34770	2014-08-01	1634
SAX	274	SAX-250	207	34719	2014-08-01	1614
SAX	321	SAX-300	254	34672	2014-08-01	1544
SAX	419	SAX-400	352	34574	2014-08-01	1522
SAX	518	SAX-500	451	34475	2014-08-01	1453
SAX	602	SAX-600	535	34391	2014-08-01	1422
SB	97	SB-100	25	34911	2014-08-02	1528
SB	122	SB-150	50	34886	2014-08-02	1450
SB	150	SB-125	78	34858	2014-08-02	1514
SB	174	SB-200	102	34834	2014-08-02	1409
SB	199	SB-175	127	34809	2014-08-02	1428
SB	250	SB-250	178	34758	2014-08-02	1349
SB	302	SB-500	230	34706	2014-08-02	1134

SB	351	SB-300	279	34657	2014-08-02	1325
SB	399	SB-350	327	34609	2014-08-02	1215
SB	499	SB-400	427	34509	2014-08-02	1153
SB	597	SB-600	525	34411	2014-08-02	1110
SC	560	SC-560	109	34467	2014-09-07	947
SC	585	SC-585	134	34442	2014-09-06	1607
SC	635	SC-635	184	34392	2014-09-06	1549
SCB	297	SBC-297	12	35023	2014-09-06	1141
SCB	320	SBC-320	35	35000	2014-09-06	1207
SCB	348	SBC-348	63	34972	2014-09-06	1112
SCB	372	SBC-372	87	34948	2014-09-06	1252
SCB	424	SBC-424	139	34896	2014-09-06	1313
SCB	474	SBC-474	189	34846	2014-09-06	1042
SCB	572	SBC-572	287	34749	2014-09-06	1330
SCB	800	SBC-800	497	34538	2014-09-05	1652
SCX	351	SCX-351	40	34839	2014-09-05	1420
SCX	377	SCX-377	66	34813	2014-09-05	1342
SCX	403	SCX-403	92	34787	2014-09-05	1322
SCX	499	SCX-499	188	34691	2014-09-05	1445
SCX	601	SCX-601	290	34589	2014-09-05	1251
SDW	0		0	0	2014-09-07	1300

Table H-2. Aqueous geochemical parameters measured in the field. Temperature (T), $E_{measured}$ (E), alkalinity as $CaCO_3$ (Alk.), electrical conductivity (EC), and spectrophotometrically-determined sulphide (S^{2-}) concentrations are reported.

Site	DBS (cm)	T (°C)	pH	E (mV)	Eh (mV)	Alk. (mg L^{-1})	EC (µS cm^{-1})	S^{2-} (µg L^{-1})
SA	155	16.5	7.58	340	592	236	1023	6
SA	184	15.8	7.61	239	491	168	1143	10
SA	210	15.4	7.81	171	423	170	1233	5
SA	232	15.2	7.96	174	427	155	1294	4
SA	258	13.5	7.37			74	1353	4
SA	309	14.1	7.41	54	307	56	1935	2
SA	406	14.3	7.94	7	260	128	1445	2
SA	503	15.2	8.10	8	260	296	1592	2
SA	592	15.9	8.32	105	357	455	2781	18
SA	802	15.6	8.38	5	257	392	3530	6
SAB	330	12.8	7.50	12	266	165	1357	0
SAB	380	12.9	7.56	3	257	279	1691	0

SAB	423	13.2	7.67	-2	252	355	2257	0
SAB	474	13.3	7.72	-29	225	416	2945	1
SAB	522	13.5	7.80	-62	192	419	3190	0
SAB	568	13.9	7.74	-78	175	432	3360	0
SAB	613	16.6	7.81	-113	139	434	3280	4
SAB	702	17.4	7.90	-135	116	439	3160	4
SAB	793	17.8	7.92	-155	96	458	3130	25
SAM	146	21.1	6.16	252	500	7	274.8	3
SAM	171	16.1	6.17	189	441	19	408	3
SAM	196	15.7	6.81	81	334	53	657	7
SAM	220	14.9	7.25	-5	248	71	798	4
SAM	246	14.9	7.38	-29	224	63	814	7
SAM	293	14.4	7.78	-58	195	161	1010	3
SAM	396	15	8.23	-95	158	464	3210	3
SAM	497	14.6	8.07	-110	143	464	3590	3
SAM	594	15.3	8.04	-113	140	512	3610	2
SAM	791	16.1	8.08	-128	124	552	3740	2
SAX	119	15.8	7.56	65	317	94	507	0
SAX	147	9.7	7.99	0	256	146	640	0
SAX	174	8.2	8.01	-47	210	192	725	0
SAX	199	8.6	8.02	209	466	238	787	2
SAX	223	8	8.01	99	356	238	875	1
SAX	274	9.2	8.16	7	264	427	1185	1
SAX	321	10.7	8.26	3	259	580	2285	1
SAX	419	10.3	8.19	-76	180	510	3270	5
SAX	518	11.6	8.20	47	302	682	3590	1
SAX	602	11.6	8.25	-116	139	800	3510	24
SB	97	18.5	7.33	109	359	197	1086	4
SB	122	16.7	7.07	114	366	117	1469	7
SB	150	18.1	6.84	115	366	44	1396	4
SB	174	15.7	6.99	32	284	40	1249	3
SB	199	14.5	7.09	41	294	55	917	3
SB	250	13.5	7.32	55	309	88	646	3
SB	302	11.9	7.64	-36	219	152	490	3
SB	351	15.2	4.69	-40	213	174	625	2
SB	399	12.9	7.77	-82	172	211	752	2
SB	499	13.8	8.11	-82	172	486	2578	3
SB	597	13.9	8.12	-119	134	448	3200	5
SC	560	5.5	7.52	-12	247	1139	5730	25
SC	585	8.6	7.21	-59	198	1291	6040	10
SC	635	8.7	7.63	-68	188	1370	6180	36
SCB	297	8.9	6.44	298	554	23	1296	2
SCB	320	8.5	6.72	125	382	54	1335	7
SCB	348	8.8	6.34	224	480	100	1263	0
SCB	372	8.1	7.07	31	288	84	682	28
SCB	424	8.3	7.66	-89	168	221	1544	20
SCB	474	8.6	7.58	-53	204	299	1618	24
SCB	572	8.5	7.67	176	432	196	1687	0
SCB	800	10.6	7.79	-3	253	258	1624	8
SCX	351	9.9	7.18	142	398	100	1317	3
SCX	377	10	7.56	148	404	183	1445	4
SCX	403	9.7	7.53	283	539	235	1542	8
SCX	499	9.2	7.74	36	292	547	3200	1
SCX	601	11.8	8.01	-11	244	789	3590	0
SDW								

Table H-3. Spectrophotometrically-determined N concentration (as NH_3), stable isotopes of water (δD & $\delta^{18}O$), and FTIR-determined acid-extractable organics / naphthenic acids (NAs) are reported. Samples for which replicates (Rep.) were analyzed are indicated as either "in" (replicates analyzed by author internally at single lab) or "inB" (blind replicates analyzed by technician internally at single lab).

Site	DBS (cm)	NH_3 (mg L^{-1})	Rep.	δD (‰)	$\delta^{18}O$ (‰)	Rep.	NAs (mg L^{-1})	Rep.
SA	155	0.04		-135.7	-16.1		1	
SA	184	0.21	in	-128.6	-15.1		<1	
SA	210	0.47		-130.8	-15.9		<1	
SA	232	1.64		-128.2	-15.2		<1	
SA	258	3.36		-132.2	-15.5		<1	
SA	309	8.29		-136.5	-16.2		<1	
SA	406	3.69		-136.2	-15.9		<1	
SA	503	2.17	in	-129.4	-14.6		<1	
SA	592	2.34		-114.4	-12.5		<1	inB
SA	802	3.14	in	-114.8	-12.9		<1	
SAB	330	25.57		-150.7	-18.2	in	<1	
SAB	380	22.85		-143.7	-17.5	in	<1	
SAB	423	19.3		-131.3	-15.2	in	<1	
SAB	474	16.3	in	-124.5	-14.0	in	<1	inB
SAB	522	10.05	in	-118.7	-14.2	in	1	inB
SAB	568	5.31		-116.0	-13.3	in	<1	
SAB	613	5.26		-118.4	-13.6		2	
SAB	702	4.91		-121.4	-14.3		<1	
SAB	793	4.87		-120.0	-14.2		<2	
SAM	146	0.82		-135.6	-16.6		<2	
SAM	171	0.68		-135.9	-16.4		<1	
SAM	196	1.21		-128.6	-15.2		<2	
SAM	220	2.7	in	-138.4	-17.0		<2	
SAM	246	2.82		-134.5	-15.9		<1	
SAM	293	5.31		-141.6	-16.8		<2	
SAM	396	2.81		-115.7	-13.0		<1	
SAM	497	3.5		-117.2	-13.5		<2	
SAM	594	3.76		-124.6	-14.3		<2	
SAM	791	7.89		-121.1	-13.7		<1	inB
SAX	119	1.28		-139.2	-16.3		<2	
SAX	147	2.21		-143.6	-17.2		<1	inB
SAX	174	2.71		-141.1	-16.9	in	<2	
SAX	199	2.05		-142.8	-17.1	in	<2	
SAX	223	2.25		-144.2	-17.6	in	<1	
SAX	274	2.2		-134.9	-16.1	in	<2	
SAX	321	2.48		-120.4	-13.2	in	<2	inB
SAX	419	3.81		-118.5	-13.4	in	<2	
SAX	518	5.53		-114.2	-12.1	in	<2	
SAX	602	7.06		-118.5	-13.8	in	2	
SB	97	0.51		-126.6	-16.1		8	
SB	122	0.77		-126.1	-15.6		3	
SB	150	1.25		-123.7	-15.3		<1	
SB	174	4.07		-127.0	-15.7		<2	inB
SB	199	5.83		-131.9	-16.6		<1	
SB	250	5		-143.5	-18.3		<1	
SB	302	2.62		-147.1	-18.8		<2	
SB	351	3.46		-152.3	-18.8		<2	
SB	399	2.89		-155.9	-19.5		<2	inB
SB	499	3.19		-127.6	-15.3		<1	

SB	597	3.96	-120.2	-14.2	<1	inB
SC	560	1.41	-143.6	-17.2	19	inB
SC	585	6.2	-143.9	-17.2	14	
SC	635	7.35	-146.3	-17.2	<2	
SCB	297		-149.5	-18.4	18	
SCB	320	0.29	-148.8	-17.9	<2	
SCB	348		-146.4	-17.8	<2	
SCB	372	0.18	-148.6	-18.4	<2	
SCB	424	2.14	-147.7	-17.7	2	
SCB	474	0.76	-147.9	-17.7	3	
SCB	572	2.25	-146.5	-17.6	3	
SCB	800	1.1	-151.4	-18.5	2	
SCX	351	0.337	-158.4	-19.4	<2	
SCX	377	2.32	-154.3	-18.7	<2	
SCX	403	3.52	-146.6	-17.4	<2	
SCX	499	2.72	-129.0	-15.3	<2	
SCX	601	9.11	-126.1	-14.9	<2	
SDW			-148.8	-19.0	8	

Table H-4. Inorganic anions analyzed by ion chromatography. All values reported in mg L^{-1}. Samples for which replicates (Rep.) were analyzed are indicated as either "inB" (blind replicates analyzed by technician internally at single lab) or "ex" (replicates analyzed at a second external lab).

Site	DBS (cm)	Rep.	Br	Cl	F	NO_3-N	NO_2-N	SO_4	PO_4
SA	155		<0.2	44.9	0.71	<0.2	0.7	202.0	2.12
SA	184	inB	<0.2	66.5	0.49	<0.2	<0.1	273.5	2.67
SA	210		<0.2	73.3	0.41	<0.2	0.9	301.0	2.70
SA	232		<0.2	81.0	0.42	<0.2	1.3	340.0	2.86
SA	258		<0.2	113.0	0.21	<0.2	<0.1	366.0	3.09
SA	309		<0.2	237.0	0.14	<0.2	<0.1	484.0	4.35
SA	406		<0.2	125.0	0.32	<0.2	<0.1	387.0	2.79
SA	503	ex	<0.2	93.0	1.18	<0.05	<0.05	334.7	1.05
SA	592		<0.2	244.0	1.76	<0.2	<0.1	553.0	1.81
SA	802		<0.2	502.0	1.57	<0.2	<0.1	543.0	1.59
SAB	330		<0.2	25.7	0.39	<0.2	0.8	441.0	2.21

SAB	380		<0.2	70.6	0.71	<0.2	0.5	418.0	2.82
SAB	423		<0.2	155.0	1.11	<0.2	<0.1	476.0	3.52
SAB	474	inB	<0.2	310.0	1.28	<0.2	<0.1	532.0	2.75
SAB	522	inB	<0.2	428.0	1.32	<0.2	<0.1	534.0	2.11
SAB	568		<0.2	477.0	1.29	<0.2	<0.1	499.0	1.78
SAB	613		<0.2	477.0	1.28	<0.2	<0.1	476.0	1.92
SAB	702		<0.2	487.0	1.19	<0.2	<0.1	419.0	1.35
SAB	793		<0.2	481.0	1.13	<0.2	<0.1	389.0	1.04
SAM	146		<0.2	0.2	<0.05	<0.2	0.6	105.0	0.23
SAM	171		<0.2	3.4	<0.05	<0.2	0.7	143.0	1.98
SAM	196		<0.2	23.3	0.07	<0.2	3.6	202.0	4.51
SAM	220	inB/ex	<0.2	27.4	0.10	<0.05	<0.05	250.7	2.17
SAM	246		<0.2	29.5	0.10	<0.2	0.7	261.0	2.90
SAM	293		<0.2	42.1	0.42	<0.2	0.8	265.0	0.98
SAM	396		<0.2	465.0	1.56	<0.2	<0.1	518.0	1.54
SAM	497		<0.2	533.0	1.41	<0.2	<0.1	513.0	1.53
SAM	594		0.26	668.0	1.01	<0.2	<0.1	313.0	2.69
SAM	791		0.31	735.0	0.68	<0.2	<0.1	282.0	1.81
SAX	119		<0.2	4.3	0.22	<0.2	1.1	151.0	0.44
SAX	147		<0.2	5.5	0.33	<0.2	1.4	164.0	0.58
SAX	174		<0.2	6.6	0.41	<0.2	1.5	167.0	0.65
SAX	199		<0.2	8.8	0.54	<0.2	1.4	178.0	0.90
SAX	223		<0.2	10.4	0.67	<0.2	2.6	181.0	0.86
SAX	274		<0.2	22.8	1.14	<0.2	3.7	161.0	1.17
SAX	321		<0.2	166.0	1.73	<0.2	2.8	332.0	2.11
SAX	419		<0.2	451.0	1.21	<0.2	<0.1	440.0	2.54
SAX	518		0.3	630.0	1.04	<0.2	7.1	158.0	1.83
SAX	602		0.35	679.0	1.05	<0.2	<0.1	34.8	1.66
SB	97		<0.2	86.9	0.94	1.8	<0.1	174.0	0.34
SB	122		<0.2	169.0	0.31	<0.2	<0.1	284.0	0.62
SB	150		<0.2	199.0	0.09	<0.2	<0.1	295.0	0.48
SB	174		<0.2	188.0	0.06	<0.2	<0.1	307.0	0.24
SB	199		<0.2	123.0	0.07	<0.2	<0.1	174.0	0.17
SB	250		<0.2	74.7	0.14	<0.2	<0.1	141.0	0.11
SB	302		<0.2	4.3	0.29	<0.2	1.1	79.9	0.20
SB	351		<0.2	3.6	0.29	<0.2	1.2	147.0	0.34
SB	399		<0.2	6.7	0.50	<0.2	1.3	160.0	0.50
SB	499		<0.2	276.0	1.36	<0.2	<0.1	410.0	1.97
SB	597		<0.2	497.0	1.18	<0.2	<0.1	403.0	1.40
SC	560	inB	<0.2	96.7	1.01	<0.2	<0.1	1920.0	<0.1
SC	585		<0.2	151.0	1.14	<0.2	<0.1	1920.0	<0.1
SC	635		<0.2	148.0	1.11	<0.2	<0.1	2050.0	<0.1
SCB	297		<0.2	1.3	<0.05	<0.2	0.8	613.0	0.18
SCB	320		<0.2	5.0	0.06	<0.2	0.9	539.0	0.19
SCB	348		<0.2	2.8	<0.05	0.7	<0.1	549.0	0.20
SCB	372		<0.2	0.6	<0.05	<0.2	0.9	540.0	0.17
SCB	424		<0.2	56.2	0.60	<0.2	0.7	449.0	0.17
SCB	474		<0.2	64.8	0.68	<0.2	0.7	449.0	0.19
SCB	572		<0.2	62.1	0.68	<0.2	0.7	441.0	0.14
SCB	800		<0.2	53.1	0.57	<0.2	0.8	434.0	0.17
SCX	351		<0.2	10.3	0.14	<0.2	1.0	543.0	0.65
SCX	377		<0.2	26.4	0.25	<0.2	1.0	520.0	0.69
SCX	403		<0.2	68.8	0.45	<0.2	2.3	376.0	0.88
SCX	499		<0.2	459.0	0.91	<0.2	<0.1	282.0	2.37
SCX	601		0.25	592.0	1.23	<0.2	<0.1	90.9	1.02
SDW			<0.2	26.5	<0.05	2.0	1.5	29.1	5.74

Table H-5. Major cations analyzed by inductively coupled plasma optical emission spectrometry (ICP-OES). All values reported in mg L^{-1}. Samples for which replicates (Rep.) were analyzed are indicated as either "inB" (blind replicates analyzed by technician internally at single lab) or "ex" (replicates analyzed at a second external lab). Data for Al, Cd, Co, Cr, Cu, Li, Ni, Pb, Sb, Tl, Zr, and Zr not shown because all values were below ICP-OES detection limits. The second/external lab had lower detection limits for some analytes and analyzed a slightly different set of analytes.

Site	DBS (cm)	Rep.	As	B	Ba	Ca	Fe	K	Mg	Mn
SA	155			0.847	BDL	5.48	BDL	BDL	0.56	BDL
SA	184			0.764	BDL	2.97	BDL	BDL	0.90	0.020
SA	210			0.765	BDL	4.35	BDL	BDL	1.31	0.055
SA	232			0.844	BDL	8.82	BDL	5.08	3.33	0.163
SA	258			0.882	BDL	21.70	0.036	6.28	8.40	0.400
SA	309			1.100	0.004	56.00	0.094	11.20	22.90	0.715
SA	406			1.780	BDL	35.50	BDL	10.70	29.00	0.442
SA	503			2.910	BDL	13.90	BDL	8.92	10.30	0.140
SA	592			3.150	BDL	12.80	BDL	10.90	10.40	0.085
SA	802	inB		3.215	BDL	17.85	BDL	11.85	12.45	0.054
SAB	330			1.160	BDL	46.00	BDL	BDL	19.30	0.393
SAB	380			1.920	BDL	24.30	BDL	7.35	17.40	0.169
SAB	423			2.400	BDL	19.30	BDL	10.50	14.50	0.150
SAB	474	inB/ex	0.0046	2.650	BDL	18.82	BDL	13.48	14.60	0.168
SAB	522			2.730	BDL	18.40	0.127	14.60	13.80	0.201
SAB	568			2.810	BDL	17.90	0.141	14.20	12.40	0.231
SAB	613			2.820	BDL	17.60	0.326	13.60	12.00	0.232
SAB	702			2.740	BDL	17.30	0.295	12.50	11.60	0.223
SAB	793			2.590	0.019	17.50	0.194	12.00	11.00	0.233
SAM	146			0.402	BDL	4.35	BDL	BDL	4.46	0.093
SAM	171			0.511	BDL	2.85	BDL	BDL	1.40	0.032
SAM	196			0.723	BDL	7.49	BDL	BDL	2.54	0.214
SAM	220	inB		0.814	BDL	17.25	0.221	5.16	5.91	0.568
SAM	246			0.800	BDL	15.80	0.474	5.21	5.34	0.528
SAM	293			1.700	BDL	49.10	0.124	6.69	24.00	0.408
SAM	396			3.300	BDL	16.00	BDL	11.30	10.60	0.175
SAM	497			3.430	BDL	16.40	0.043	10.40	10.60	0.155
SAM	594			3.370	BDL	17.00	BDL	8.49	10.70	0.131
SAM	791			3.390	0.034	28.90	BDL	10.60	18.10	0.170
SAX	119			1.110	BDL	38.70	BDL	BDL	12.20	0.572
SAX	147	ex	0.0044	1.320	BDL	44.33	BDL	4.18	15.83	0.451
SAX	174			1.620	BDL	38.40	BDL	BDL	15.90	0.187
SAX	199			1.990	BDL	26.30	BDL	BDL	19.00	0.083
SAX	223	inB		2.175	BDL	21.05	BDL	5.17	17.50	0.087
SAX	274			2.830	BDL	8.50	BDL	6.23	7.68	0.012
SAX	321			3.250	BDL	8.69	BDL	8.88	6.43	0.009
SAX	419			3.340	BDL	18.10	BDL	11.00	9.02	0.038
SAX	518			3.490	BDL	18.70	BDL	10.00	11.30	0.049
SAX	602			3.510	0.05	17.30	BDL	9.61	10.60	0.009
SB	97			1.000	BDL	0.19	BDL	BDL	0.21	BDL
SB	122	inB		0.795	BDL	0.53	BDL	5.29	0.59	BDL
SB	150	inB		0.703	BDL	4.63	BDL	BDL	1.30	0.111
SB	174	inB		0.581	BDL	16.55	0.174	BDL	5.34	0.595
SB	199	inB		0.522	BDL	16.55	BDL	BDL	5.23	0.296
SB	250	inB		0.658	BDL	70.45	BDL	BDL	11.30	0.548
SB	302	inB		1.195	BDL	30.70	0.041	BDL	16.65	0.275
SB	351	ex	BDL	1.780	BDL	27.81	BDL	4.54	19.12	0.235

SB	399	inB	2.370	BDL	20.85	0.066	5.34	20.45	0.150
SB	499	inB	3.395	BDL	11.80	BDL	10.25	9.02	0.056
SB	597	inB	3.320	BDL	15.80	0.056	11.15	10.90	0.068
SC	560	inB	4.580	0.019	176.00	0.592	18.05	97.40	0.988
SC	585		5.240	0.023	143.00	1.400	18.80	92.60	0.606
SC	635		5.470	0.01	163.00	0.916	20.10	122.00	0.517
SCB	297		0.318	BDL	91.10	BDL	7.32	51.70	0.554
SCB	320		0.420	BDL	84.00	BDL	6.77	45.20	0.522
SCB	348		0.299	BDL	81.40	BDL	6.95	45.20	0.549
SCB	372		0.265	0.009	89.60	2.080	6.56	44.60	0.756
SCB	424		0.857	0.072	66.10	3.300	6.58	34.80	0.543
SCB	474		0.933	0.09	66.30	1.250	7.14	35.40	0.483
SCB	572		1.040	0.102	56.40	BDL	7.10	31.00	0.406
SCB	800		0.895	0.089	67.20	0.663	6.91	35.00	0.500
SCX	351		0.727	BDL	136.00	BDL	BDL	45.50	0.265
SCX	377		1.070	BDL	131.00	BDL	BDL	43.90	0.305
SCX	403		1.680	BDL	71.60	BDL	BDL	26.50	0.201
SCX	499		2.220	BDL	16.70	BDL	8.95	10.50	0.036
SCX	601		2.040	BDL	13.80	BDL	8.60	9.77	0.015
SDW			BDL	BDL	41.30	BDL	BDL	9.20	BDL

Table H-5. continued

Site	**DBS (cm)**	**Rep**	**Mo**	**Na**	**P**	**S**	**Se**	**Si**	**Sr**	**V**
SA	155		1.260	242.0	BDL	71.2	BDL	10.80	0.097	3.000
SA	184		1.550	262.0	BDL	95.7	BDL	11.50	0.085	1.550
SA	210		1.580	275.0	BDL	105.0	BDL	11.90	0.110	1.100
SA	232		1.650	288.0	BDL	119.0	BDL	11.30	0.220	0.196
SA	258		1.850	245.0	BDL	128.0	BDL	12.10	0.506	0.100
SA	309		2.520	310.0	BDL	171.0	BDL	13.10	1.350	0.072
SA	406		1.690	237.0	BDL	134.0	BDL	9.02	1.210	BDL
SA	503		1.260	334.0	BDL	115.0	BDL	4.63	0.338	0.170
SA	592		1.740	632.0	BDL	198.0	BDL	3.88	0.449	0.127
SA	802	inB	1.105	765.5	BDL	194.0	BDL	3.54	0.560	0.085
SAB	330		1.320	189.0	BDL	153.0	BDL	8.97	1.200	0.107
SAB	380		1.690	287.0	BDL	146.0	BDL	5.68	0.753	0.242
SAB	423		2.010	430.0	BDL	164.0	BDL	4.55	0.620	0.237
SAB	474	inB/ex	1.700	574.2	0.082	189.9	0.026	4.36	0.591	0.148
SAB	522		1.210	686.0	BDL	185.0	BDL	4.50	0.600	0.124
SAB	568		1.030	712.0	BDL	173.0	BDL	4.64	0.603	0.116
SAB	613		1.090	710.0	BDL	166.0	BDL	4.66	0.596	BDL
SAB	702		0.771	685.0	BDL	144.0	BDL	4.82	0.571	BDL
SAB	793		0.647	673.0	BDL	135.0	BDL	4.77	0.544	BDL
SAM	146		0.117	39.8	BDL	35.5	BDL	21.40	0.119	0.210
SAM	171		1.160	72.6	BDL	48.6	BDL	24.40	0.087	0.632
SAM	196		2.580	121.0	BDL	68.4	BDL	15.30	0.199	0.532
SAM	220	inB	1.345	134.5	BDL	86.5	BDL	15.75	0.353	0.131
SAM	246		1.690	139.0	BDL	88.7	BDL	15.30	0.339	0.149
SAM	293		0.565	118.0	BDL	90.3	BDL	10.10	1.180	0.236
SAM	396		0.942	746.0	BDL	179.0	BDL	4.11	0.506	0.081
SAM	497		0.921	797.0	BDL	179.0	BDL	3.92	0.547	BDL
SAM	594		1.620	798.0	BDL	109.0	BDL	4.13	0.547	BDL
SAM	791		1.070	811.0	BDL	99.2	BDL	4.86	0.852	BDL
SAX	119		0.278	47.6	BDL	763.0	BDL	11.30	0.727	0.239
SAX	147	ex	0.327	56.3	0.068	55.5	0.009	8.66	0.869	0.210
SAX	174		0.388	91.3	BDL	56.7	BDL	7.00	0.843	0.147

SAX	199		0.527	122.0	BDL	61.2	BDL	5.81	0.702	0.182
SAX	223	inB	0.613	147.0	BDL	62.3	BDL	5.36	0.601	0.200
SAX	274		0.720	263.0	BDL	55.2	BDL	4.84	0.285	0.062
SAX	321		1.370	543.0	BDL	117.0	BDL	4.24	0.293	0.070
SAX	419		1.450	738.0	BDL	155.0	BDL	4.27	0.364	0.477
SAX	518		1.110	802.0	BDL	60.7	BDL	4.54	0.690	0.072
SAX	602		1.030	797.0	BDL	18.6	BDL	4.66	0.717	BDL
SB	97		0.268	248.0	BDL	62.1	BDL	4.52	0.033	1.140
SB	122	inB	0.301	303.5	BDL	97.6	BDL	5.89	0.036	0.406
SB	150	inB	0.273	283.0	BDL	98.3	BDL	6.86	0.105	0.085
SB	174	inB	0.220	251.5	BDL	100.5	BDL	8.29	0.296	BDL
SB	199	inB	0.084	155.5	BDL	59.6	BDL	9.03	0.284	0.065
SB	250	inB	BDL	43.9	BDL	47.0	BDL	9.19	1.170	0.071
SB	302	inB	0.113	36.7	BDL	27.8	BDL	7.66	0.870	BDL
SB	351	ex	0.239	74.8	0.049	48.8	0.012	6.46	0.784	BDL
SB	399	inB	0.331	112.0	BDL	54.0	BDL	5.79	0.591	BDL
SB	499	inB	1.180	578.5	BDL	140.5	BDL	4.18	0.352	0.053
SB	597	inB	0.900	696.5	BDL	139.5	BDL	4.22	0.482	BDL
SC	560	inB	BDL	1190.0	BDL	600.0	BDL	6.61	4.350	BDL
SC	585		BDL	1300.0	BDL	602.0	BDL	6.01	4.270	BDL
SC	635		BDL	1290.0	BDL	669.0	BDL	5.98	5.410	BDL
SCB	297		0.086	118.0	BDL	214.0	BDL	30.60	1.590	1.080
SCB	320		0.122	118.0	BDL	185.0	BDL	26.00	1.340	0.955
SCB	348		BDL	108.0	BDL	187.0	BDL	29.90	1.360	1.050
SCB	372		BDL	99.3	BDL	181.0	BDL	30.30	1.310	BDL
SCB	424		BDL	205.0	BDL	148.0	BDL	19.10	1.160	BDL
SCB	474		BDL	228.0	BDL	148.0	BDL	18.40	1.210	BDL
SCB	572		BDL	253.0	BDL	138.0	BDL	16.00	1.130	BDL
SCB	800		0.082	210.0	BDL	151.0	BDL	17.90	1.200	BDL
SCX	351		0.385	78.5	BDL	182.0	BDL	13.70	1.110	0.870
SCX	377		0.453	114.0	BDL	176.0	BDL	11.20	1.220	0.117
SCX	403		0.525	209.0	BDL	126.0	BDL	7.36	1.090	0.087
SCX	499		1.470	694.0	BDL	100.0	BDL	5.01	0.390	0.121
SCX	601		0.680	725.0	BDL	30.6	BDL	5.06	0.413	BDL
SDW			BDL	17.0	1.420	10.6	BDL	1.54	0.243	BDL

Table H-6. Trace elements analyzed by inductively coupled plasma mass spectrometry (ICP-MS). All values reported in mg L^{-1}. Samples for which replicates (Rep.) were analyzed are indicated as either "inB" (blind replicates analyzed by technician internally at single lab) or "inL" (lab replicates analyzed by technician internally at a single lab). Data for Ag, Ce, Dy, Er, Eu, Gd, Hf, Ho, La, Lu, Nb, Nd, Pb, Pr, Sm, Sn Ta, Tb, Th, Tl, Tm, Y, and Yb not shown because values for all samples were below 1 µg L^{-1} or below ICP-MS detection limits.

Site	DBS (cm)	Rep.	Al	As	B	Ba	Ca	Co	Cr
SA	155	inL	0.017	0.003	0.756	0.005	4.939	0.001	0.000
SA	184		0.016	0.001	0.687	0.005	2.723	0.000	0.000
SA	210		0.018	0.002	0.663	0.007	3.938	0.000	<0.00039
SA	232		0.019	0.004	0.738	0.015	8.033	0.000	<0.00039
SA	258	inB	0.008	0.001	0.783	0.032	20.062	0.001	<0.00039
SA	309		0.007	0.001	0.972	0.061	52.513	0.001	<0.00039
SA	406	inL	0.015	0.002	1.577	0.044	32.215	0.000	<0.00039
SA	503		0.033	0.004	2.552	0.020	13.119	0.000	0.000
SA	592		0.061	0.007	2.798	0.027	12.385	0.000	0.000
SA	802	inL	0.066	0.007	2.798	0.042	17.329	0.000	<0.00039
SAB	330		0.013	0.000	0.991	0.054	42.402	0.001	<0.00039
SAB	380		0.016	0.001	1.670	0.037	22.589	0.001	<0.00039
SAB	423		0.018	0.002	2.095	0.034	18.751	0.001	<0.00039
SAB	474	inB	0.023	0.002	2.303	0.037	18.232	0.001	0.000
SAB	522		0.028	0.002	2.394	0.041	18.384	0.001	0.000
SAB	568		0.052	0.001	2.496	0.040	17.638	0.001	<0.00039
SAB	613		0.033	0.001	2.561	0.044	17.553	0.000	<0.00039
SAB	702		0.036	0.001	2.472	0.047	17.134	0.000	0.000
SAB	793		0.023	0.001	2.408	0.077	17.029	0.000	0.000
SAM	146		0.010	0.000	0.373	0.008	3.921	0.003	<0.00039
SAM	171		0.020	0.000	0.475	0.008	2.599	0.002	<0.00039
SAM	196		0.009	0.000	0.663	0.015	7.009	0.002	<0.00039
SAM	220	inB	0.012	0.001	0.750	0.025	15.560	0.001	<0.00039
SAM	246	inL	0.010	0.001	0.737	0.026	14.255	0.000	<0.00039
SAM	293		0.018	0.001	1.539	0.047	48.222	0.000	<0.00039
SAM	396		0.035	0.003	3.097	0.032	15.503	0.000	0.001
SAM	497		0.046	0.002	3.262	0.031	15.990	0.000	0.001
SAM	594		0.048	0.002	3.116	0.030	16.474	0.000	0.001
SAM	791		0.030	0.001	3.303	0.093	29.881	0.000	0.001
SAX	119	inB	0.013	0.003	1.025	0.023	39.817	0.001	<0.00039
SAX	147	inB	0.014	0.003	1.194	0.027	45.131	0.000	<0.00039
SAX	174		0.015	0.003	1.452	0.023	37.626	0.000	0.000
SAX	199		0.025	0.002	1.813	0.017	23.595	0.000	<0.00039
SAX	223								
SAX	274		0.036	0.002	2.511	0.010	8.105	0.000	<0.00039
SAX	321		0.047	0.002	2.859	0.014	8.448	0.000	0.000
SAX	419		0.037	0.002	2.934	0.033	17.612	0.000	0.000
SAX	518		0.032	0.001	3.100	0.061	18.418	0.000	0.000
SAX	602		0.024	0.002	3.102	0.108	16.795	0.000	0.001
SB	97	inB	0.016	0.002	0.898	<0.00049	0.274	0.000	0.000
SB	122	inB	0.010	0.001	0.768	0.001	0.581	0.000	0.000
SB	150	inB	0.007	0.001	0.658	0.007	4.603	0.001	<0.00039
SB	174	inB	0.006	0.001	0.529	0.025	15.333	0.001	<0.00039
SB	199	inB/inL	0.005	0.001	0.477	0.017	15.145	0.001	<0.00039
SB	250	inB	0.009	0.000	0.580	0.047	69.214	0.001	<0.00039
SB	302	inB	0.013	0.000	1.011	0.022	28.812	0.000	<0.00039
SB	351	inB	0.016	0.000	1.537	0.024	26.377	0.000	<0.00039

SB	399	inB	0.021	0.000	2.036	0.023	19.166	0.000	<0.00039
SB	499	inB	0.045	0.002	2.959	0.023	11.592	0.000	0.000
SB	597	inB/inL	0.043	0.002	2.932	0.036	15.467	0.000	0.000
SC	560	inB	0.002	0.003	4.666	0.080	206.898	0.002	0.001
SC	585		0.005	0.003	5.188	0.083	161.315	0.001	0.001
SC	635		0.003	0.002	5.376	0.068	183.370	0.001	0.002
SCB	297		0.007	0.002	0.316	0.048	93.632	0.005	<0.00039
SCB	320		0.004	0.002	0.391	0.040	85.224	0.006	<0.00039
SCB	348		0.005	0.001	0.256	0.043	82.418	0.006	<0.00039
SCB	372		0.003	0.002	0.229	0.070	91.462	0.004	<0.00039
SCB	424		0.003	0.001	0.790	0.132	69.812	0.002	<0.00039
SCB	474		0.002	0.006	0.852	0.139	68.238	0.004	<0.00039
SCB	572		0.002	0.002	0.930	0.148	57.696	0.002	<0.00039
SCB	800		0.002	0.002	0.832	0.140	69.308	0.001	<0.00039
SCX	351		0.004	0.002	0.708	0.040	141.676	0.003	<0.00039
SCX	377		0.003	0.001	1.030	0.045	129.432	0.001	<0.00039
SCX	403		0.004	0.001	1.620	0.044	74.297	0.001	<0.00039
SCX	499		0.006	0.002	2.100	0.027	15.961	0.000	0.000
SCX	601		0.011	0.001	2.093	0.049	13.973	0.000	0.000
SDW	0		0.006	<0.00016	0.044	0.033	40.928	0.000	0.000

Table H-6. continued

Site	DBS (cm)	Rep.	Cs	Cu	Fe	Ga	Ge	Hg	K
SA	155	inL	0.000	0.080	<0.0097	0.000	0.000	<0.00068	<0.0065
SA	184		0.000	0.010	0.012	0.000	0.000	0.000	<0.0065
SA	210		0.000	0.009	0.032	0.000	0.000	0.000	<0.0065
SA	232		0.000	0.007	0.047	0.000	0.000	<0.00068	<0.0065
SA	258	inB	0.000	0.005	0.101	0.000	0.000	<0.00068	<0.0065
SA	309		0.001	0.006	0.153	0.000	0.000	<0.00068	2.716
SA	406	inL	0.000	0.005	0.067	0.001	0.000	0.003	4.824
SA	503		0.000	0.007	0.040	0.001	0.000	<0.00068	0.038
SA	592		0.000	0.020	0.024	0.002	0.000	<0.00068	<0.0065
SA	802	inL	0.000	0.034	0.011	0.002	0.000	0.004	<0.0065
SAB	330		0.001	0.003	0.069	0.000	0.000	<0.00068	<0.0065
SAB	380		0.001	0.005	0.042	0.000	0.000	<0.00068	<0.0065
SAB	423		0.001	0.011	0.056	0.000	0.000	<0.00068	<0.0065
SAB	474	inB	0.001	0.017	0.059	0.001	0.000	0.000	<0.0065
SAB	522		0.001	0.021	0.190	0.001	0.000	<0.00068	<0.0065
SAB	568		0.000	0.039	0.192	0.001	0.000	0.003	<0.0065
SAB	613		0.000	0.027	0.415	0.001	0.000	0.002	<0.0065
SAB	702		0.000	0.026	0.408	0.001	0.000	0.001	<0.0065
SAB	793		0.000	0.022	0.363	0.001	0.000	0.001	<0.0065
SAM	146		0.000	0.005	0.043	0.000	0.000	<0.00068	1.385
SAM	171		0.000	0.007	0.031	0.000	0.000	<0.00068	0.812
SAM	196		0.000	0.003	0.089	0.000	0.000	<0.00068	0.483
SAM	220	inB	0.000	0.003	0.269	0.000	0.000	<0.00068	1.951
SAM	246	inL	0.000	0.003	0.522	0.000	0.000	0.002	2.107
SAM	293		0.000	0.002	0.182	0.000	0.000	0.000	3.807
SAM	396		0.000	0.022	0.067	0.002	0.000	0.003	<0.0065
SAM	497		0.000	0.022	0.061	0.002	0.000	0.003	<0.0065
SAM	594		0.000	0.031	0.084	0.002	0.000	0.002	<0.0065
SAM	791		0.000	0.040	0.091	0.000	0.000	0.006	<0.0065
SAX	119	inB	0.000	0.001	<0.0097	0.000	0.000	0.000	3.144
SAX	147	inB	0.000	0.001	0.003	0.001	0.000	<0.00068	2.733
SAX	174		0.000	0.001	0.012	0.001	0.000	<0.00068	2.156

SAX	199		0.000	0.002	<0.0097	0.001	0.000	<0.00068	1.983
SAX	223								
SAX	274		0.000	0.005	0.002	0.001	0.000	<0.00068	0.071
SAX	321		0.000	0.012	<0.0097	0.002	0.000	0.001	<0.0065
SAX	419		0.000	0.021	0.019	0.001	0.000	0.002	<0.0065
SAX	518		0.000	0.023	0.028	0.000	0.000	0.002	<0.0065
SAX	602		0.000	0.025	0.187	0.000	0.000	0.001	<0.0065
SB	97	inB	0.000	0.006	0.003	0.000	0.000	0.002	<0.0065
SB	122	inB	0.000	0.008	0.008	0.000	0.000	<0.00068	<0.0065
SB	150	inB	0.000	0.006	0.040	0.000	0.000	0.001	<0.0065
SB	174	inB	0.000	0.004	0.236	0.000	0.000	0.000	<0.0065
SB	199	inB/inL	0.000	0.003	0.092	0.000	0.000	0.002	<0.0065
SB	250	inB	0.000	0.001	0.037	0.000	0.000	<0.00068	2.904
SB	302	inB	0.000	0.001	0.105	0.000	0.000	<0.00068	2.796
SB	351	inB	0.000	0.001	0.078	0.000	0.000	<0.00068	2.850
SB	399	inB	0.000	0.002	0.138	0.000	0.000	<0.00068	2.516
SB	499	inB	0.000	0.012	0.086	0.001	0.000	0.002	<0.0065
SB	597	inB/inL	0.000	0.016	0.134	0.001	0.000	0.003	<0.0065
SC	560	inB	0.000	0.031	0.466	<0.000051	0.000	<0.00068	<0.0065
SC	585		0.000	0.036	1.522	<0.000051	0.000	<0.00068	<0.0065
SC	635		0.000	0.036	0.967	<0.000051	0.000	<0.00068	<0.0065
SCB	297		0.000	0.008	0.006	<0.000051	0.000	<0.00068	3.952
SCB	320		0.000	0.004	0.084	0.000	0.000	<0.00068	3.745
SCB	348		0.000	0.003	0.017	<0.000051	0.000	<0.00068	4.126
SCB	372		0.000	0.002	1.952	<0.000051	0.000	<0.00068	4.225
SCB	424		0.000	0.004	3.081	<0.000051	0.001	0.001	1.313
SCB	474		0.000	0.004	0.956	<0.000051	0.001	0.000	0.989
SCB	572		0.000	0.005	0.001	<0.000051	0.001	0.000	0.474
SCB	800		0.000	0.004	0.761	<0.000051	0.000	<0.00068	1.392
SCX	351		0.000	0.002	0.015	0.000	0.000	<0.00068	0.426
SCX	377		0.000	0.002	0.020	<0.000051	0.000	0.002	0.566
SCX	403		0.000	0.004	0.008	<0.000051	0.000	0.002	<0.0065
SCX	499		0.000	0.013	0.006	0.000	0.000	0.004	<0.0065
SCX	601		0.000	0.017	0.028	<0.000051	0.000	0.003	<0.0065
SDW	0		0.000	0.007	0.003	0.000	0.000	<0.00068	0.974

Table H-6. continued

Site	DBS (cm)	Rep.	Li	Mg	Mn	Mo	Na	Ni	P
SA	155	inL	0.011	0.370	0.047	1.174	246.882	0.012	0.114
SA	184		0.014	0.668	0.074	1.385	249.909	0.008	0.091
SA	210		0.020	1.030	0.103	1.386	258.174	0.005	0.072
SA	232		0.054	2.815	0.194	1.434	277.130	0.005	0.165
SA	258	inB	0.098	7.230	0.394	1.611	239.986	0.011	0.125
SA	309		0.186	21.403	0.727	2.238	302.418	0.014	0.097
SA	406	inL	0.151	27.650	0.441	1.518	230.656	0.004	0.137
SA	503		0.100	9.082	0.180	1.121	323.375	0.002	0.197
SA	592		0.108	9.310	0.134	1.534	643.221	0.004	0.308
SA	802	inL	0.120	11.272	0.108	1.015	823.353	0.003	0.280
SAB	330		0.087	17.765	0.387	1.195	181.761	0.024	0.062
SAB	380		0.097	16.130	0.202	1.491	273.552	0.028	0.072
SAB	423		0.112	13.812	0.193	1.837	434.351	0.024	0.075
SAB	474	inB	0.124	13.735	0.205	1.584	601.383	0.023	0.097
SAB	522		0.139	12.599	0.241	1.155	695.433	0.019	0.133
SAB	568		0.151	12.479	0.266	0.979	598.099	0.018	0.125
SAB	613		0.157	11.041	0.271	1.032	566.246	0.014	0.139

SAB	702		0.161	11.794	0.258	0.761	513.526	0.004	0.104
SAB	793		0.151	9.997	0.265	0.633	485.971	0.003	0.116
SAM	146		0.037	3.684	0.134	0.140	27.335	0.052	0.040
SAM	171		0.023	1.106	0.084	1.017	46.432	0.031	0.042
SAM	196		0.037	2.105	0.239	2.195	77.129	0.030	0.043
SAM	220	inB	0.069	5.123	0.570	1.262	132.973	0.016	0.074
SAM	246	inL	0.066	4.705	0.522	1.528	138.076	0.012	0.066
SAM	293		0.117	22.889	0.419	0.562	119.041	0.008	0.080
SAM	396		0.133	10.144	0.228	0.959	749.940	0.007	0.190
SAM	497		0.138	10.369	0.212	0.935	806.190	0.006	0.181
SAM	594		0.096	10.352	0.183	1.565	777.766	0.004	0.182
SAM	791		0.117	18.744	0.215	1.044	774.031	0.004	0.115
SAX	119	inB	0.068	13.285	0.594	0.314	50.790	0.012	0.082
SAX	147	inB	0.070	15.711	0.453	0.349	61.722	0.007	0.100
SAX	174		0.065	14.851	0.221	0.394	89.287	0.005	0.100
SAX	199		0.066	17.960	0.130	0.522	120.959	0.005	0.124
SAX	223								
SAX	274		0.082	6.821	0.070	0.704	242.053	0.004	0.226
SAX	321		0.121	5.790	0.070	1.307	471.145	0.007	0.362
SAX	419		0.162	8.480	0.098	1.397	687.570	0.007	0.248
SAX	518		0.128	10.859	0.108	1.080	764.749	0.008	0.251
SAX	602		0.105	10.154	0.071	1.012	708.119	0.004	0.232
SB	97	inB	0.011	0.065	0.002	0.287	230.800	0.007	0.044
SB	122	inB	0.011	0.432	0.011	0.330	317.110	0.010	0.043
SB	150	inB	0.020	1.093	0.163	0.307	288.982	0.021	0.045
SB	174	inB	0.033	4.728	0.587	0.249	248.371	0.019	0.042
SB	199	inB/inL	0.037	4.553	0.316	0.125	153.969	0.014	0.044
SB	250	inB	0.056	10.047	0.542	0.091	42.457	0.018	0.050
SB	302	inB	0.046	15.188	0.298	0.145	35.594	0.007	0.086
SB	351	inB	0.062	19.185	0.264	0.261	78.106	0.007	0.070
SB	399	inB	0.069	19.634	0.190	0.347	109.335	0.007	0.094
SB	499	inB	0.111	8.507	0.113	1.156	601.869	0.009	0.250
SB	597	inB/inL	0.124	10.441	0.124	0.907	687.343	0.009	0.265
SC	560	inB	0.734	104.605	1.130	0.005	1161.463	0.010	0.045
SC	585		0.689	98.805	0.655	0.003	1302.711	0.008	0.052
SC	635		0.775	130.926	0.568	0.002	1293.444	0.006	0.045
SCB	297		0.190	49.340	0.595	0.131	105.659	0.120	0.044
SCB	320		0.157	42.793	0.520	0.164	114.195	0.058	0.064
SCB	348		0.174	42.905	0.549	0.113	102.692	0.094	0.058
SCB	372		0.168	42.046	0.795	0.097	100.277	0.029	0.064
SCB	424		0.153	34.192	0.554	0.107	200.110	0.003	0.065
SCB	474		0.155	34.065	0.537	0.118	225.480	0.006	0.028
SCB	572		0.143	29.546	0.414	0.097	233.501	0.006	0.036
SCB	800		0.145	33.975	0.513	0.124	198.401	0.005	0.058
SCX	351		0.081	45.051	0.311	0.424	78.927	0.048	0.048
SCX	377		0.080	42.923	0.340	0.470	111.396	0.026	0.064
SCX	403		0.080	26.279	0.249	0.549	204.538	0.019	0.048
SCX	499		0.096	9.863	0.094	1.409	666.564	0.009	0.144
SCX	601		0.112	9.958	0.080	0.722	712.912	0.005	0.161
SDW	0		0.004	8.459	0.008	0.002	13.853	0.003	1.345

Table H-6. continued

Site	**DBS (cm)**	**Rep.**	**Rb**	**Sc**	**Sb**	**Se**	**Si**	**Sr**	**Ti**
SA	155	inL	0.009	0.004	0.003	<0.0058	7.985	0.061	0.003
SA	184		0.010	0.004	0.001	<0.0058	8.554	0.052	0.003

SA	210		0.010	0.004	0.001	<0.0058	9.504	0.075	0.003
SA	232		0.010	0.004	0.000	<0.0058	9.147	0.174	0.003
SA	258	inB	0.012	0.004	0.000	<0.0058	9.886	0.473	0.003
SA	309		0.027	0.005	0.000	0.000	11.144	1.347	0.003
SA	406	inL	0.022	0.003	0.000	0.000	7.636	1.202	0.002
SA	503		0.015	0.002	0.000	0.000	3.971	0.285	0.001
SA	592		0.017	0.001	0.000	0.001	3.355	0.387	0.001
SA	802	inL	0.019	0.001	0.000	0.000	3.086	0.548	0.002
SAB	330		0.016	0.003	0.000	0.000	7.346	1.161	0.002
SAB	380		0.021	0.002	0.000	0.000	4.776	0.718	0.001
SAB	423		0.026	0.002	0.000	0.001	3.952	0.617	0.001
SAB	474	inB	0.032	0.002	0.000	0.001	3.745	0.591	0.002
SAB	522		0.030	0.002	0.000	0.001	4.003	0.607	0.002
SAB	568		0.026	0.002	0.000	0.001	4.070	0.604	0.002
SAB	613		0.024	0.002	0.000	0.001	4.247	0.600	0.002
SAB	702		0.020	0.002	0.000	0.001	4.405	0.576	0.002
SAB	793		0.018	0.002	0.000	0.001	4.312	0.543	0.002
SAM	146		0.008	0.007	0.001	0.001	17.092	0.082	0.004
SAM	171		0.009	0.008	0.001	0.001	22.431	0.053	0.005
SAM	196		0.012	0.005	0.001	<0.0058	12.501	0.157	0.003
SAM	220	inB	0.010	0.005	0.000	0.000	15.130	0.311	0.003
SAM	246	inL	0.010	0.005	0.000	0.000	14.728	0.295	0.003
SAM	293		0.017	0.003	0.000	0.001	9.928	1.165	0.003
SAM	396		0.022	0.002	0.000	0.001	4.440	0.486	0.002
SAM	497		0.022	0.001	0.000	0.001	4.254	0.537	0.002
SAM	594		0.019	0.001	0.000	0.001	4.426	0.567	0.002
SAM	791		0.019	0.002	0.000	0.001	4.782	0.863	0.002
SAX	119	inB	0.009	0.004	0.000	0.001	10.735	0.770	0.003
SAX	147	inB	0.010	0.003	0.000	0.000	7.978	0.866	0.002
SAX	174		0.010	0.002	0.000	<0.0058	6.378	0.828	0.002
SAX	199		0.009	0.002	0.000	0.000	5.308	0.699	0.002
SAX	223								
SAX	274		0.012	0.002	0.000	<0.0058	4.388	0.248	0.002
SAX	321		0.017	0.002	0.000	<0.0058	3.899	0.259	0.002
SAX	419		0.019	0.002	0.000	0.001	3.873	0.332	0.002
SAX	518		0.015	0.002	0.000	0.001	4.281	0.697	0.002
SAX	602		0.013	0.002	0.000	0.001	4.397	0.730	0.002
SB	97	inB	0.009	0.002	0.001	0.006	4.043	0.001	0.002
SB	122	inB	0.012	0.002	0.001	0.002	5.353	0.005	0.002
SB	150	inB	0.007	0.003	0.000	0.001	6.228	0.076	0.002
SB	174	inB	0.007	0.003	0.000	0.000	7.552	0.259	0.002
SB	199	inB/inL	0.008	0.003	0.000	0.000	8.002	0.245	0.002
SB	250	inB	0.013	0.003	0.000	0.000	8.263	1.158	0.002
SB	302	inB	0.010	0.003	0.000	0.000	6.610	0.845	0.002
SB	351	inB	0.011	0.002	0.000	<0.0058	5.806	0.766	0.002
SB	399	inB	0.011	0.002	0.000	<0.0058	5.233	0.587	0.001
SB	499	inB	0.017	0.002	0.000	0.001	3.933	0.320	0.001
SB	597	inB/inL	0.020	0.002	0.000	0.001	3.992	0.484	0.001
SC	560	inB	0.011	0.003	0.000	0.003	6.781	5.023	0.003
SC	585		0.014	0.002	0.000	0.003	6.199	4.768	0.003
SC	635		0.017	0.002	0.000	0.003	6.181	5.969	0.003
SCB	297		0.016	0.010	0.000	0.005	31.354	1.623	0.006
SCB	320		0.012	0.009	0.000	0.002	27.682	1.381	0.006
SCB	348		0.014	0.010	0.000	0.004	31.772	1.411	0.006
SCB	372		0.004	0.011	0.000	0.001	32.897	1.365	0.006
SCB	424		0.006	0.007	0.000	0.000	21.625	1.243	0.004

SCB	474		0.007	0.007	0.000	0.001	21.012	1.249	0.004
SCB	572		0.007	0.006	0.000	0.000	15.129	1.122	0.004
SCB	800		0.007	0.006	0.000	0.000	17.424	1.245	0.004
SCX	351		0.005	0.005	0.000	0.000	13.942	1.187	0.003
SCX	377		0.006	0.004	0.000	0.000	10.728	1.261	0.003
SCX	403		0.010	0.003	0.000	0.000	7.196	1.134	0.002
SCX	499		0.012	0.002	0.000	0.001	4.827	0.348	0.002
SCX	601		0.010	0.002	0.000	0.001	5.222	0.440	0.002
SDW	0		0.001	0.001	0.000	0.000	1.396	0.203	0.000

Table H-6. continued

Site	DBS (cm)	Rep.	U	V	W	Zn	Zr
SA	155	inL	0.000	2.940	0.002	0.009	0.001
SA	184		0.000	1.511	0.002	0.003	0.000
SA	210		0.000	1.081	0.002	0.002	0.000
SA	232		0.000	0.198	0.002	0.002	0.000
SA	258	inB	0.000	0.113	0.002	0.003	0.000
SA	309		0.000	0.092	0.000	0.004	0.000
SA	406	inL	0.000	0.051	0.001	0.001	0.000
SA	503		0.002	0.185	0.002	0.002	0.000
SA	592		0.006	0.144	0.005	0.002	0.001
SA	802	inL	0.005	0.105	0.004	0.002	0.001
SAB	330		0.000	0.122	0.001	0.010	0.000
SAB	380		0.001	0.246	0.001	0.010	0.000
SAB	423		0.002	0.250	0.002	0.008	0.000
SAB	474	inB	0.002	0.214	0.003	0.007	0.001
SAB	522		0.003	0.147	0.003	0.006	0.001
SAB	568		0.003	0.138	0.003	0.005	0.007
SAB	613		0.003	0.061	0.003	0.004	0.002
SAB	702		0.003	0.010	0.003	0.001	0.002
SAB	793		0.002	0.006	0.003	0.002	0.001
SAM	146		<0.0000039	0.209	<0.000027	0.029	0.000
SAM	171		<0.0000039	0.565	0.000	0.019	0.000
SAM	196		<0.0000039	0.493	0.001	0.005	0.000
SAM	220	inB	0.000	0.150	0.001	0.003	0.000
SAM	246	inL	0.000	0.162	0.001	0.004	0.000
SAM	293		0.000	0.250	0.001	0.003	0.000
SAM	396		0.006	0.110	0.003	0.002	0.001
SAM	497		0.006	0.013	0.004	0.001	0.002
SAM	594		0.006	0.007	0.004	0.001	0.002
SAM	791		0.001	0.007	0.003	0.001	0.001
SAX	119	inB	0.000	0.259	0.000	0.012	0.000
SAX	147	inB	0.000	0.223	0.000	0.001	0.000
SAX	174		0.001	0.159	0.001	0.001	0.000
SAX	199		0.001	0.190	0.001	0.002	0.000
SAX	223						
SAX	274		0.002	0.083	0.002	0.001	0.001
SAX	321		0.005	0.093	0.008	0.001	0.003
SAX	419		0.003	0.485	0.005	0.002	0.002
SAX	518		0.004	0.097	0.003	0.001	0.002
SAX	602		0.004	0.020	0.002	0.001	0.002
SB	97	inB	0.000	1.183	0.001	0.001	0.000
SB	122	inB	<0.0000039	0.417	0.001	0.002	0.000
SB	150	inB	<0.0000039	0.108	0.001	0.004	0.000
SB	174	inB	<0.0000039	0.065	0.000	0.004	0.000

SB	199	inB/inL	0.000	0.085	0.000	0.003	0.000
SB	250	inB	0.000	0.090	0.000	0.002	0.000
SB	302	inB	0.000	0.044	0.000	0.002	0.000
SB	351	inB	0.000	0.062	0.000	0.001	0.000
SB	399	inB	0.000	0.041	0.001	0.001	0.000
SB	499	inB	0.004	0.079	0.004	0.001	0.001
SB	597	inB/inL	0.003	0.053	0.003	0.001	0.001
SC	560	inB	0.001	0.001	<0.000027	0.005	0.004
SC	585		0.001	0.002	<0.000027	0.006	0.005
SC	635		0.001	0.001	<0.000027	0.005	0.005
SCB	297		<0.0000039	1.126	<0.000027	0.008	0.000
SCB	320		0.000	1.013	<0.000027	0.004	0.000
SCB	348		<0.0000039	1.103	<0.000027	0.005	0.000
SCB	372		0.000	0.050	<0.000027	0.002	0.000
SCB	424		0.000	0.005	<0.000027	0.001	0.000
SCB	474		0.000	0.006	0.000	0.001	0.000
SCB	572		0.000	0.006	0.000	0.001	0.000
SCB	800		0.000	0.003	<0.000027	0.003	0.000
SCX	351		0.000	0.983	0.000	0.003	0.000
SCX	377		0.001	0.135	0.000	0.002	0.000
SCX	403		0.002	0.113	0.001	0.002	0.000
SCX	499		0.003	0.145	0.002	0.001	0.001
SCX	601		0.002	0.019	0.002	0.001	0.002
SDW	0		0.000	0.000	<0.000027	5.639	0.000

APPENDIX J: SELECTIVE EXTRACTION METHODS, MATERIALS, AND RESULTS

The extraction protocol used in this study was developed to examine the release of trace metals from coke under expected field conditions. The composition of coke is very different than that of soils types for which extraction protocols have been developed. Coke is composed almost entirely of an "organic" fraction, so performing the common oxidizable extraction step would essentially target the entire sample. An acid extraction step would be similarly out of place because field conditions are predominantly neutral-alkaline. Aqueous oxidized V species (i.e. V(V) oxyanions) are generally less soluble at low pH regardless.

Three fractions were targeted for extractions: water soluble, exchangeable, and reducible (Table J-1). A water soluble extraction was included because both field data from this project and previous extractions performed on coke indicated its importance (Jack, et al., 1979; Kessler & Hendry, 2006). A slightly alkaline pH, low ionic strength (deionized water) solution was used to simulate precipitation flushing in field conditions. An exchangeable extraction was included to test whether metals affiliated with clay minerals, or adsorbed directly on the coke matrix surfaces can exchange with other cations. A circumneutral pH, high ionic strength solution with pH-buffering capacity was employed. A reducible extraction was used to investigate the possible association of trace metals with amorphous or crystalline oxides hosted in the coke matrix (Blackmore, et al., 1996; Zubot, et al., 2012). A slightly alkaline pH, weak-moderate reductant solution was employed for this step. Coke samples (n = 20) were thawed, vacuum-filtered, freeze-dried, and stored anoxically until immediately prior to the experiment. They were not ground, since grinding samples dramatically increases specific surface area which could exaggerate the release of metals with respect to field conditions.

Table J-1. Selective extraction protocol and summary of reagents used.

Fraction	Solution	Preparation	Extraction
Water Soluble	H_2O (deionized)	pH 7.5	Shake 180 rpm 0.6 h Centrifuge 4000 rpm 40 min
Exchangeable	$Na_2HPO_4 \cdot 7H_2O$ (0.58 M) [1] $NaH_2PO_4 \cdot H_2O$ (0.42 M) [2]	pH 6.7	Shake 180 rpm 16 h Centrifuge 4000 rpm 40 min
Reducible	Na-ascorbate (0.12 M) [3] Na_3-citrate $\cdot 2H_2O$ (0.17 M) [4] $NaHCO_3$ (0.6 M) [5]	pH 8.0	Shake 180 rpm 24 h Centrifuge 4000 rpm 40 min

1) ACS reagent 98.0-102% assay, metals <0.001%; 2) ACS reagent >98.0% assay, metals <0.001%; 3) crystalline >98% assay; 4) BioUltra for molecular biology >99.5% (NT), metals <0.0005%; 5) ACS reagent 99.7-100.3%

Supernatant triplicates for each sample for each fraction were pooled into ~120 mL samples and thoroughly mixed. A 30 mL subsample of each pooled supernatant was filtered to 0.1 µm, acidified to pH 2 with concentrated (67-70%) nitric acid (Millipore Omnitrace), and analysed via ICP-MS. Supernatant for two samples for each fraction were left in triplicate in order to assess reproducibility. No residual extraction step was included because whole-rock elemental analyses were already performed on all samples. Extractant solution blanks for each fraction were analysed via ICP-MS and ICP-OES to determine the background concentration of elements. These concentrations were then subtracted from the sample concentrations. Analyte concentrations in both the blank solutions and the sample supernatants were adjusted to account for the dilution by nitric acid addition. Finally, the mass of analyte released per unit mass of coke was determined for all analytes, for each fraction, for each sample.

Leaching studies have previously shown that the rate and magnitude of V release to be greater than that for other metals like Ni, Mo, and Mn but that the leaching potential of V was still relatively low compared to overall V concentration in coke (Kessler & Hendry, 2006). Concentrations of V and Mo in Syncrude pore water were previously found to be attributable to the water soluble fraction (Kessler & Hendry, 2006). V and Ni consistently displayed the following concentration trend: Exchangeable > Reducible > Water Soluble.

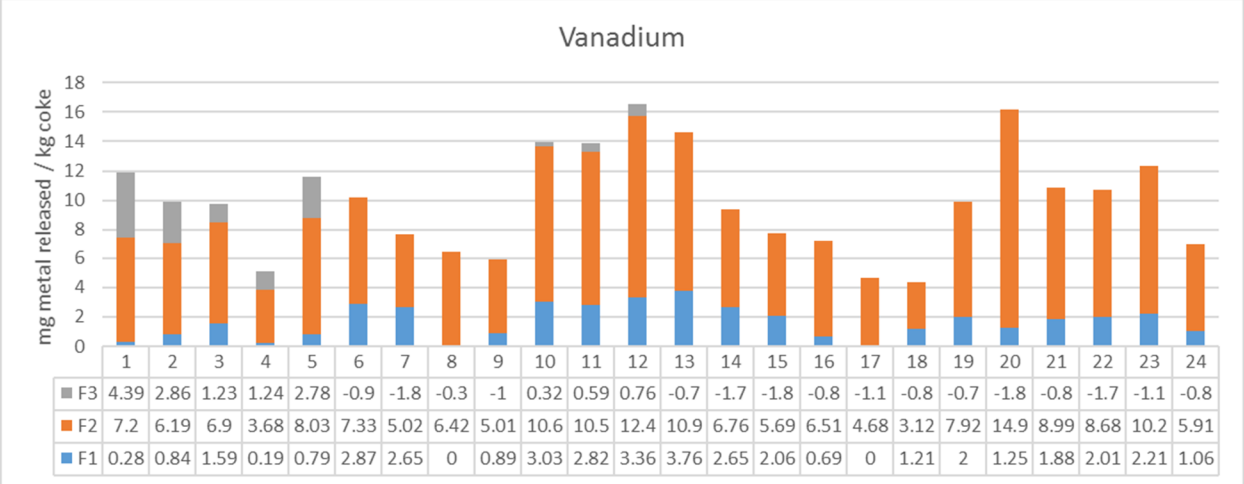

	1	2	3	4	5	6	7	8	9	10	11	12	13	14	15	16	17	18	19	20	21	22	23	24
F3	4.39	2.86	1.23	1.24	2.78	-0.9	-1.8	-0.3	-1	0.32	0.59	0.76	-0.7	-1.7	-1.8	-0.8	-1.1	-0.8	-0.7	-1.8	-0.8	-1.7	-1.1	-0.8
F2	7.2	6.19	6.9	3.68	8.03	7.33	5.02	6.42	5.01	10.6	10.5	12.4	10.9	6.76	5.69	6.51	4.68	3.12	7.92	14.9	8.99	8.68	10.2	5.91
F1	0.28	0.84	1.59	0.19	0.79	2.87	2.65	0	0.89	3.03	2.82	3.36	3.76	2.65	2.06	0.69	0	1.21	2	1.25	1.88	2.01	2.21	1.06

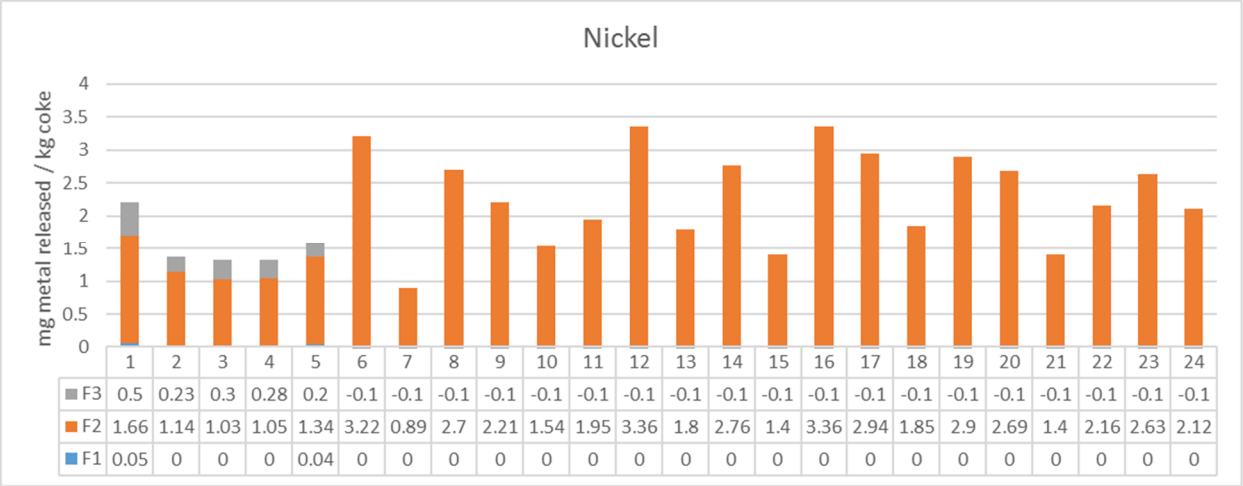

	1	2	3	4	5	6	7	8	9	10	11	12	13	14	15	16	17	18	19	20	21	22	23	24
F3	0.5	0.23	0.3	0.28	0.2	-0.1	-0.1	-0.1	-0.1	-0.1	-0.1	-0.1	-0.1	-0.1	-0.1	-0.1	-0.1	-0.1	-0.1	-0.1	-0.1	-0.1	-0.1	-0.1
F2	1.66	1.14	1.03	1.05	1.34	3.22	0.89	2.7	2.21	1.54	1.95	3.36	1.8	2.76	1.4	3.36	2.94	1.85	2.9	2.69	1.4	2.16	2.63	2.12
F1	0.05	0	0	0	0.04	0	0	0	0	0	0	0	0	0	0	0	0	0	0	0	0	0	0	0

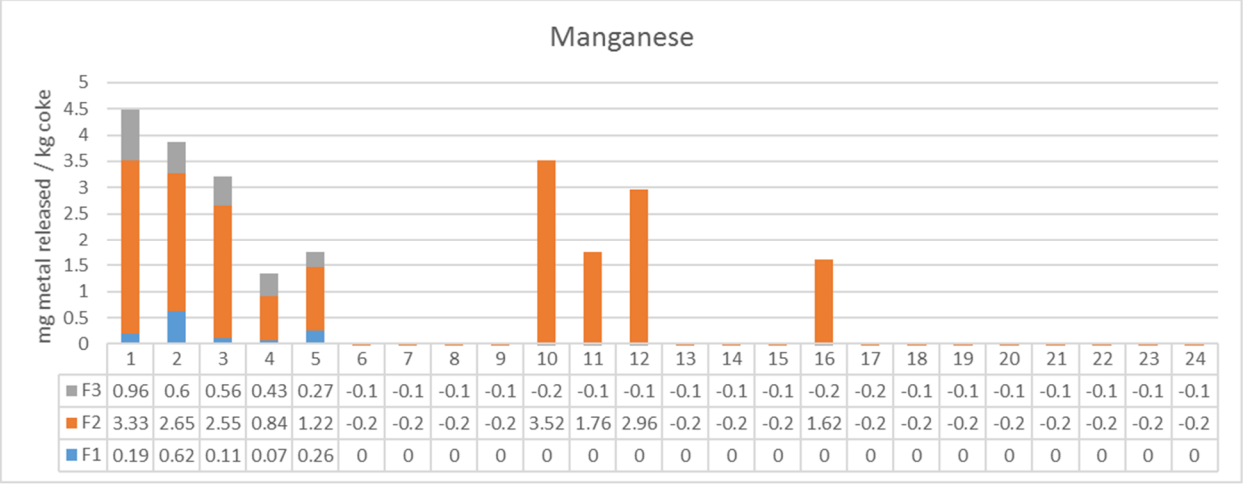

	1	2	3	4	5	6	7	8	9	10	11	12	13	14	15	16	17	18	19	20	21	22	23	24
F3	0.96	0.6	0.56	0.43	0.27	-0.1	-0.1	-0.1	-0.1	-0.2	-0.1	-0.1	-0.1	-0.1	-0.1	-0.2	-0.2	-0.1	-0.1	-0.1	-0.1	-0.1	-0.1	-0.1
F2	3.33	2.65	2.55	0.84	1.22	-0.2	-0.2	-0.2	-0.2	3.52	1.76	2.96	-0.2	-0.2	-0.2	1.62	-0.2	-0.2	-0.2	-0.2	-0.2	-0.2	-0.2	-0.2
F1	0.19	0.62	0.11	0.07	0.26	0	0	0	0	0	0	0	0	0	0	0	0	0	0	0	0	0	0	0

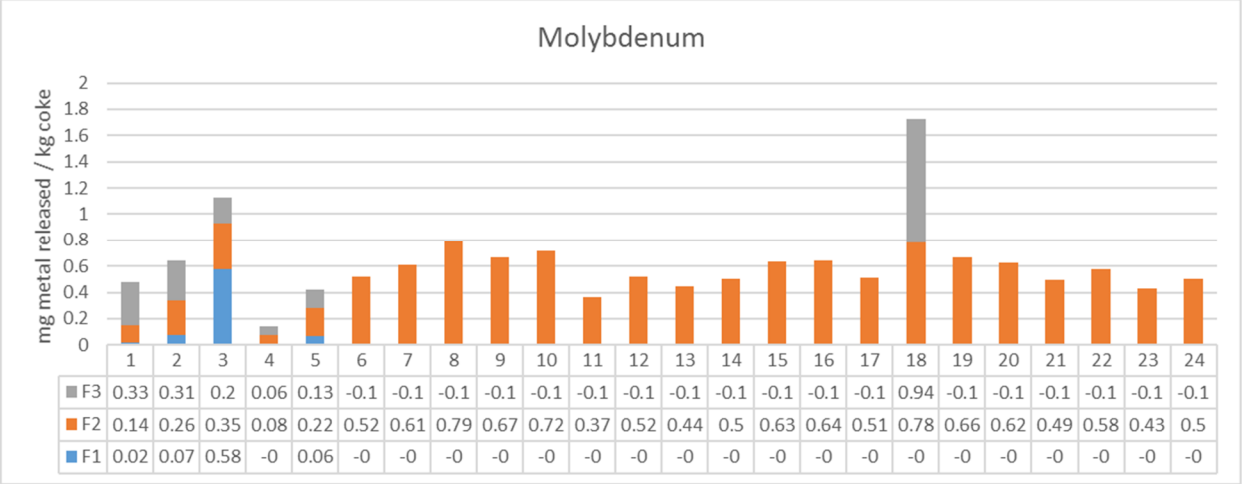

	1	2	3	4	5	6	7	8	9	10	11	12	13	14	15	16	17	18	19	20	21	22	23	24
F3	0.33	0.31	0.2	0.06	0.13	-0.1	-0.1	-0.1	-0.1	-0.1	-0.1	-0.1	-0.1	-0.1	-0.1	-0.1	-0.1	0.94	-0.1	-0.1	-0.1	-0.1	-0.1	-0.1
F2	0.14	0.26	0.35	0.08	0.22	0.52	0.61	0.79	0.67	0.72	0.37	0.52	0.44	0.5	0.63	0.64	0.51	0.78	0.66	0.62	0.49	0.58	0.43	0.5
F1	0.02	0.07	0.58	-0	0.06	-0	-0	-0	-0	-0	-0	-0	-0	-0	-0	-0	-0	-0	-0	-0	-0	-0	-0	-0

Figure J-1. Summary of leachability of V, Ni, Mn and Mo from coke by the 3 extractant solutions for the 24 samples analyzed.